Computational Study of Nonequilibrium Chemistry in High Temperature Flows

A DISSERTATION
SUBMITTED TO THE FACULTY OF THE GRADUATE SCHOOL
OF THE UNIVERSITY OF MINNESOTA
BY

Sriram Doraiswamy

IN PARTIAL FULFILLMENT OF THE REQUIREMENTS
FOR THE DEGREE OF
Doctor of Philosophy

November, 2010

Acknowledgements

Foremost, I would like to express my deep and sincere gratitude to my advisor Dr. Graham V. Candler for the continuous support of my Ph.D study and research, for his patience, motivation, enthusiasm, and immense knowledge. I would also like to thank Dr. J. Daniel Kelley for helping me understand the complex mechanisms behind various chemical processes. Without his contribution, this thesis would not have been possible.

For this dissertation, I would like to thank my reading committee members, Dr. Graham Candler, Dr. Mahesh Krishnan, Dr. Thomas Schwartzentruber and Dr. Sanford Lipsky for their time, interest and helpful comments.

During this work, I have collaborated with a lot of colleagues for whom I have great regard. The most notable of them for whom I would like to express my thanks are Dr. Joanna Austin and Dr. Manu Sharma of the University of Illinois at Urbana-Champaign, and Dr. Igor Adamovich and Dr. Munetake Nishihara of the Ohio State University. Their experiments were very helpful for this work.

The members of the Candler group have contributed greatly to my personal and professional time at the University of Minnesota. Thanks are due to Pramod Subbareddy, Ioannis Nompelis, Travis Drayna and Dave Peterson for getting me up to speed during the initial learning phase, and always being readily available to lend me their help. Other past and present members I had the pleasure of working with or alongside of are Vladimyr Gidzak, Michael Barnhardt, Ross Wagnlid, Matthew Bartkowicz, Eric Tylczak, Tian Wan, Ryuta Suzuki, Ryan Gosse, Heath Johnson, Chris Alba, Joel Gronwall, Loretta Trevino, Pietro Ferrero and the numerous summer interns.

My time at Minnesota was enjoyable in large part due to the many friends and groups I have become a part of. I would like to particularly thank Guruprasad Somasundaram and Rajapandiyan Asaithambi for all the fruitful discussions. My friends Shrinivas

Venkatraman, Mayur Suri, Vivek Venkatraman, Srikrishnan Srinivasan, Neelakantan Saikrishnan, Rajes Sau and Venkat Kalambur among many others have greatly enriched my stay at Minnesota. Thanks to Vladimyr and Bonnie Gidzak for the loads of fun time spent in their company.

Lastly, I would like to thank my family for all their love and encouragement. For my parents, Doraiswamy and Neela, who raised me with a love of science and supported me in all my pursuits. For my brother, Srikrishna who was always ready to help in whatever capacity. And most of all for my loving, encouraging, and patient wife Niranjana whose support during my entire Ph.D. is so appreciated. Thank you.

Dedication

To my parents,
Doraiswamy Natesan & Neela Doraiswamy

Abstract

Recent experimental measurements in the reflected shock tunnel CUBRC LENS-I facility raise questions about our ability to correctly model the recombination processes in high enthalpy flows. In the carbon dioxide flow, the computed shock standoff distance over the Mars Science Laboratory (MSL) shape was less than half of the experimental result. For the oxygen flows, both pressure and heat transfer data on the double cone geometry were not correctly predicted. The objective of this work is to investigate possible reasons for these discrepancies. This process involves systematically addressing different factors that could possibly explain the differences. These factors include vibrational modeling, role of electronic states and chemistry-vibrational coupling in high enthalpy flows.

A state-specific vibrational model for CO_2, CO, O_2 and O system is devised by taking into account the first few vibrational states of each species. All vibrational states with energies at or below 1 eV are included in the present work. Of the three modes of vibration in CO_2, the antisymmetric mode is considered separately from the symmetric stretching mode and the doubly degenerate bending modes. The symmetric and the bending modes are grouped together since the energy transfer rates between the two modes are very large due to Fermi resonance. The symmetric and bending modes are assumed to be in equilibrium with the translational and rotational modes. The kinetic rates for the vibrational-translation energy exchange reactions, and the intermolecular and intramolecular vibrational-vibrational energy exchange reactions are based on experimental data to the maximum extent possible. Extrapolation methods are employed when necessary. This vibrational model is then coupled with an axisymmetric computational fluid dynamics code to study the expansion of CO_2 in a nozzle.

The potential role of low lying electronic states is also investigated. Carbon dioxide has a single excited state just below the dissociation limit. CO and O recombine exclusively to this excited state and then relaxes to the ground electronic state. A simple model is proposed to represent the effect of this intermediate state in the recombination process. Preliminary results show that this excited electronic state is a potential reason for increased shock standoff distance observed in LENS facility.

The general role of chemistry-vibrational coupling in modeling recombination dominated flows is also investigated. A state-specific model is developed to analyze the complex chemistry-vibration coupling present in high enthalpy nozzle flows. A basic model is formulated assuming molecules are formed at a specific vibrational level and then allowed to relax through a series of vibration-vibration and vibration-translation processes. This is carried out assuming that the molecules behave as either harmonic or anharmonic oscillators. The results are compared with the standard vibration-chemistry model for high enthalpy nozzle flows. Next, a prior recombination model that accounts for the rotational-vibrational coupling is used to obtain prior recombination distribution. A distribution of recombining states is obtained as a function of the total energy available to the system. The results of this model are compared with recent experiments. Additionally, a reduced model is formulated using the concepts of the state-specific model. The results of this reduced model is compared with the state specific model.

Contents

List of Tables

List of Figures

Chapter 1

Introduction

1.1 Motivation, Background and Related Work

Over the last decade, there have been many puzzling reports associated with high enthalpy flows. Unlike moderate enthalpy flows (h_o<4 MJ/kg), at high enthalpies, computations were unable to reproduce the measurements made in LENS-I reflected shock tunnel.

The motivation to study CO_2 was initiated by the increased shock standoff distance observed in the high enthalpy LENS facility at CUBRC [1]. The shock standoff distance predicted by CFD was off by 200%. The LENS-I facility is a reflected shock tunnel, i.e. the shock reflects off the end wall reheating the gas providing very high temperature and pressure in the reservoir. For the same enthalpy, similar experiments were carried out in the LENS-X facility [2]. LENS - X is an expansion tunnel, and there is no stagnation of the gas at high temperature. The high enthalpy of the gas is obtained by virtue of high velocity. There is very good agreement between computation and experiment for this case. Figure 1.1 illustrates the comparison between CFD and the experiments in both LENS-I and LENS-X [1, 2].

Another set of high enthalpy experiments at similar conditions was carried out at the Hypervelocity Expansion Tube (HET) facility at University of Illinois at Urbana-Champaign. Comparison with simulations for spheres and MSL shapes were excellent. The results are shown in figures 1.2 and 1.3. The experimental results are taken from Sharma et. al. [3].

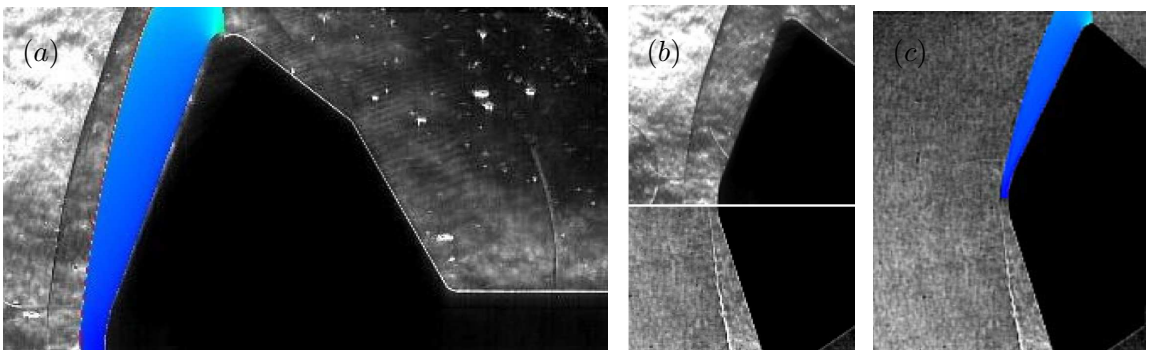

Figure 1.1: Comparison of shock shapes between (a) Standard Model and LENS-I, (b) LENS-I and LENS-X, (c) Standard Model and LENS-X

The agreement with both the expansion tunnels (HET and LENS-X) is very good. This shows that the differences observed in reflected shock tunnel for the same enthalpy is due to high temperature effects in the reservoir gas and subsequent expansion. To further investigate this problem of increased shock standoff distance in LENS-I, a series of numerical experiments was conducted by MacLean and Holden [1]. In their work, arbitrary quantities of chemical and vibrational energy were artificially frozen in the free-stream gas to study its effect on the shock standoff distance. It was found that although freezing both chemical and vibrational energy influenced the shock standoff distance, frozen vibrational energy had significantly larger impact than frozen chemical energy. It was found that if 42% of energy was frozen as vibrational energy then the correct shock standoff distance was predicted by CFD. Clearly, there is a need to model the vibrational relaxation of CO_2 in a better way.

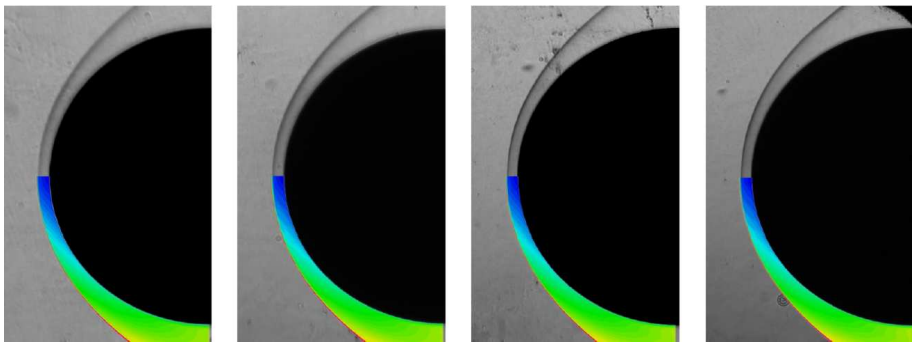

Figure 1.2: Comparison of shock shapes for spheres of different radii

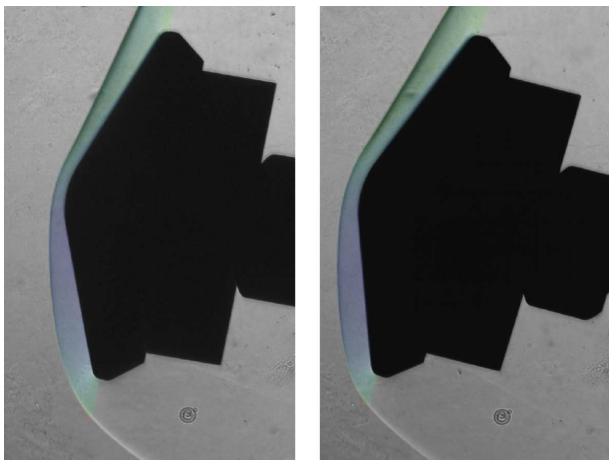

Figure 1.3: Comparison of shock shapes for the MSL shape at 11-deg and 16-deg angles of attack

Vibrational modeling may not be the sole reason for the discrepancy. There could be fundamental problems with modeling the recombination processes. For example, in high enthalpy air flows, Parker et al. [4, 5] measured the levels of nitric oxide in the exit plane of LENS-I, and found much lower levels than the computational results (factor of three). Nompelis et al. [6] investigated this problem and were unable to find a plausible explanation. Recently, Holden and co-workers at CUBRC ran a series of double cone shots in LENS-I with mixtures of oxygen and argon. An analysis of these results is presented by Nompelis et al. [7]. Part of the comparison is shown in figures 1.4 and 1.5. Note that at the lower enthalpy (Run 81), the comparison with experiments is very good. At higher enthalpy (Run 84), computational predictions of both pressure and heat flux measurements on the first cone is slightly higher than the experiments. Prior to these experiments, the mismatch in NO levels in high enthalpy air runs was attributed to the Zeldovich reactions involving nitric oxide. Now, the problem appears to be due to inadequate modeling of oxygen recombination. Since oxygen is an important species in the carbon dioxide system, better modeling of oxygen recombination might also explain a part of the puzzle associated with the increased shock standoff problem in LENS-I.

The potential role of higher electronic states in recombination should also be investigated to resolve the problem of increased shock standoff in CO_2. A recent quasi-classical trajectory calculation on the CO_2 system [8] shows that CO_2 is always formed in the

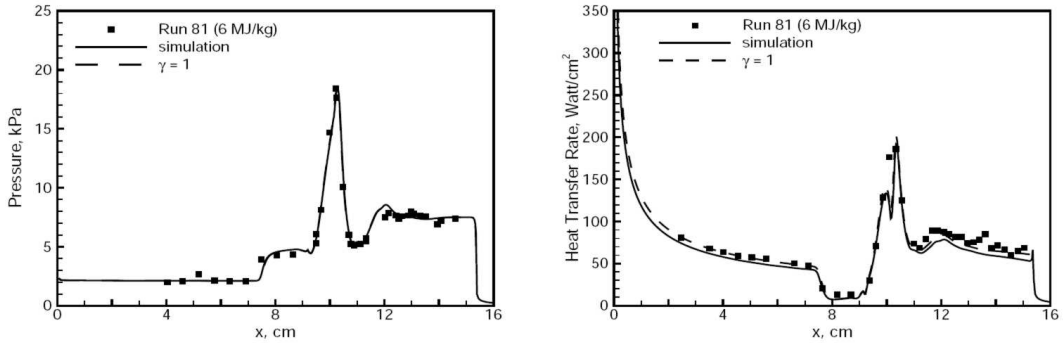

Figure 1.4: Surface pressure and heat transfer comparison with simulations; 50:50 oxygen-argon mixture at 6 MJ/kg, Run 81 conditions

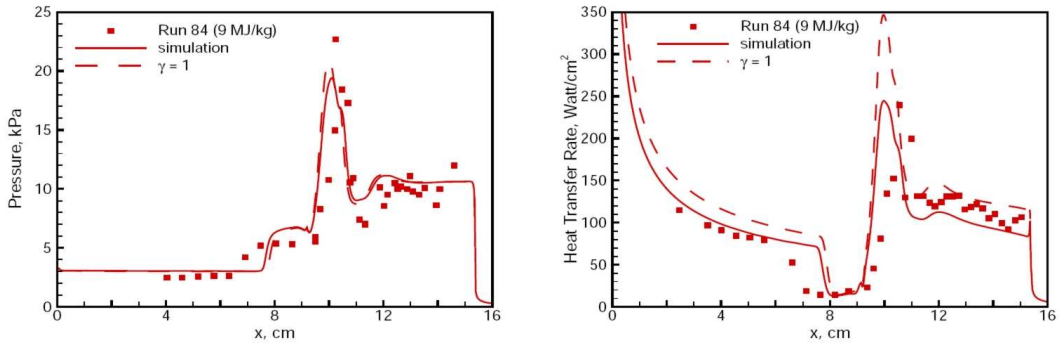

Figure 1.5: Surface pressure and heat transfer comparison with simulations; 50:50 oxygen-argon mixture at 9 MJ/kg, Run 84 conditions

excited state. This mechanism could also be a reason for the larger standoff distance.

1.2 Scope of the Current Study

In this work, we investigate each of the reasons separately to gain a better understanding of the various complex processes. We adopt a state-specific approach to analyze the vibrational relaxation processes. In this approach, we consider each vibrational state of the molecule to be a different species. By following such a method, we do not make any assumptions about the distribution of the internal vibrational states. This also provides deeper insight into the various vibrational relaxation processes present in a reacting system.

Chapter 2 presents the governing equations for a chemically reacting and vibrationally relaxing gas. The Navier-Stokes equations are presented along with the numerical methods used to solve such a system. We use standard numerical techniques that are popular and useful for practical applications. The standard models for vibrational relaxation and chemical reactions are presented along with transport coefficients.

Chapter 3 investigates the role of vibrational modeling in the CO_2 system. We use the state specific approach to study this problem. The rate constants for various reactions/transitions are obtained from experimental data wherever possible. Extrapolation methods are employed when necessary. We validate this vibrational model against experimental data. The state specific model developed in this chapter forms the basis for further analysis of recombination process.

Chapter 4 deals with the potential role of higher electronic states in the CO_2 system. We use a simple model with appropriate justifications to reproduce the recombination mechanism from a quasi-classical trajectory calculation.

Chapter 5 deals with analysis of chemistry-vibrational coupling in high enthalpy flows. O_2 is chosen as the candidate species to study the recombination in the nozzle. We consider both harmonic and anharmonic oscillators in the state specific approach to study the recombination. The first part of this chapter is purely a numerical experiment. After the initial analysis, we use the information theory approach to study the recombination by accounting for rotational-vibrational coupling in diatomics. The results for this model are compared against standard model results. In the last part of this chapter, a reduced model that can be used for flows of practical interest is developed.

Chapter 2

Mathematical Formulation and Numerical Method

2.1 Introduction

In this chapter, the set of coupled partial differential equations that describe the dynamics of a high-temperature flowfield are derived. The equation set is expanded so that it is applicable to a gas that is vibrationally excited and chemically reacting. The chemical kinetics model that describes the reacting flowfield and the assumptions underlying the current description are presented. The limitations of the standard models utilized to study chemically reacting and vibrationally excited flows are discussed.

2.2 Basic Assumptions

The continuum assumption is utilized to derive the basic equations of interest. This assumption is valid when the mean free path is much lesser than the characteristic length scale of the body or the flow. The ratio of the mean free path to the characteristic length scale is defined by the Knudsen number, Kn. The continuum formulation requires the Knudsen number to be much less than one so that there are a large number of molecules within a computational volume. For the flows of interest in this present work, (i.e.) the nozzle flows and blunt body simulations, this Knudsen number is in the range of 0.1 – 0.0001, thereby justifying the assumption of continuum. The small Knudsen number

also justifies the use of no-slip condition at the wall for both velocity and temperature, since there are a large number of collisions of the gas molecules with the wall. It is also implicit in the continuum formulation that there is very little statistical variation within the flowfield, therefore continuum description of the viscous fluxes is also consistent.

The thermal state of the gas is assumed to be described by separate temperatures. A single temperature description of flowfield does not adequately reflect the complex physics behind the various processes. Each energy mode (i.e. translational, rotational or vibrational) relaxes with its characteristic time scale, and takes finite time to approach equilibrium. But the number of collisions needed to equilibrate translational and rotational modes of a gas species is very small. This justifies the use of a single temperature (T) to describe translational and rotational modes. This assumption is reasonable in the continuum regime, where for a typical species, the number of collisions needed to equilibrate is about five [9].

In the standard formulation described in this chapter, the energy contained in the vibrational mode of a species is described by the vibrational temperature, T_v. The internal vibrational distribution of states is assumed to conform to the harmonic oscillator description (Boltzmann distribution) at all vibrational temperatures. Harmonic oscillator description assumes equally spaced vibrational energy levels. Additionally, this description of temperature assumes the intramolecular and intermolecular vibrational relaxation to be very fast, and this justifies the use of a single vibrational temperature to describe the vibrational state of the gas mixture. This type of description is valid at low vibrational temperatures where only the first few low lying vibrational states are populated. When higher vibrational states are populated, the behavior of the molecule deviates from the harmonic oscillator description. This is because the energy levels of higher vibrational states are closer to each other, and a proper description of such a system would warrant a detailed model that incorporates the rate of relaxation between each vibrational state. Also, at extreme conditions, there is an inherent coupling between the rotational and the vibrational states. In this chapter we focus on the derivation of the standard model of vibrational energy transfers. We will relax some of the assumptions in future chapters.

We will restrict the formulation to non-ionized, chemically reacting flows. Further, specific assumptions will be discussed in conjunction with the derivation of the governing

equations.

2.3 The Conservation Equations

For a chemically reacting flow of ns species of which nd are diatomic molecules, there will be ns mass conservation equations.

$$\frac{\partial \rho_s}{\partial t} + \nabla.(\rho_s \mathbf{u}) = -\nabla.(\rho_s \mathbf{v_s}) + w_s \tag{2.1}$$

where ρ_s is the density of the species s, $\mathbf{u}$ is the mean velocity of the flow, $\mathbf{v_s}$ is the diffusion velocity of the species s, and w_s is the rate of formation of species s due to chemical reaction. The total density ρ is obtained by summing up individual species densities. The expressions for the chemical source terms and the diffusion velocities are discussed in later sections of this chapter.

The conservation of momentum equation is given as

$$\frac{\partial (\rho \mathbf{u})}{\partial t} + \nabla.(\rho \mathbf{u} \otimes \mathbf{u} + pI) = \nabla.\tau \tag{2.2}$$

where p is the thermodynamic pressure, τ is the viscous stress tensor. The above equation assumes that there are no external forces acting on the flow. Note that the diffusion velocities do not appear in the equation as their contribution sum identically to zero [10].

The conservation of the total energy of the mixture of gases is expressed as,

$$\frac{\partial E}{\partial t} + \nabla.((E+p)\mathbf{u}) = \nabla.(\tau \mathbf{u}) - \nabla.(\mathbf{q_t} + \mathbf{q_r} + \mathbf{q_v}) - \nabla.\sum_{s=1}^{ns} \rho_s h_s \mathbf{v_s} \tag{2.3}$$

where $\mathbf{q_t}$, $\mathbf{q_r}$ and $\mathbf{q_v}$ are the translation, rotational and vibrational heat flux vectors, and h_s is the total enthalpy per unit mass of species s. The method of evaluation of the heat flux vectors will be discussed in the subsequent sections.

Since we describe the vibrational energy of the flowfield separately, we need to construct the conservation equation for vibrational energy as well. As stated earlier because we assume that the vibration-vibration coupling is very strong, we can describe the vibrational energy by a single vibrational temperature. This also implies that we do not have to solve for the vibrational energy for each species. The conservation equation

for the vibrational energy per unit volume is given by [10],

$$\frac{\partial E_v}{\partial t} + \nabla.(E_v \mathbf{u}) = -\nabla.\mathbf{q_v} - \nabla.\sum_{s=1}^{ns} \rho_s e_{vs} \mathbf{v_s} + w_v \tag{2.4}$$

where e_{vs} is the species vibrational energy per unit mass and w_v is the vibrational energy source term. The vibrational energy source term will be discussed in future sections.

2.4 Equation of State

The relation between the conserved quantities and the primitive variables such as pressure or temperature is derived in this section. The total energy is composed of separate components of energy that may be written as,

$$E = \sum_{s=1}^{ns} \rho_s c_{vs} T + \frac{1}{2}\rho \mathbf{u}.\mathbf{u} + E_v + \sum_{s=1}^{ns} \rho_s h_s^\circ \tag{2.5}$$

where c_{vs} is the translation-rotational specific heat given by

$$c_{vs} = c_{vs}^{tr} + c_{vs}^{rot} \tag{2.6}$$

The translational and rotational specific heats are given by

$$c_{vs}^{tr} = \frac{3}{2}\frac{R_u}{M_s} \tag{2.7}$$

$$c_{vs}^{rot} = \frac{R_u}{M_s}, s < nd \tag{2.8}$$

where R_u is the universal gas constant. The vibrational temperature for the mixture is given by inverting the expression for the vibrational energy contained in a harmonic oscillator at the vibrational temperature T_v. This assumes Boltzmann distribution of population over the vibrational states. The expression for the vibrational energy is given as,

$$E_v = \sum_{s=1}^{nd} \rho_s \frac{R_u}{M_s} \frac{\theta_{vs}}{\exp(\theta_{vs}/T_v) - 1} \tag{2.9}$$

where θ_{vs} is the characteristic vibrational temperature of species s. The pressure is given by perfect gas equation of state.

$$p = \sum_{s=1}^{ns} \rho_s \frac{R_u}{M_s} T = \rho R T \qquad R = \sum_{s=1}^{ns} \frac{\rho_s}{\rho} \frac{R_u}{M_s} \tag{2.10}$$

The enthalpy per unit mass is defined by

$$h_s = c_{vs} T + \frac{p_s}{\rho_s} + e_{vs} + h_s^\circ \tag{2.11}$$

2.5 Shear Stresses, Heat Fluxes and Diffusion Velocities

The viscous stress tensor for a Newtonian fluid is given by,

$$\tau = \mu(\nabla \mathbf{u} + \nabla \mathbf{u}^T) + \lambda \nabla . \mathbf{u} \tag{2.12}$$

Using the Stokes hypothesis for bulk viscosity we get,

$$2\mu + 3\lambda = 0 \Rightarrow \lambda = -\frac{2}{3}\mu \tag{2.13}$$

where μ is the kinematic viscosity of the mixture. This kinematic viscosity depends on the state of the fluid and the composition.

The heat fluxes are assumed to obey the Fourier's law,

$$\mathbf{q_i} = -\kappa_i \nabla T_i \tag{2.14}$$

where i refers to any internal energy mode. The thermal conductivities for different internal energy modes are related to molecular viscosity by the Eucken relation [11]. In this formulation, it is assumed that the transport of translational energy involves correlation with velocity, but transport of other internal energy modes such as the rotational and vibrational modes involves no correlation.

$$\kappa_{ts} = \frac{5}{2} c_{vs}^{tr} \mu_s \qquad \kappa_{rs} = c_{vs}^{rot} \mu_s \qquad \kappa_{vs} = c_{vs}^{vib} \mu_s \tag{2.15}$$

where μ_s and κ_s are species viscosity and thermal conductivity. The vibrational specific heat capacity c_{vs}^{vib} is computed directly by

$$c_{vs}^{vib} = \frac{\partial e_{vs}}{\partial T_v} \tag{2.16}$$

The diffusion of mass is due to changes in mass fractions, temperature or pressure. For the flowfields of interest, changes in mass fractions alone contribute to the mass diffusion. Steep gradients in temperature are typically accompanied with breakdown of Navier-Stokes equations [12]. Also the baro-diffusion terms are negligible. Under the above assumptions, the Fick's Law can be used,

$$-\rho_s \mathbf{v_s} = \rho D_s \nabla \frac{\rho_s}{\rho} \tag{2.17}$$

The multi-component diffusion coefficient D_s is replaced with a single diffusion coefficient which is derived assuming a constant Lewis number, Le.

$$Le = \frac{\rho D c_p}{\kappa} \tag{2.18}$$

where c_p is the translational-rotational specific heat capacity at constant pressure and κ is the thermal conductivity of the mixture. The assumption of constant Lewis number is valid for gas mixtures that do not have any light particles such hydrogen or electrons.

To compute the thermal conductivity (κ) and viscosity (μ) of the mixture we use Wilke's mixing rule [13].

$$\mu = \sum_s \frac{X_s \mu_s}{\phi_s} \qquad \kappa = \sum_s \frac{X_s \kappa_s}{\phi_s} \tag{2.19}$$

where,

$$X_s = \frac{c_s M}{M_s}, M = \sum_s \frac{c_s}{M_s} \tag{2.20}$$

$$\phi_s = \sum_r X_r \left[1 + \sqrt{\frac{\mu_s}{\mu_r}} \left(\frac{M_r}{M_s}\right)^{\frac{1}{4}}\right]^2 \left[\sqrt{\left(8(1 + \frac{M_s}{M_r})\right)}\right]^{-1} \tag{2.21}$$

where c_s is the mass fraction of the species s. The model of Blottner [14] is used for viscosity of species, these are calculated using curve fits of the form,

$$\mu_s = 0.1 \exp[(A_s \ln T + B_s) \ln T + C_s] \tag{2.22}$$

The values of A_s, B_s and C_s are given in the appendix A.

2.6 Chemical Source Terms

In this section we evaluate the source terms w_s. These represent the rate of production/destruction of species s. For the systems considered in the present work, two types of reactions can occur. The first one is the dissociation/recombination reactions for any diatomic species $\mathcal{X}_2$,

$$\mathcal{X}_2 + M \rightleftharpoons \mathcal{X} + \mathcal{X} + M \tag{2.23}$$

where M is any third body/collision partner that provides the energy for the dissociation. For the reverse reaction, the excess energy released during the recombination is shared between the third body M as kinetic energy and the vibrational energy in the newly formed molecule.

The second type of reaction is the exchange reaction. It has the general form,

$$\mathcal{A} + \mathcal{BC} \rightleftharpoons \mathcal{AC} + \mathcal{B} \tag{2.24}$$

The rate constants of the forward and the backward reactions take the Arrhenius form. By summing the rates of the formation of species due to each reaction, we will be able to evaluate the chemical source term w_s.

The forward and the backward reaction rates are affected by the level of thermal nonequilibrium in the flow. We use the standard two temperature Park's vibration-dissociation model [15] to calculate the rates. Park's model has been widely in use primarily due to its ease of implementation. Even though Park's model does not satisfy the principle of detailed balance, it has been shown to provide satisfactory results for a wide variety of flow conditions [10]. The Park model assumes that the reaction rates are functions of an effective temperature given by,

$$T_{eff} = \sqrt{T T_v} \tag{2.25}$$

The reaction rates are estimated at this effective temperature.

$$k_{f_m} = C_{f_m} T_{eff}^{\eta_m} \exp(-\theta_m / T_{eff}) \tag{2.26}$$

where m denotes the reaction. The values of C_{f_m}, θ_m and η_m are obtained from experimental curve fits and are tabulated in the Appendix A. The backward reaction rate

coefficients are obtained by the principle of detailed balance.

$$k_{b_m} = \frac{k_{f_m}}{K_{eq_m}} \tag{2.27}$$

The equilibrium constant K_{eq_m} is evaluated using the Van't Hoff equation,

$$\ln K_{eq_m} = \frac{-\Delta H_m}{RT} + \frac{\Delta S_m}{R} \tag{2.28}$$

where ΔH_m and ΔS_m are the changes in entropy and enthalpy for the reaction m. The entropy and enthalpy values are obtained using the Gordon McBride fits [16].

2.7 Vibrational Energy Source Term

In this section we discuss the vibrational energy source term w_v. Vibrational energy exchange takes place through molecular collisions. These collisions can be of two types, non-reactive collisions and reactive collisions.

In a realistic mixture of gas, there are many types of vibrational energy exchanges for non-reactive collisions. There can be energy exchanges between vibrational and translational modes, energy exchanges between vibrational modes of different molecules and vibrational energy exchanges within the same molecule. As the molecules are assumed to behave as harmonic oscillators, the vibrational energy exchange within the molecule is ignored. Also, we assume that the vibrational energy exchange between different molecules is extremely fast. The translational and rotational modes are assumed to be in equilibrium characterized by a single temperature. The coupling between the rotational and the vibrational modes is not considered. At high internal energies, we can not assume that vibrational and rotational modes to be separable. The rotational energy of the molecule determines the allowable vibrational states.

In this chapter, we only consider the vibrational-translational mode energy exchange. The source term due to the vibrational-translational energy exchange is given by the Landau-Teller model [11] as,

$$Q^{LT}_{t-v_s} = \rho_s \frac{e^{\star}_{v_s} - e_{v_s}}{< \tau_s >} \tag{2.29}$$

where $e^{\star}_{v_s}$ is the vibrational energy per unit mass of species s evaluated at the local translational temperature, and $<\tau_s>$ is the molar averaged Landau-Teller relaxation

time given by [17],

$$< \tau_s >= \frac{\sum_r X_r}{\sum_r X_r/\tau_{sr}} \tag{2.30}$$

where X_r is the mole fraction of species r and τ_{sr} is the relaxation time of the species pair s and r. The standard form of expression used to evaluate this relaxation time is by using the Millikan and White fits [18],

$$\tau_{sr} = \frac{1}{p} \exp[A_{sr}(T^{-1/3} - 0.015\mu_{sr}^{1/4}) - 18.42] \tag{2.31}$$

$$A_{sr} = 1.16 \times 10^{-3} \mu_{sr}^{1/2} \theta_{v_s}^{4/3} \tag{2.32}$$

$$\mu_{sr} = \frac{M_s M_r}{M_s + M_r} \tag{2.33}$$

For the vibrational source term due to reactive collisions (chemical reactions), we assume that the newly formed (destroyed) molecule gain (lose) vibrational energy given by the local vibrational temperature. This assumption is consistent with assuming that the vibrational modes of different molecules equilibrate extremely fast to the local vibrational temperature. Under these assumptions, the vibrational source term due to chemical reactions is given by,

$$Q_{v_s} = w_s e_{v_s} \tag{2.34}$$

The total vibrational energy source term is the sum of the vibrational-translational energy exchange and vibrational energy due to chemical reactions,

$$w_v = \sum_{s=1}^{nd} Q_{v-t_s}^{LT} + \sum_{s=1}^{nd} w_s e_{v_s} \tag{2.35}$$

2.8 Boundary Conditions

In the current study, we use no-slip velocity boundary condition at solid surfaces. At the wall, we assume isothermal non-catalytic wall for all the cases unless stated otherwise. Non-catalytic wall implies that there is zero-gradient in species in the wall normal direction. Fully catalytic wall implies that all atomic species fully recombine at the wall. For the supersonic nozzle simulations, we use a subsonic boundary condition at the reservoir such that the Mach number at the throat is unity [19].

2.9 Numerical Method

In the present work, we use the high fidelity codes developed by Candler [19] for computing nozzle flows, and the unstructured three dimensional solver (US3D) developed by Nompelis et al. [20]. The nozzle code uses an excluded volume equation of state to account for high pressure effects encountered in the reservoir. This code is an axisymmetric CFD solver that solves the compressible Navier-Stokes equations. This code is used to solve for all cases of nozzle flows. For the flows over blunt bodies, the unstructured hybrid implicit unstructured finite volume solver is used. In these codes, the inviscid fluxes are calculated using a low dissipation version of the Steger-Warming flux vector splitting. Second order accuracy in space is achieved using an upwind biased MUSCL approach [21]. Time integration is performed implicitly using a parallel line relaxation procedure [22].

Chapter 3

Vibrational Modeling for the CO_2 System

3.1 Introduction

In this chapter, we will derive the vibrational model used to study the CO_2 system. We will also formulate a basic chemistry-vibrational coupling model to study the high enthalpy nozzle flow. The motivation to focus on vibrational modeling of CO_2 is due to the systematic study by MacLean and Holden [1]. This numerical experiment was carried out to estimate the effect of the internal energy on shock standoff distance, and is not based on physics. It was found that the frozen vibrational energy had a much larger impact on the shock standoff distance than the frozen chemical energy. In this previous study [1], a frozen vibrational content of 42% of the total enthalpy was found to predict the shock shape correctly and also improve the quality of agreement of surface pressure measurements and heat transfer rates. Though the vibrational content of 42% is aphysical, it does show that there is a need to better model the vibrational processes such as intermolecular V-V exchange, intramolecular V-V exchange and V-T exchange reactions. There is a large body of literature regarding the vibrational energy transfer in CO_2, both intramolecular transfer among the internal state manifolds and intermolecular transfer processes to other molecules, including CO and O_2. Representative collections of such data are found in the surveys by Taylor and Bitterman [23], Lewis and Trainor [24], and Weitz and Flynn [25]. Much of the interest in CO_2 stems

Table 3.1: Reservoir conditions for the CUBRC run (Run 8) with an effective enthalpy of 5.63 MJ/kg and a pressure of 29.5 MPa.

Temperature	3500 K
ρ	39.9 kg/m^3
cCO_2	0.7737
cCO	0.1440
cO_2	0.0786
cO	0.0036

from its value as a laser medium. Efforts to model such lasers, which typically use CO_2, N_2, O_2 and He, have employed reduced reaction sets with success [26]. Given the similarity of the high-enthalpy CO_2 (CO_2, CO, O_2) to the laser system, one can be optimistic that the rate equation calculation will point to a simplified approach. In order to understand the mechanism of vibrational energy transfers, as a first step each vibrational state must be considered as a separate chemical species, and rates for their formation and loss need to be estimated. In this work, all vibrational states with energy less than 1 eV are included. The goal is to develop a simplified model with a few characteristic temperatures that will greatly condense the rate data. This cannot be done without explicit calculations that justify such simplification.

3.2 Vibrational Modeling of CO_2

3.2.1 Thermodynamic Calculations

The STANJAN thermodynamic package was used to calculate the reservoir gas properties for 'run 8' as described by MacLean and Holden [1]. Run 8 was one of several tests run at the CUBRC for high-enthalpy high density CO_2 gas. Similar calculation with a different thermodynamics package has been reported by MacLean and Holden, and the results of the two codes were in good agreement. Table 3.1 shows the computed reservoir conditions for 'run 8' such as temperature, density, and mass fractions for different species. The excited electronic O_2 states are not included.

CO_2 has three modes of vibration: symmetric stretching mode, doubly degenerate

bending mode and the antisymmetric stretching mode. The first simplification is to group the symmetric stretch (ν_1) and bending modes (ν_2) of CO_2, since they form a set of levels that are strongly coupled by collisions with other molecules [27], and by Fermi resonance among themselves. The stretch-bend manifold of CO_2 states receives special treatment in obtaining the state specific population of the antisymmetric states. Given the efficient intergroup coupling, it is reasonable to label the symmetric stretch-bend levels with a single quantum number (ν_{SB}), and consider them separately from the antisymmetric stretch mode (ν_3). An additional simplification is realized using the fact that the collisional deactivation of the stretch-bend states is fast, and faster than the rate of energy transfer into them [28]. It is shown that collisional deactivation of the stretch-bend states has a rate constant k $\geq$ 2-3$\times$ 10^{-12} cc/s at 2000 K and the rate increases for upper stretch-bend states [29, 30]. The rate of transfer from the antisymmetric state into the stretch-bend manifold (from $\nu_3 = 1$ to $\nu_2 = 3$), although fairly fast [30], is 5 times slower than the stretch-bend mode V-T,R quenching rate, and at least 15 times slower than transfer out of the $\nu_2 = 3$ state. As the CO_2 system relaxes during the expansion, energy transfer from the antisymmetric state collisionally populates the stretch-bend manifold. Because this intramolecular transfer is slower than the stretch-bend manifold relaxation rate via V-T,R transfer, the intramolecular process effectively deactivates the antisymmetric state to the heat bath. Further justification for this assumption is given by the study by MacLean and Holden [1], this numerical kinetic study of the CUBRC expansion nozzle (run 8) showed that the stretch-bend vibrational temperature was only a few degrees higher than the gas kinetic temperature. The result of all this is that the stretch-bend manifold is not explicitly treated in this work. The antisymmetric populations (ν_3) are implicitly summed over the stretch-bend states. This is analogous to the summation over rotational states for the diatomics. Just as for rotation, the stretch-bend manifold is assumed to be at the gas kinetic temperature throughout the expansion. A similar state-specific approach for CO_2 was carried out by Limbaugh and Drakes [31] to analyze radiatively heated wind tunnels.

The results in Table 3.1 are used to compute the number densities in each vibrational state for CO_2, CO and O_2. In general, for a given species, the population N_i in the

level i relative to that in the ground state N_0 is given by

$$\frac{N_i}{N_0} = \left(\frac{g_i}{g_0}\right) \exp(-\Delta E_i/kT) \tag{3.1}$$

where g_i is the statistical weight of level i, ΔE_i is the energy of level i above the ground state, k is the Boltzmann constant and T is the temperature. The total population in all the states is

$$N_{total} = N_0 + N_1 + N_2 + ... = N_0(1 + \Sigma[\frac{g_i}{g_0} \exp(-\Delta E_i/kT)]) \tag{3.2}$$

where the sum is over all levels from $i = 1$ to a level high enough that succeeding terms are effectively zero. For a temperature of 3500 K and energy of 8000 cm^{-1}, the exponential term in Eq. (3.2) has a value of 0.037. The statistical weights g_i are unity for CO and O_2 vibrational levels, and for the CO_2 antisymmetric stretch levels considered here. This fact coupled with the small value of the exponential term at 8000 cm^{-1} indicates that neglect of higher energy levels in these manifolds would have little effect on the computed populations (less than 1%). By construction, the number densities calculated via Eqs. (3.1) and (3.2) necessarily sum to the thermodynamically calculated total values obtained from Table 3.1. Also, correct ratios among the number densities appropriate to the thermal equilibrium are obtained. This means that the value in each retained level is a bit higher than the value that would result if more levels were included. For CO and O_2, these population differences are less than 1%. For $CO_2(\nu_3)$, the difference is about 2%. With the 8000 cm^{-1} limit given above, there will be 4 $CO_2(\nu_3)$ levels, 5 CO levels and 6 O_2 levels including the ground states. Along with the O atoms, there are a total of 16 separate species. The resulting populations are shown in Table 3.2.

3.2.2 Vibrational Energy Transfer Processes

Although energy transfer data are available for the species of interest, much of it involves low-lying states, mostly $v = 1 \rightarrow 0$, and limited temperature ranges. We will be required to scale the data to upper states by applying factors derived from transition matrix elements, and by adjusting the rate constant to account for the varying energy defects between initial and final vibrational states. First we discuss the transition matrix

Table 3.2: Number densities for individual species in the reservoir.

Species	Number densities (cm^{-3})
Total $CO_2(\nu_3)$	4.220^{20}
$\nu_3 = 0$	2.660^{20}
$\nu_3 = 1$	1.020^{20}
$\nu_3 = 2$	0.391^{20}
$\nu_3 = 3$	0.152^{20}
Total CO_2	1.240^{20}
$v = 0$	0.730^{20}
$v = 1$	0.302^{20}
$v = 2$	0.127^{20}
$v = 3$	0.054^{20}
$v = 4$	0.023^{20}
Total O_2	5.900^{19}
$v = 0$	2.830^{19}
$v = 1$	1.490^{19}
$v = 2$	0.794^{19}
$v = 3$	0.429^{19}
$v = 4$	0.234^{19}
$v = 5$	0.129^{19}
Total O	5.400^{18}

elements. The collisional interactional potential can be formally written as

$$V_I(R, r_1, r_2) = (1 + a\delta r_2 + b\delta r_2 + c\delta r_1\delta r_2 + d\delta r_1^2 + e\delta r_2^2 + ...)V_I(R, r_1^0, r_2^0) \qquad (3.3)$$

The R - coordinate describes relative motion between two colliding molecules and contains the angular information as well. The δr's are the small displacements of the molecular internal separation from the equilibrium values r^0. The expansion of the right hand side of Eq. (3.3) can be terminated at second-order with little loss in accuracy. The two linear δr terms in the interaction potential are responsible for excitation/de-excitation of vibration in molecules 1 and 2 respectively, i.e. single molecule V-T,R processes. The bilinear term is responsible for the V-V transfer, and the quadratic terms produce two quantum processes in molecule 1 or 2. The bilinear term can also produce simultaneous excitation in molecules 1 and 2. The two quantum process can be ignored in our

system, because the one quantum energies are high $\sim$ 2000 cm^{-1}, and the two quantum processes at $\sim$ 4000 cm^{-1} are much less probable, even at the temperatures in the present study. If the molecules are harmonic oscillators, the single-quantum transition probabilities for a given molecule scale with the upper state quantum number; a 2$\rightarrow$1 process has twice the probability of a 1$\rightarrow$0 process. This scaling rule remains a good approximation for the real, anharmonic molecules in the CO_2-CO-O2 system because the anharmonic effects are small for the relevant low lying states. Thus we will use this scaling to extrapolate rate constants from lower to upper states.

A more complicated scaling involves accounting for the varying state energy separations resulting from anharmonicity. A complete treatment of the energy-averaged set of molecular collisions interacting through V_I in Eq. (3.3) leads to a rate constant for a given process. To do this exactly, one must have complete knowledge of V_I and then execute a quantum-mechanical treatment of the dynamics. This has been done only for a few systems, and the results are numerical and not analytical. However, various approximate approaches have been developed that give useful results, although arbitrary adjustments and constants are employed to get agreement with experiment. The best known of these analytical treatment is the method of Schwartz, Slawsky and Herzfeld - SSH theory by Rapp and Kassal [32]. The key aspect of this theory that we use here is the prediction, in its simplest form, of a rate constant expression,

$$k_f = C \exp(B/T^{1/3}) \tag{3.4}$$

where B is a function of the transition frequency ν raised to the 2/3 power. In fact for most of the processes of interest here, the functional form in Eq. (3.4) provides a good fit to the experimental data, particularly for the temperatures above 500 K. This form has been used for all the V-T,R processes and non-resonant V-V processes, and the $\nu^{2/3}$ scaling has been used for these V-V processes. This $\nu^{2/3}$ scaling has been ignored for the V-T,R processes because the transition frequency variation - a few 10's of wavenumbers - is not important when applied to the large V-T,R frequencies. It does have an effect on the much smaller V-V transition frequencies. To summarize, the harmonic oscillator scaling rule is consistently applied to obtain rate constants for upper states from the lower state experimental values. The SSH frequency scaling is applied only to non-resonant V-V processes.

Near resonant same species rate constants are treated differently using an approach developed for the CO-CO V-V transfer by Jeffers & Kelley [33]. There are no data for such fast processes at high temperature, so extrapolation is required. These processes are all fast, and do not add or take away much energy from the system. The extrapolated rate constants may not be accurate even within a factor of two or three but this will have little effect on the flow dynamics.

The rate constants used in the present work are tabulated in the Appendix B (B.1, B.2 and B.3). All the reactions are in the exothermic direction. For the V-T,R processes and intermolecular V-V processes, the forward rate constants are of the form described in Eq. (3.4), and for the intramolecular processes, the rate constant is of the form,

$$k_f = C(T/1000) \tag{3.5}$$

The reverse rates are obtained by detailed balance, i.e. multiplying the listed rate constants by $\exp(-\Delta E/kT)$,

$$k_b = k_f \exp(-\Delta E/kT) \tag{3.6}$$

The ΔE values are obtained from spectroscopic data for the molecules involved [34, 35] and include anharmonicity corrections. The value of the Boltzmann constant k when ΔE is expressed in cm^{-1} is 0.695.

Intramolecular V-V processes are listed in Table B.1. As stated earlier, these near-resonant V-V processes will be fast at the temperatures considered in this study. Unfortunately, none have been measured at high temperature. The rate constants for this set of reactions are based on the experimental results for CO-CO at room temperature. These have an unusual defect dependence that was successfully reproduced by a theoretical model by Jeffers and Kelley [33] incorporating both long and short range interactions. This model can be extended to high temperatures, where the short range interaction is dominant. The CO-CO rates in Table B.1 are based on this calculation. There are room temperature rate constants for O_2-O_2 [36], and the rate constants for high temperatures are scaled based on the short range model of CO. Similar procedure was adopted for $CO_2(\nu_3)$ to obtain rates at high temperatures. The accuracy of these rate constants can be off by as much as a factor of two, but because these processes are all faster than the VT processes, it does not really matter, and these processes do not take or release much energy into the translational or rotational degrees of freedom.

In Table B.2, for the reaction

$$CO_2(\nu_3) + M \rightleftharpoons CO_2(\nu_3 - 1) + M \tag{3.7}$$

direct one quantum V-T transfer is very slow because of the large energy gap between the quantum states, and has never been measured. The major ν_3 loss process is intramolecular V-V transfer to the stretch-bend manifold. Deactivation of the stretch-bend manifold is fast at temperatures and densities appropriate for this study, and it can be safely be treated as part of the heat bath with the rotational modes. Therefore, the intramolecular V-V process is equivalent to a V-T,R process and is treated that way in the rate package.

V-V energy transfer rates for CO_2-O_2 have not been included in the list of reactions in Table B.3 because these rates have not been measured at high temperatures. The large energy defect ($\sim$ 800 cm^{-1}) is within a few wavenumbers of that for N_2-O_2, and that process is known to be very slow. This rate cannot compete with V-V transfer to CO, or with the intramolecular ν_3 loss process.

3.2.3 Numerical Results

Numerical experiments were carried out to observe the variation of relaxation times with temperature. The relaxation time is defined as follows,

$$\frac{E_v - E_v^\star}{E_{v0} - E_v^\star} = e^{-t/\tau} \tag{3.8}$$

If E_v is the vibrational energy at any time 't', $E_v^\star$ is the equilibrium vibration energy at that particular temperature and E_{v0} is the initial vibrational energy, then the relaxation time can be defined as the time taken for the difference E_v-$E_v^\star$ to fall to $\frac{1}{e}(E_{v0}$-$E_v^\star)$ [11].

Figure 3.1 shows the comparison of the relaxation times with experiments. The solid lines represent the best fit curve for the relaxation times obtained in the present work. The experimental data were obtained from Park [37]. The relaxation times of pairs of species such as CO-CO, CO-O, O_2-O_2 and O_2-O are in very good agreement with the experimental data. We see that separating the antisymmetric stretch levels from the symmetric stretch-bend levels leads to an increase in the relaxation time. The relaxation time can be related to the temperature for most pairs by the following equation,

$$p\tau = \exp(aT^{-\frac{1}{3}} + b) \qquad [atm.s] \tag{3.9}$$

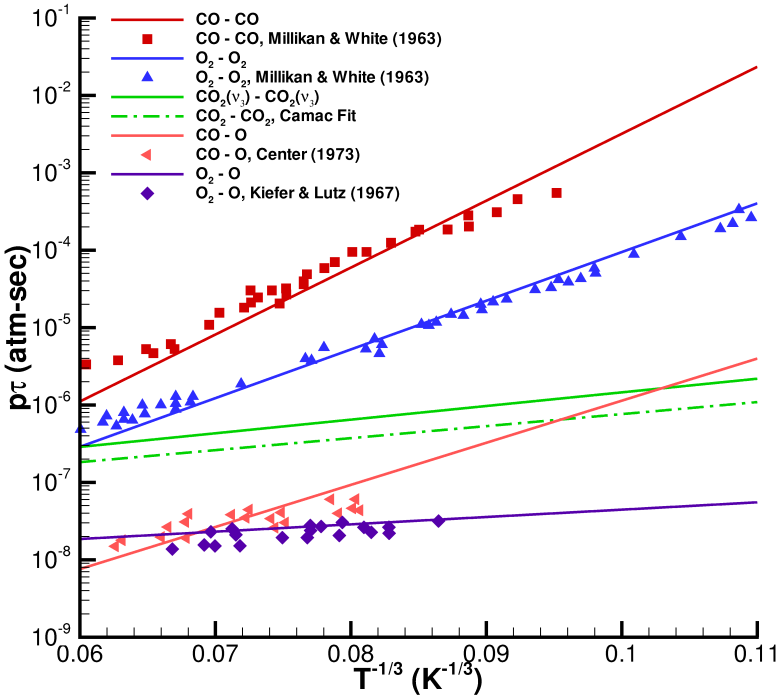

Figure 3.1: Validation of Relaxation times with Experiments.

The only exceptions to the above equation were the relaxation times for the pairs - $CO_2(\nu_3)$-CO, $CO_2(\nu_3)$-O_2 and $CO_2(\nu_3)$-O. Figure 3.2 plots the variation of relaxation times with temperature. The following equation best describes the behavior.

$$p\tau = \frac{T^2 \exp(aT^{-\frac{1}{3}} + b)}{1 - \exp(-\frac{\theta_v}{T})} \qquad [atm.s] \tag{3.10}$$

where θ_v is the characteristic vibrational temperature of the antisymmetric stretch bend (3382 K). This shows that the product of pressure and relaxation time for $CO_2(\nu_3)$, when deactivated by CO, O_2 and O, decreases with decrease in temperature, and the relaxation time was also found to follow the same behavior. The values for constant a and b for different pairs are listed in Table 3.3.

In the next section we will discuss the chemistry and vibration coupling that we used to run the full scale simulations.

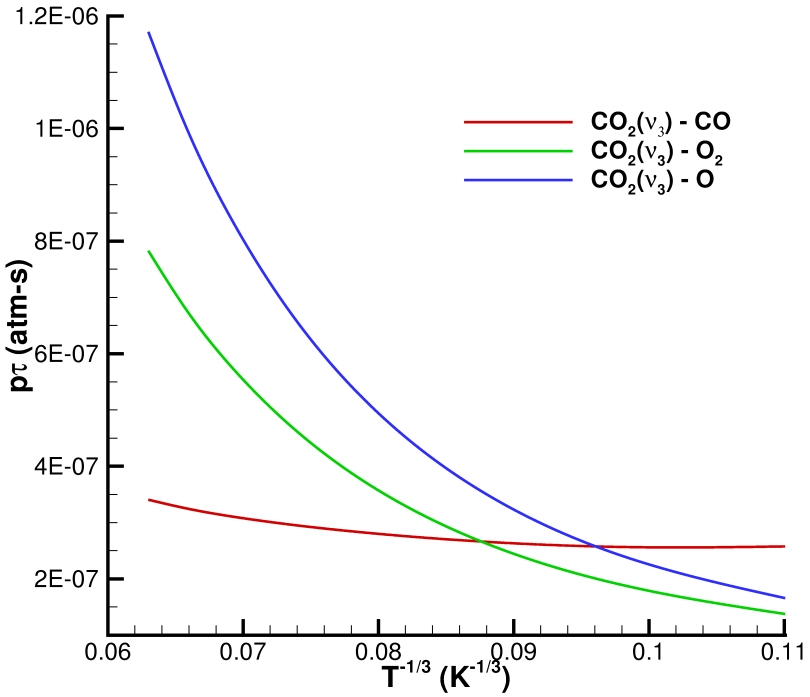

Figure 3.2: Relaxation times for $CO_2(\nu_3)$.

3.3 Chemistry-Vibration Coupling

For the given enthalpy conditions, STANJAN thermodynamic package predicted non-trivial amounts of CO_2, CO, O_2 and O species to be present in the reservoir. Three reactions were identified to be necessary to describe the production/destruction of these species in the CO_2 system.

$$CO_2 + M \rightleftharpoons CO + O + M \tag{3.11}$$

$$O_2 + M \rightleftharpoons O + O + M \tag{3.12}$$

$$CO_2 + O \rightleftharpoons CO + O_2 \tag{3.13}$$

One simple way of coupling chemistry and vibration is to use the modified values of the relaxation times from Table 3.3, and use the Park two temperature model. The

Table 3.3: Values of vibrational constants for CO_2, CO and O_2.

	a	b
CO_2		
M = CO_2	40.58	-17.50
CO	77.01	-36.75
O_2	45.68	-33.96
O	41.07	-33.27
CO		
M = CO_2	9.53	-15.45
CO	199.12	-25.66
O_2	116.76	-20.53
O	125.25	-26.21
O_2		
M = CO_2	153.23	-24.66
CO	162.71	-25.01
O_2	144.88	-23.75
O	21.82	-19.11
M is the colliding partner.		

modified relaxation times are very similar to the Millikan and White fits except for CO_2. As mentioned before, the relaxation times for $CO_2(\nu_3)$ with CO, O_2 or O decrease with decrease in temperature. This model will be called **Model CV-$p\tau$**.

Another way of coupling is to treat the problem as a two step process. The first step would be to solve for the vibrational states from the rate data. The next step would be to sum up the number densities in these vibrational states, and treat the chemistry reactions separately, and then redistribute the total number densities according to the Boltzmann distribution at the local gas kinetic temperature. This is not effective since it does not model the nonequilibrium in the flow, and certainly does not allow population inversion in the vibrational states. So it was necessary to let individual vibrational states participate in the chemical reactions, even though this leads to an extensive set of possibilities. Since each vibrational state is considered to be as a separate species, none of the standard vibration-dissociation models can be used here. Therefore a way of combining the chemistry with the vibrational modes must be formulated.

This chemistry-vibrational coupling model must reflect the following:

- Species at upper vibrational states must show greater tendency to dissociate/react

than the lower lying states.

- Detailed balance must be satisfied in the formulation, i.e. $k_f/k_b = K_{eq}$.

To understand the chemistry-vibration coupling used in the present work, lets consider a simple reaction

$$A(v=i) + M \rightleftharpoons B(v=j) + M \tag{3.14}$$

where species A at i^{th} vibrational level reacts with a collisional partner M to give species B at j^{th} vibrational level. We need to know the expressions for the equilibrium constant ($K_{eq}^{A_iB_j}$) and the forward rate constant ($k_f^{A_iB_j}$). But the data that we do know from literature is the rate constant and the equilibrium constant for the global chemical reaction comprising of all the vibrational states,

$$\mathrm{A} + \mathrm{M} \rightleftharpoons \mathrm{B} + \mathrm{M} \tag{3.15}$$

Let k_f^{AB} be the forward rate constant and K_{eq}^{AB} for the reaction in Eq. (3.15). The backward rate constant is obtained by the principle of detailed balance. We know the equilibrium constants for the following reactions,

$$A(v=0) \rightleftharpoons A(v=i) \qquad K_{eq}^{A_i} = \exp(-\Delta E_i^A/kT) \tag{3.16}$$

$$B(v=0) \rightleftharpoons B(v=j) \qquad K_{eq}^{B_j} = \exp(-\Delta E_j^B/kT) \tag{3.17}$$

where ΔE_i^A and ΔE_j^B denote the energy difference between the ground states of $A(v=0)$ and $B(v=0)$, and the excited states of $A(v=i)$ and $B(v=j)$ respectively. To get the equilibrium constant for the reaction in Eq. (3.14), we need the equilibrium constant of the reaction between the ground states of A and B,

$$A(v=0) + M \rightleftharpoons B(v=0) + M \tag{3.18}$$

which could then be combined with Eqs. (3.16) and (3.17) to yield the desired result. The next step is to get the ground state densities as a function of the total density and the temperature. As discussed in the previous section, the population N_i for a given species in the level i relative to that in the ground state N_0 is given by Eq. (3.1) and the total population in all the states is given by Eq. (3.2). Since the statistical weights

g_i are unity for all the CO, O_2 and the CO_2 antisymmetric stretch levels considered, the expression can be rewritten as,

$$N_{total} = N_0(1 + \Sigma[\exp(-\Delta E_i/kT)]) \tag{3.19}$$

Further, the degree of anharmonicity at the temperatures considered is small, so using the harmonic oscillator model, we can write

$$\Delta E_i = i\Delta E_0 = i\Delta E \tag{3.20}$$

With this assumption, it is then easy to do the summation in Eq. (3.19) as a geometric series (assuming infinite sum).

$$N_{total} = \frac{N_0}{1 - \exp(-\Delta E/kT)} \tag{3.21}$$

Applying this result to obtain a relationship between total density of A and $A(v = 0)$, and similarly for B and $B(v = 0)$, we get,

$$[A] = \frac{[A(v = 0)]}{1 - \exp(-\Delta E^A/kT)} \tag{3.22}$$

$$[B] = \frac{[B(v = 0)]}{1 - \exp(-\Delta E^B/kT)} \tag{3.23}$$

where [X] denotes the concentration of species X. From (3.22) and (3.23), the equilibrium constant for the reaction in Eq. (3.18) is

$$K_{eq}^{A_0B_0} = \frac{[B(v = 0)]}{[A(v = 0)]} = \frac{[B](1 - \exp(-\Delta E^B/kT))}{[A](1 - \exp(-\Delta E^A/kT))} = K_{eq}^{AB}\frac{1 - \exp(-\Delta E^B/kT)}{1 - \exp(-\Delta E^A/kT)} \tag{3.24}$$

Using the results derived above, we can now obtain an expression for the equilibrium constant for the reaction in Eq. (3.14).

$$K_{eq}^{A_iB_j} = \frac{K_{eq}^{B_j}}{K_{eq}^{A_i}}K_{eq}^{A_0B_0} = \frac{\exp(-\Delta E_j^B/kT)(1 - \exp(-\Delta E^B/kT))}{\exp(-\Delta E_i^A/kT)(1 - \exp(-\Delta E^A/kT))}K_{eq}^{AB} \tag{3.25}$$

The expression for K_{eq}^{AB} can be obtained from curve fits available in the literature.

Next we need to obtain the rate constant $k_f^{A_iB_j}$ from the rate constant expression for the global reaction k_f^{AB}. If we consider the classic description of the rate constant,

$$k_f = A_f^{rr}\exp(\frac{-E_{act}^f}{kT}) \tag{3.26}$$

where A_f^{rr} is the pre-exponential factor, E_{act} is the energy of activation and k is the Boltzmann constant. Based on this description, the rate constant, k_f (Eq. (3.26)) is basically the same as $k_f^{A_0B_0}$. The effect of upper vibrational states is to reduce the energy of activation, and thereby increase the rate of the reaction. Using this simple model, we can derive the rate constant expression for the reaction in Eq. (3.14) by altering the energy of activation as needed. The forward rate constant effectively takes the form,

$$k_f^{A_iB_j} = A_f^{rr} \exp(\frac{-(E_{act}^f - \Delta E_i^A)}{kT}) = k_f^{A_0B_0} \exp(\frac{\Delta E_i^A}{kT}) \tag{3.27}$$

and similarly for the backward rate constant we get,

$$k_b^{A_iB_j} = A_b^{rr} \exp(\frac{-(E_{act}^b - \Delta E_j^B)}{kT}) = k_b^{A_0B_0} \exp(\frac{\Delta E_j^B}{kT}) \tag{3.28}$$

The above modification to the rate constants allows the upper vibrational states to have greater tendency to react than the low lying states. Moreover we also see that this derivation is consistent with the principle of detailed balance, i.e.,

$$K_{eq}^{A_iB_j} = \frac{k_f^{A_iB_j}}{k_b^{A_iB_j}} = \frac{k_f^{A_0B_0}}{k_b^{A_0B_0}} \frac{\exp(\frac{\Delta E_i^A}{kT})}{\exp(\frac{\Delta E_j^B}{kT})} = \frac{K_{eq}^{B_j}}{K_{eq}^{A_i}} K_{eq}^{A_0B_0} \text{ (same as (3.25))} \tag{3.29}$$

Next step is to find an expression that relates the rate constants $k_f^{A_0B_0}$ and k_f^{AB}. A nominal correction would be to relate the rate constants as follows,

$$k_f^{A_0B_0} = k_f^{AB}[1 - \exp(-\Delta E^A/kT)]^{-1} \tag{3.30}$$

$$k_b^{A_0B_0} = k_b^{AB}[1 - \exp(-\Delta E^B/kT)]^{-1} \tag{3.31}$$

so that the expressions are consistent with the derivation for the equilibrium constants.

We have outlined the basic principle in obtaining the rate constants and the equilibrium constants for the set of the reactions. It is easy to extend this derivation for reactions with multiple species such as Eq. (3.13). We will denote this way of coupling chemistry and vibration for all the 16 species as **Model CV-16**.

The expressions for the forward rate constants for the chemical reactions (Eqs. (3.11), (3.12) and (3.13)) are of the form,

$$k_f = C_M \exp(-\theta/T) \tag{3.32}$$

Table 3.4: Centerline summary at the test section.

Model	ρ (kg/m^3)	Pressure (Pa)	T (K)	T$_v$ (K)	Mach
Std. model	0.00895	1613.88	892.68	895.69 (all)	5.71587
CV$-p\tau$	0.00933	1706.95	911.11	916.32 (all)	5.68639
CV-16	0.00933	1967.97	1082.30	1082.30 (ν_{SB})	5.41824

The rate constant for the backward reaction is obtained by the principle of detailed balance. The values of these constants are listed in the Appendix (Table A.4). The equilibrium constants are evaluated using curve fits by Mitcheltree et al. [38].

Both Model CV-$p\tau$ and Model CV-16 were used to run the full scale simulations of the nozzle. The standard CO_2 which uses the Park two temperature model and the Landau - Teller model [39] for vibrational relaxation is used to compare the models used in the present work. The Millikan and White fits [18] are used to obtain the relaxation times for all the species except CO_2. Camac rates are used for the vibrational relaxation of CO_2 [40]. Camac rates assume all modes of CO_2 relax together.

3.4 Results and Discussion

3.4.1 Nozzle Flowfield Computations

The coupled vibration - chemistry models were implemented in an axisymmetric CFD solver [19] to calculate the flow field inside the nozzle. The CFD solver uses an excluded volume equation of state to account for the high density effects inside the reservoir. For more information on the CFD solver see Ref. [19]. The reservoir conditions are the same as in Table 3.2. An isothermal wall temperature of 300 K was assumed for the entire nozzle. The results are compared with the standard vibrational model for CO_2. To look at the differences in the flow field prediction between the models, specific values are compared at the test section location. Tables 3.4, 3.5 and 3.6 show the comparison between the standard vibrational model and the models used in the present work.

Table 3.4 shows the comparison of the thermodynamic properties such as pressure, temperature, etc. The models used in the present work predict larger temperatures,

Table 3.5: Mass fractions of species at the centerline test section.

Chemistry Model	CO_2	CO	O_2	O
Standard CO2 model	.8629	.0872	.0497	.000089
Model CV$-p\tau$	.8745	.0798	.0457	3.56E-13
Model CV-16	.9384	.0391	.0225	3.64E-08

Table 3.6: Representative vibrational temperature of species at the centerline at test section for Model CV-16.

Chemical Species	T_v^* (K)
$CO_2(\nu_3)$	1091.14
CO	1104.84
O_2	1245.33

pressures and densities, and therefore lower Mach numbers when compared to the standard model.

The degree of vibrational nonequilibrium is very small for the standard model and Model CV-$p\tau$. The chemical composition of various species do not show much difference between the standard model and Model CV-$p\tau$. The only difference between the standard model and Model CV-$p\tau$ is the modified relaxation times. The vibrational relaxation in both the standard model and Model CV-$p\tau$ is too fast to cause vibrational nonequilibrium in the flow. Moreover, the fast relaxation times obtained for $CO_2(\nu_3)$ deactivation by CO, O_2 or O counter the effect of the slow relaxation of the antisymmetric mode of CO_2 during the expansion in the nozzle. This causes both the standard model and Model CV-$p\tau$ to give similar results.

The chemistry-vibrational coupling used in Model CV-16 predicts larger mass fraction of CO_2 and lower mass fractions of CO and O_2 (Table 3.5). This coupling effectively predicts a composition closer to chemical equilibrium than the other models. Since the stretch-bend modes were assumed to be in equilibrium with the translational and rotational modes, T_v (stretch-bend) is the same as T. The amount of vibrational energy stored can be understood by assigning a representative vibrational temperature (T_v^*) to each of the species $CO_2(\nu_3)$, CO, and O_2. This vibrational temperature is calculated assuming the species as a harmonic oscillator having the same amount of vibrational

energy.

These vibrational temperatures are listed in Table 3.6. These temperatures are purely representative of the vibrational energy content in the respective species. The vibrational temperatures for $CO_2(\nu_3)$, CO and O_2 are larger than the translational temperature because of anharmonicity, and should not be interpreted as the flow being in vibrational nonequilibrium. The number densities in the vibrational levels of $CO_2(\nu_3)$, CO or O_2 were found to follow the Boltzmann distribution at a temperature close to the local translational temperature. Let us consider the amount of vibrational energy stored in the different species for the standard CO_2 model. By using the harmonic oscillator assumption we can derive the total energy content in the species. This value for the standard CO_2 model is 0.2227 MJ/kg. A corresponding calculation for Model CV-16 yields an energy content of 0.3425 MJ/kg in the vibrational modes. This model predicts a larger value for two reasons.

First, the vibrational temperatures are larger than the standard model because of anharmonicity; second, the antisymmetric stretch modes of CO_2 are responsible for most of the vibrational energy, and because a larger mass fraction of CO_2 is predicted by Model CV-16, the vibrational energy content is larger than the standard model. Even though the present model does predict larger vibrational energy content in the free-stream, this is not close to the 42% of the total enthalpy value (2.5025 MJ/kg) recommended in Ref. [1].

To summarize, all the models predict the flow to be close to vibrational equilibrium at the test section. Model CV-16 predicts a flow to be closer to chemical equilibrium than the other two models. In the next section we will look at the effect of these chemistry models on the shock standoff distance.

3.4.2 Shock Standoff Studies

The simulations for the MSL shape were carried using a hybrid, implicit unstructured finite volume solver (US3D) that solves the compressible Navier-Stokes equations [20]. The inviscid fluxes are calculated using a low dissipation version of Steger-Warming flux vector splitting. Second-order accuracy in space is achieved using an upwind biased MUSCL approach [21]. Time integration is performed implicitly using a parallel line relaxation procedure [22]. The MSL shape is a 31 cm diameter, 70° sphere-cone

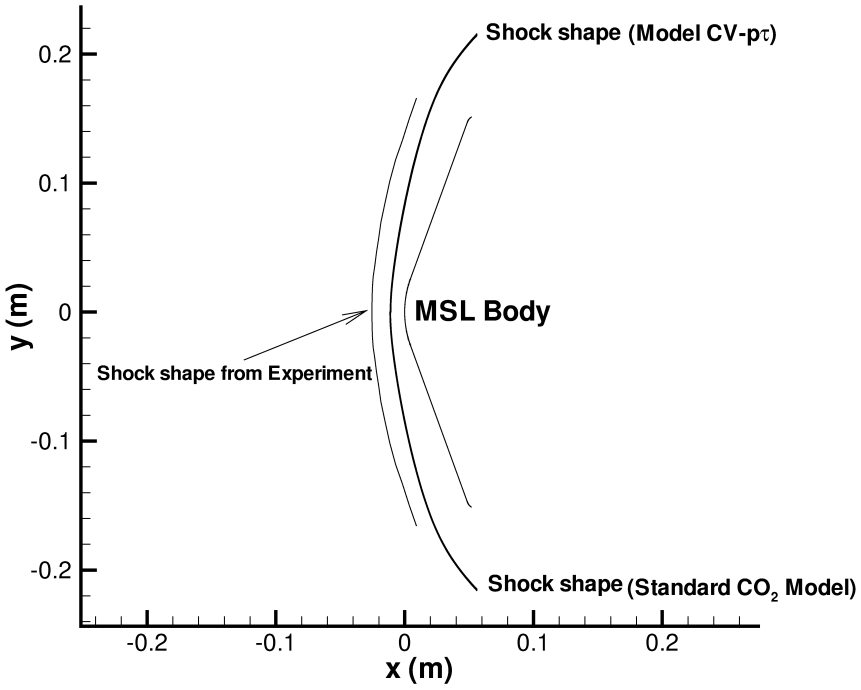

Figure 3.3: Comparison of shock shapes between Standard Model and Model CV-$p\tau$. Shock shape from experiment is indicated in figure.

geometry. The chemistry models, Model CV-$p\tau$ and Model CV-16 were coupled with the flow solver. The test section conditions from the nozzle simulations (Tables 3.4, 3.5) were used for the inflow. The grid used consists of 400 points along the surface and 163 points in the surface normal direction, with points clustered near the shock for better resolution. Isothermal catalytic wall temperature of 300 K was used for the wall. The experimental shock shape is extracted from the Schlieren data in Ref [1]. The shock shape from simulation is obtained from the location of the maximum temperature gradient. These extracted shock shapes are shown in figure 3.3 and 3.4.

Figure 3.3 compares Model CV-$p\tau$ with standard CO_2 model. The inflow conditions are very close to vibrational equilibrium for both the models and the extent of chemical nonequilibrium is also the same, and so the shock standoff distance does not change

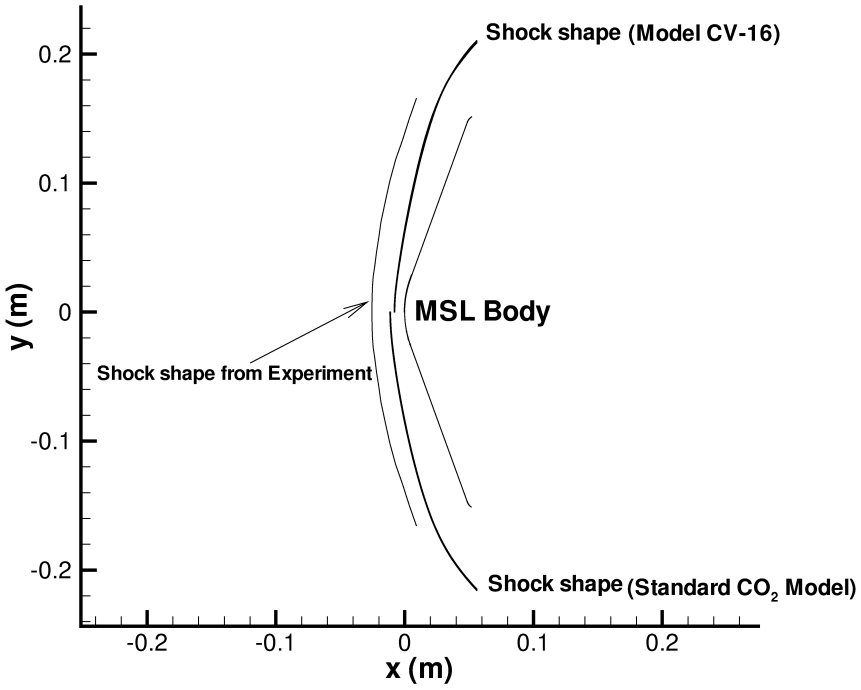

Figure 3.4: Comparison of shock shapes between Standard Model and Model CV-16. Shock shape from experiment is indicated in figure.

between the models. Figure 3.4 shows the comparison between Model CV-16 and the standard CO_2 model. From the nozzle simulations, we know that Model CV-16 predicts the flow at the test section to be closer to chemical equilibrium than the standard model. This is reflected in the shock standoff calculations. The study by Maclean and Holden [1] shows the shock standoff distance to decrease when the composition at the test section is closer to chemical nonequilibrium, and since Model CV-16 predicts a composition closer to chemical equilibrium, the shock standoff distance is smaller despite a lower Mach number. We see that the shock standoff distance is sensitive to the chemistry-vibration coupling model.

3.5 Concluding Remarks

A state specific vibrational model for CO_2, CO, O_2 and O involving 16 species has been formulated and validated against experiments. The antisymmetric stretching mode was decoupled from the symmetric stretching and the bending modes. The symmetric stretching and bending modes were assumed to be in equilibrium with the translational mode. Results show that the antisymmetric mode relaxes more slowly than the other two modes. Additionally, it was found that the relaxation times for the collisional deactivation of $CO_2(\nu_3)$ by CO, O_2 and O increase with temperature. Two methods of chemistry-vibrational coupling were used to simulate the nozzle expansion. The numerical experiments of the vibrational model were used to generate curve fits for the relaxation times. These curve fits were used with a standard chemistry-vibration model for a reduced set of the main four species. This model gave similar results as the standard model, both for the nozzle test section conditions and for the shock standoff distance. The other method included all the 16 state-specific species and a full calculation based on rate expressions for every possible reaction between the species. This method predicted a flow closer to chemical equilibrium at the test section than other models, thereby estimating a decreased shock standoff distance. All the models show that the flow at the test section is close to vibrational equilibrium. This present work uses an advanced state-specific vibrational model that considers the antisymmetric mode separately from the other two modes of CO_2. This approach does not explain the phenomenon of increased shock standoff distance observed in LENS CUBRC facility. Since the advanced modeling of vibrational processes does not resolve the case of increased shock standoff distance in the reflected shock tunnels, the reason for the anomalous behavior must be due to other factors. Possible factors responsible for increased shock standoff distance could be,

- Electronically excited species
- Chemistry-vibrational coupling

Of these factors, we know that chemistry-vibrational coupling affects the shock standoff distance (Figure 3.3 and 3.4). In the next chapters we will look at the effect of both electronically excited states and chemistry-vibrational coupling.

Chapter 4

Role of Electronic States

4.1 Introduction

Following the conclusions from the last chapter where we identified two possible reasons for increased shock standoff distance, i.e. excited electronic states and chemistry - vibrational coupling, in this chapter we focus on the role of excited states in the CO_2 system.

4.1.1 Excited states of CO_2

The problem of CO_2 recombination has been investigated for quite some time (see [8, 41, 42]). The collision between ground state $O(^3P)$ and $CO(^1\Sigma)$ initially produce CO_2 on the excited triplet potential energy surface. The ground state of $CO_2(^1\Sigma_g^+)$ is a linear state whereas the excited $CO_2(^3A)$ is a bent molecule. If the ground state of CO_2 is to dissociate directly, it would necessarily form the excited $O(^1D)$ and $CO(^1\Sigma)$ due to spin constraints. This spin conservation path requires about 2.2 eV more energy than the other path. The observed activation energy for CO_2 is close to the energy separation between the ground state CO_2, and $O(^3P)$ and $CO(^1\Sigma)$. Thus the dynamics for the highly excited ground state CO_2 must allow for the crossing to the triplet state prior to decomposition, and similarly the recombination reaction should also pass through the crossing to the ground state.

The ground and excited states of CO_2 have been described for in detail [8, 42]. The potential surface for CO_2 is shown in Figure 4.1. The reaction paths are shown as solid

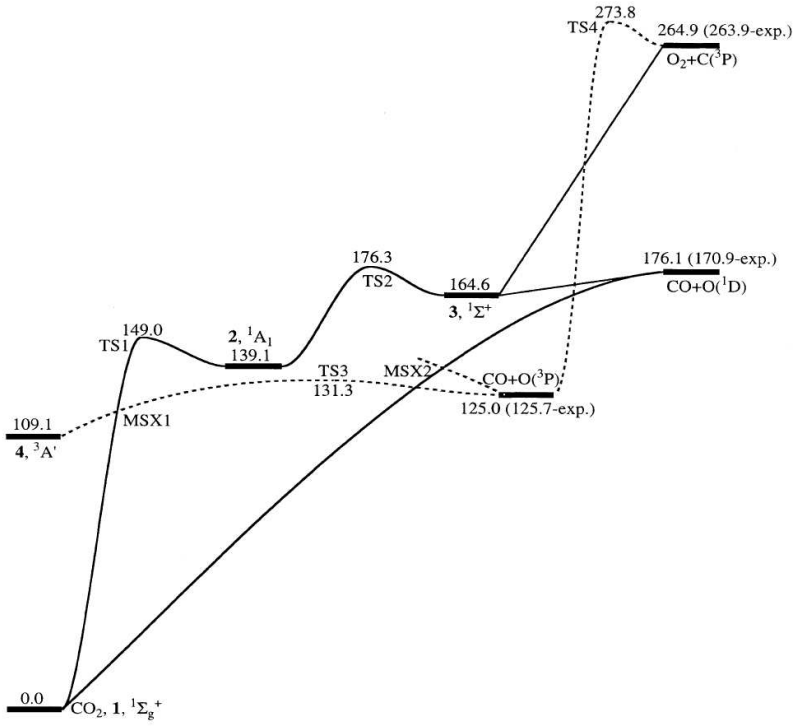

Figure 4.1: Molecular interaction potentials for electronic states of CO_2 at zero rotation. Energies given in kcal/mol w.r.t. ground state CO_2.

lines. The reaction corresponding to ground state $O(^3P)$ with $CO(^1\Sigma)$ is represented by a dotted line. The positions denoted by TS1 and TS2 are transition states, and positions denoted by MSX1 and MSX2 are points of crossing of the ground potential surface with the first excited potential surface. The excited state is a bent state with a bond angle of 120°. The more energetically accessible regions of the singlet-triplet crossing occur for bent configurations at energies around 3.5 eV above the ground state. This means that recombination process not only has to go through the crossing, but also this crossing produces a $CO_2(^1\Sigma)$ with very high excitation particularly in the bending mode. The motions will be very anharmonic and strongly coupled, and all the internal modes relax simultaneously. Also, once the crossing has taken place from the triplet state to the ground state, direct collisional re-dissociation is not probable since it requires additional 2 eV. Recrossing to the triple state is also not favored since the molecule is highly strained in the bending mode, and intramolecular energy transfer will

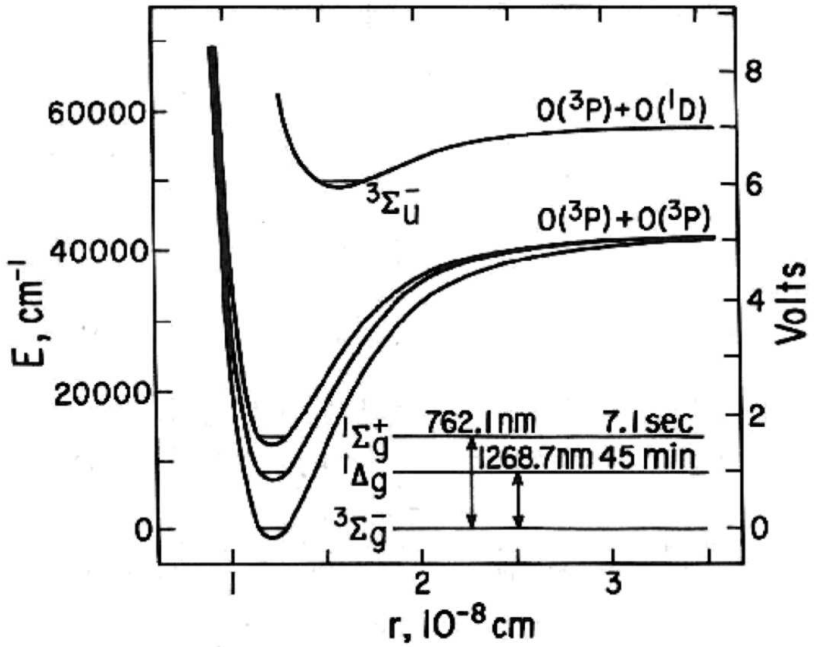

Figure 4.2: Molecular interaction potentials for electronic states of O_2 at zero rotation

occur, rapidly pulling the system away from easy re-access to the triplet state.

The surface hopping frequency is quite high compared to the time between collisions in a typical CO_2 system for the conditions of interest. The elastic collision frequency is between 10^{11} and 10^9 s^{-1}. The surface hopping frequency is comparable to the vibrational frequencies of the excited state $\sim 2\times10^{13}$ [42]. The probability that a system vibrating across the seam makes a transition is about 10^{-2} to 10^{-3}. Hence the rate constant for unimolecular singlet-triplet transition is this probability multiplied by the vibrational frequency (2×10^{10} to 2×10^{11}). This shows that a recombined triplet state is likely to transition to the ground state even before it undergoes a single collision. We know the singlet state is formed in a highly bent configuration with an internal energy of 3.5 eV. This energy redistributes itself among all internal energy modes on the time scale of the vibrational period $\sim 10^{-13}$.

4.1.2 Excited states of O_2

Oxygen also has two low lying electronic excited states: the $a^1\Delta_g$ state is 7918 cm^{-1} (0.98 eV) above the ground state, and the $b^1\Sigma_g^+$ is 13195 cm^{-1} (1.64 eV) above the ground state, compared to a dissociation energy of 5.1 eV. Furthermore these are singlet states and the ground state is a triplet state (X $^3\Sigma_g^-$). Thus transitions to the ground state is spin forbidden, and the a and b states have long radiative lifetimes (60 minutes and 12 seconds respectively [43]). The potential surface diagram for O_2 is shown in Figure 4.2. The singlet b state is likely to be quenched to the singlet a state. Therefore we could expect if a state molecules are formed, they are likely to persist throughout the expansion. From the internuclear diagram for O_2 (Figure 4.2) it is clear that these excited states will play a role in the recombination. The ground state is energetically favored, and in equilibrium, the relative population of the electronic states must correspond to the Boltzmann distribution. However, unlike the CO_2 recombination, the recombination of O atoms has no particular bias toward a specific electronic state apart from their respective degeneracy. The degeneracy of the X, a and b states are 3, 2 and 1 respectively. Thus we would expect roughly half the molecules to recombine to the X state, 1/3 to the a state and 1/6 to the b state.

In a previous work by Nompelis and Candler[6], these excited states were taken into account to assess their role in typical high enthalpy conditions at LENS-I. The authors modeled the rates to be proportional to the degeneracy, and based the rate on the forward reaction rate with the appropriate equilibrium constant for each electronic state. Their analysis gave very low levels of the excited states because the formation of the X state was energetically favored, and predicted similar values for the concentration of various species in the test section. In effect within the constraints of their model, the excited electronic states of O_2 did not play an important role in recombination processes. As we follow similar assumptions in our model, we exclude electronic states of O_2 in this chapter.

4.2 Formulation of the electronically excited species model

We model the mechanism described in previous sections with these reactions,

$$CO_2(A) + M \rightleftharpoons CO + O + M \tag{4.1}$$

$$CO_2(A) \rightleftharpoons CO_2(X) \tag{4.2}$$

$$O_2 + M \rightleftharpoons O + O + M \tag{4.3}$$

$$CO_2(X) + O \rightleftharpoons CO + O_2 \tag{4.4}$$

Note that the exchange reaction is retained with $CO_2(X)$ because the energetics of the reaction prevent the formation of $CO_2(A)$ state. The backward rate constant of reaction (4.1) is the same as the backward rate constant of reaction (3.11). The forward rate constant of reaction (4.1) is calculated by the principle of detailed balance through the equilibrium constant.

The equilibrium constant of reaction (4.1) is given by

$$K_{eq}^{A} = K_{eq}^{X} \times \exp \frac{-\Delta E_{X-A}}{kT} \tag{4.5}$$

where K_{eq}^{X} and K_{eq}^{A} are the equilibrium constants for reactions (3.11) and (4.1) respectively. ΔE_{X-A} is the energy difference between the (X) and the (A) states.

Analysis of reaction (4.2) is a bit involved. The equilibrium constant of this reaction is straightforward, and is equal to $\exp \frac{\Delta E_{X-A}}{kT}$. Since this model will be implemented in the standard model framework, we must make assumptions accordingly especially when determining the value of the forward rate constant. The standard model framework assumes that molecules are formed at the local vibrational temperature. We must view the 'hopping' reaction as a two step process, the first step being the transition from triplet potential surface to the singlet surface with loads of internal energy, and the second step is the redistribution of this energy amongst the different states. From the discussion in the preceding section we know that the transition from triplet to singlet is extremely fast. So, between the two process we can assume that the latter would be the rate determining process. The rate of such a process would be of the order of the vibrational relaxation time scale of the molecules in the ground state. We expect the symmetric and the bending modes to be the preferred modes of relaxation due to the

Table 4.1: Characteristic Vibrational Temperatures for CO_2(A) state

Species	Characteristic Vib. Temperature [K]
CO_2(A) (symmetric mode)	1571
CO_2(A) (bending mode)	864
CO_2(A) (antisymmetric mode)	3378

Table 4.2: Reservoir conditions for the CUBRC run with an effective enthalpy of 5.63 MJ/kg and a pressure of 29.5 MPa.

Temperature	3500 K
ρ	39.9 kg/m^3
cCO_2(X)	0.7737
cCO_2(A)	3.2×10^{-8}
cCO	0.1440
cO_2	0.0786
cO	0.0036

strong Fermi resonance present between the modes. So we choose the Camac rates to be ideal to describe this process. The forward rate constant of reaction (4.2) is given as [40],

$$k_f = 4.19 \times 10^6 \exp \frac{-665.6}{T} \quad (cm^3/mol - s) \tag{4.6}$$

The vibrational modes of the excited electronic state CO_2(A) should also be taken into consideration. Unlike the ground state CO_2, the (A) state CO_2 is not a linear molecule, and therefore has no doubly degenerate bending mode. The characteristic vibrational temperatures are listed in Table 4.1.

This model was used to run the nozzle simulation for the experiment in LENS-I facility. We used the axisymmetric nozzle solver developed by Candler [19] to run the nozzle simulations. The nozzle reservoir conditions are re-listed in Table 4.2 with the concentration of CO_2(A) state included.

Table 4.3: Centerline summary at the test section.

Model	ρ (kg/m^3)	Pressure (Pa)	T (K)	T_v (K)	Mach
Std. CO_2 model	0.00895	1613.88	892.68	895.69 (all)	5.71587
Elec. States model	0.00933	1574.73	767.73	774.45 (all)	5.89399

4.3 Results and Discussion

The predicted test section conditions are listed in Tables (4.3) and (4.4). The translational and vibrational temperature are lower for the electronic states model. The reason is evident from Table 4.4. The mass fraction of CO_2 is lower for the electronic states model. When compared with the reservoir mass fraction of 77%, this shows that there is only a 4% increase in CO_2 for the electronic states model. Also, we note that the concentrations of the other species is higher than the standard model. The chemical nonequilibrium is higher for the electronic states model. There is a substantially more energy stored in the chemical energy in the excited states model: 20.3% of the energy is in the chemical modes for the excited states model as compared to 14.9% for the conventional model. The reduced recombination rate results in lower predicted values of translational and vibrational temperature. This also makes the nozzle exit plane density 4% larger.

The excited state acts as an intermediate state in the formation of ground state CO_2. CO_2(A) state is unstable because it can easily re-dissociate back into CO and O, or hop to the ground state X. The competing rates of these processes set the level of CO_2(A) in the flowfield. Furthermore, the re-dissociation of CO_2(A) removes a portion of the pool of molecules that could have formed CO_2(X); this reduces the rate of recombination and partially accounts for the low level of CO_2. As a result, the flow has substantial chemical nonequilibrium.

We implemented this model in the 3D CFD solver developed at the University of Minnesota [20] and simulated the shock standoff distance for the excited states model and the standard CO_2 recombination model. A comparison of these results is shown in figure 4.3.

Quantitatively, the predicted shock standoff distance increases from 0.051 to 0.092

Table 4.4: Mass fractions of species at the centerline test section.

Model	CO_2(X)	CO_2(A)	CO	O_2	O
Std CO_2 model	.8629	.0	.0872	.0497	.000089
Elec. States model	.8153	3.7334×10^{-12}	.1175	.0651	.001903

base radii for the MSL capsule, whereas the measured experimental standoff distance is 0.165 radii. We notice that the shock standoff distance has increased by almost 100% compared to the standard model, but is still smaller than LENS-I data. This shows that the first excited electronic state of CO_2 should be included in the chemistry, and is very essential in capturing the physics of recombination.

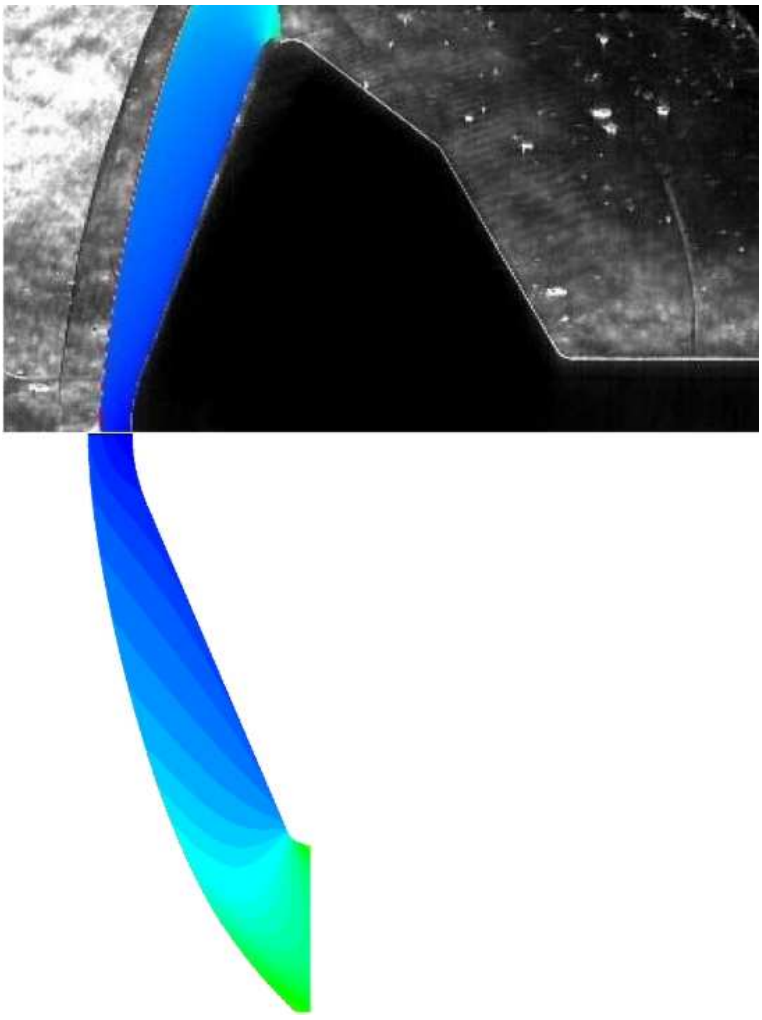

Figure 4.3: Comparison of shock shapes between Standard Model and LENS - I(top) with Electronic States Model (bottom)

Chapter 5

Chemistry-Vibration Coupling in High Enthalpy Flows

5.1 Introduction

In high enthalpy nozzle flows, the expanding flow is often dominated by recombination reactions. Typically these recombining species form molecules that have substantial internal energy. One of the assumptions in nonequilibrium flows is that the atoms recombine to form molecules at the local vibrational temperature. The vibration-vibration relaxation takes place at a much faster rate than other processes enabling the flow to be characterized by a single vibrational temperature. The present work relaxes that assumption by analyzing the flow using a state-specific model. The state-specific model which deals with molecules in each vibrational state as a separate chemical species precludes the need to use a model for vibrational relaxation. The vibration-vibration and vibration-translation processes are treated as chemical reactions. The state-specific approach has been used before to analyze flows in hypersonic nozzles [44, 45] and shock tunnels [46].

In this chapter, we focus on a simple diatomic molecule and consider its vibrational and dissociation/recombination behavior. In the first part of this chapter, we force the recombining species to form a molecule at a pre-defined vibrational energy level. The molecule thereby has substantial internal energy, and then it relaxes through a series of vibration-vibration and vibration-translation processes. Both harmonic and anharmonic

oscillator assumptions are used to describe the relaxation processes. The results are compared with a standard model that employs Park's two temperature model [15]. The inverse problem of dissociation has been handled in a similar way by Josyula and Bailey [47] though they assume dissociation to occur only from the top most vibrational level.

In the second part of this chapter, we use a prior recombination model developed by Kelley [48] that provides a probability distribution function of the recombined states as a function of the total energy available to the system. This prior recombination distribution model takes into account both vibrational and rotational modes of the diatomic molecule. We compare the results of this model with the standard model for the experiments conducted at the LENS CUBRC high enthalpy facility. These experiments were carried out for the double-cone geometry at various enthalpies for different mixtures of Oxygen and Argon. The goal of the experiments was to provide high quality data for investigating the reason behind the mismatch between CFD and experiment at high enthalpy. Preliminary comparison of CFD with the experimental results shows that there is a significant difference ($\sim 15\%$) in the pressure and heat transfer rates over the front portion of the double cone geometry at high enthalpy [7]. In the last part, a reduced model is derived using the concepts of the prior recombination probability distribution. The results of the reduced model are compared with the state-specific approach.

5.2 State-Specific Model

The total number of vibrational levels is constrained by the dissociation energy limit of the diatomic molecule. The diatomic molecule used in this study is the O_2 molecule, since it is easily dissociated at moderate temperatures, making it an ideal candidate to study the recombination process in the nozzle.

In this state specific vibrational model, we have two type of reactions – vibration-translation reactions and vibration-vibration reactions. These are shown in Eqs. (5.1) and (5.2).

$$O_2(v) + M \rightleftharpoons O_2(v-1) + M \tag{5.1}$$

$$O_2(r) + O_2(s) \rightleftharpoons O_2(r-1) + O_2(s+1) \tag{5.2}$$

The rate constants for these vibration-translation and the vibration-vibration processes are obtained using Schwartz, Slawsky and Herzfeld theory [32]. They are of the form,

$$k_f = C \exp(-B/T^{1/3}) \tag{5.3}$$

where B scales as the transition frequency ν raised to the 2/3 power for the vibration-translation processes. As for the vibration-vibration transfer, based on the study by Jeffers and Kelley [33] using short scale interactions, it was found that B scales as ν raised to 0.6. For most of the processes, this expression provides a good fit, especially for temperatures larger than 500 K. The reverse rates are obtained by the principle of detailed balance.

$$k_b = k_f \exp(-\Delta E/kT) \tag{5.4}$$

The ΔE values of the processes are obtained from spectroscopic data [34, 35]. The value of the Boltzmann constant k when ΔE is expressed in cm^{-1} is 0.695.

The rate constant for the basic V-T and V-V processes are listed in Table 5.1. The scaling for upper states for the V-T processes follows the harmonic scaling,

$$k_f^{v,v-1} = v k_f^{1,0} \tag{5.5}$$

For the V-V processes the scaling is as follows,

$$k_{f\,s,s+1}^{r,r-1} = \frac{r(s+1)}{2} k_{f\,1,2}^{1,0} \tag{5.6}$$

Note that Eq. (5.6) relates $k_{f\,s,s+1}^{r,r-1}$ to $k_{f\,1,2}^{1,0}$ instead of $k_{f\,0,1}^{1,0}$, as the process corresponding to $k_{f\,0,1}^{1,0}$ is trivial in the present system. The value of B scales with transition frequency as described earlier. We do not consider multi-quantum transfers in the present work. This type of scaling for the rate constants has shown to provide good agreement with experiments for the relaxation times [45].

O_2 is treated as either an harmonic or an anharmonic oscillator in this study. For the harmonic oscillator case, the energy distribution is assumed to be uniformly spaced at 1550 cm^{-1}; this yields 26 vibrational levels using the dissociation energy as the upper limit. For the anharmonic case, the following Dunham expression [34] is used to find the energy spacing.

Table 5.1: Rate constant data for the basic V-T and V-V processes of O_2.

Reaction	C (cm^3/s)	B	Source
V-T process			
$O_2(v{=}1) + O \rightleftharpoons O_2(v{=}0) + O$	$3.4{\times}10^{-9}$	67.5	[49, 50]
$O_2(v{=}1) + O_2 \rightleftharpoons O_2(v{=}0) + O_2$	$3.6{\times}10^{-7}$	190.0	[18]
V-V process			
$O_2(v{=}1) + O_2(v{=}1) \rightleftharpoons O_2(v{=}0) + O_2(v{=}2)$	$4.0{\times}10^{-13}$	14.38	[36]

Table 5.2: Anharmonic constants in cm^{-1} for the Dunham expression of O_2.

ω_e	1580.0
$\omega_e x_e$	11.98
$\omega_e y_e$	0.0474
$\omega_e z_e$	-0.00127

$$E(v) = \omega_e(v+1/2) - \omega_e x_e(v+1/2)^2 + \omega_e y_e(v+1/2)^3 + \omega_e z_e(v+1/2)^4 \tag{5.7}$$

Using this expression for energy spacing we obtain 36 vibration levels. The values of the various anharmonic coefficients are listed in Table 5.2. Note that rotation-vibration coupling is ignored in this model.

The only chemical reaction considered in the present work is the recombination of O atoms to the 'v_{chem}' vibrational level,

$$O + O + M \rightleftharpoons O_2(v_{chem}) + M \tag{5.8}$$

The rate constant for the recombination reaction is chosen as [51]

$$k_f = 2.2 \times 10^{13} \exp(890.0/T) \tag{5.9}$$

The backward rate constant is determined by the principle of detailed balance.

The equilibrium constant for the reaction, following the procedure in Reference [45] is,

$$K_{eq}^{v} = K_{eq} \exp(-\Delta E_{v_{chem}}/kT)(1 - \exp(\Delta E_{v=1}/kT)) \tag{5.10}$$

where $\Delta E_{v_{chem}}$ is the energy difference between the ground state and the vibration level v_{chem}. The above expression is strictly true only for harmonic oscillators.

Note that there is no correction to the rate constant based on the vibration level v_{chem}. The effect of the vibration level v_{chem} is accounted in the backward rate constant through the equilibrium constant.

5.2.1 Results: Preliminary Test Case

Validation studies were carried out for the vibrational model similar to the study in Chapter 2. The relaxation times were compared to experiments for O_2-O_2 and O_2-O pairs (Figure 5.1). The solid lines are the best fit curves corresponding to numerically generated relaxation times using a zero-dimensional code. Again we find that there is very good match with the experiments. The inclusion of upper vibrational states does not affect the relaxation time significantly. This is because the relaxation/reaction between upper vibrational states is faster than the low lying states due to rate constant scaling. The transition between the low lying states determines the net rate of relaxation. Thus the results between the vibrational model in Chapter 2 (Figure 3.1) and the present section are very similar.

The state-specific model was implemented in the axisymmetric nozzle code [19]. The nozzle geometry chosen for this work is the LENS-I hypersonic nozzle at CUBRC [2]. Selected cases of the vibrational level v_{chem} to which O atoms preferentially recombine are listed in Table 5.3. The values of the vibrational level for anharmonic cases were chosen to match the energy values of the harmonic cases. For the test case, the reservoir conditions are $P_0 = 100.0$ bar and $T_0 = 5000$ K, with 66% O_2 present. The results are listed in Tables 5.4 and 5.5. The results are compared with the Park two temperature chemistry-vibrational coupling model. In this standard model, the Landau - Teller model [39] is used for vibrational relaxation with Millikan and White fits [18] for the relaxation times. The standard model assumes that the recombined molecules form at the local vibrational temperature. This means that the population distribution of the states follow a Boltzmann distribution, i.e. the population at the lower states always being larger than the upper vibrational states.

Though the truncated harmonic oscillator assumption is not a good representation of a dissociating diatomic molecule, it is included as a reference point The first observation

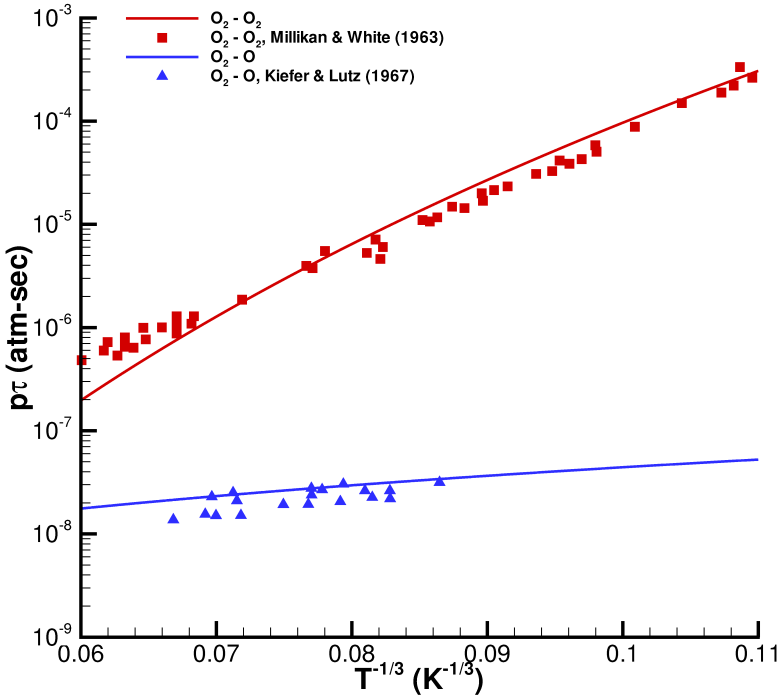

Figure 5.1: Comparison of Relaxation times for O_2-O_2 and O_2-O pairs with experiments

between the harmonic and anharmonic cases is that the macroscopic variables such density, temperature and mass fraction do not differ by much (differences less that 2%. Temperature and mass fraction go down as the value of 'v_{chem}' increases. At the max 'v_{chem}', the composition is very close to the reservoir conditions showing that the flow is chemically frozen, though there is some vibrational relaxation. This shows if the O atoms are forced to combine to the top vibrational levels, that reaction is not favored, and this results in almost the same composition in the test section as in the reservoir.

The major difference is that these macroscopic quantities vary significantly from the standard model results. The vibrational temperature T_v in the standard TT_v model is larger and the mass fraction of O_2 is 10% - 20% higher depending on 'v_{chem}'. The translation temperature in the standard model is larger because more of O atoms have recombined to form O_2.

Table 5.3: Pre-defined vibrational levels 'v_{chem}' for harmonic and anharmonic cases

Harmonic case	Anharmonic case
5	5
10	11
15	17
20	24

Table 5.4: Comparison of flow variables at the test section for Harmonic Oscillator case.

v_{chem}	ρ (kg/m^3)	T (K)	T_v (K)	Mass frac. of O_2
5	0.001848	279.63	1665.17	0.7834
10	0.002278	181.94	1601.02	0.7167
15	0.002596	160.27	1581.50	0.6905
20	0.002799	146.95	1563.45	0.6732
Standard Model	0.001819	815.70	1751.97	0.9099

Next we consider the population distributions for the harmonic and the anharmonic oscillator cases. For the sake of uniformity, we compare the populations at the test section for both cases. Figures 5.2 and 5.3 show the distribution in a log plot. As expected the distribution follows a Boltzmann distribution for the harmonic oscillator case. In Fig. 5.3b, we see non-Boltzmann distributions characteristic of anharmonicity. The populations in the anharmonic upper levels are lower than the corresponding values for the harmonic case.

Another computational experiment was carried out assuming all states have an equal probability of O_2 formation, i.e. no preferential recombination to a specific state. The results are tabulated in Table 5.6. The macroscopic variables such as density, temperature and mass fractions are very close to each other. The results suggest that a broad distribution in vibrational levels after recombination is more consistent with the standard model than recombination into any specific level.

To summarize, anharmonic or harmonic oscillator cases both give similar results for all cases, and having preferential recombination shows a significant difference compared to the standard model.

Table 5.5: Comparison of flow variables at the test section for Anharmonic Oscillator case.

v_{chem}	Density (kg/m^3)	Temperature (K)	Mass fraction of O_2
5	0.001829	289.48	0.7860
11	0.002258	183.48	0.7158
17	0.002555	162.40	0.6907
24	0.002753	149.23	0.6738
Standard Model	0.001819	815.70	0.9099

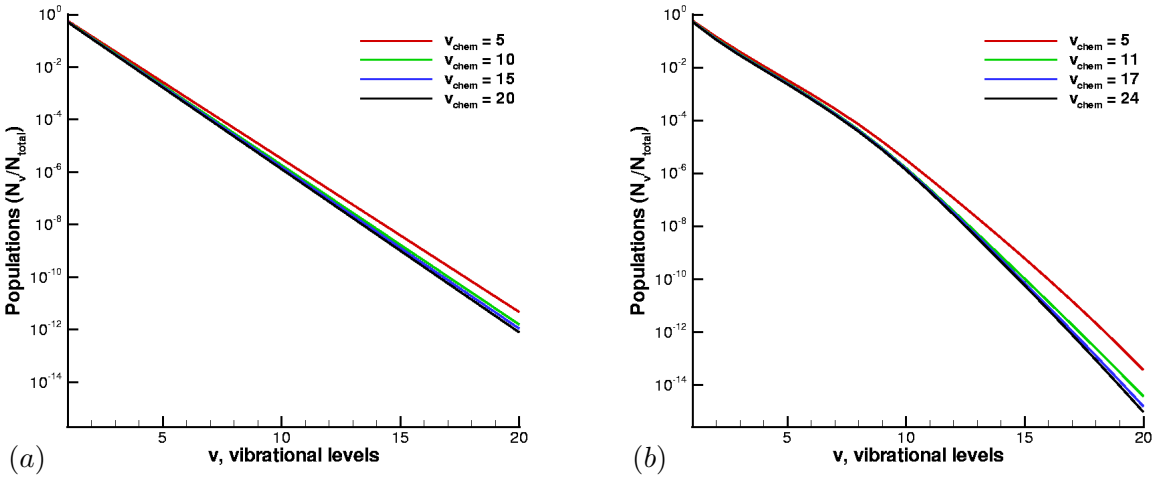

Figure 5.2: Population Distribution as a function of vibrational levels, v, at the test section for (a) Harmonic and (b) Anharmonic cases.

5.3 Prior Distribution of Molecular States

In this section we examine how the calculated test conditions vary if we assume a broad, nonuniform distribution of recombined states rather than the distributions discussed above. The distribution here is the so-called 'prior' based on an information theoretic approach [52] to chemical reactions. The conventional treatment [52] has been modified [48] to describe 3-body atom recombination. The prior state distribution of recombined products is that which maximizes the entropy of the 3-body system consistent with normalization, conservation of total system energy, E_{total}, and angular

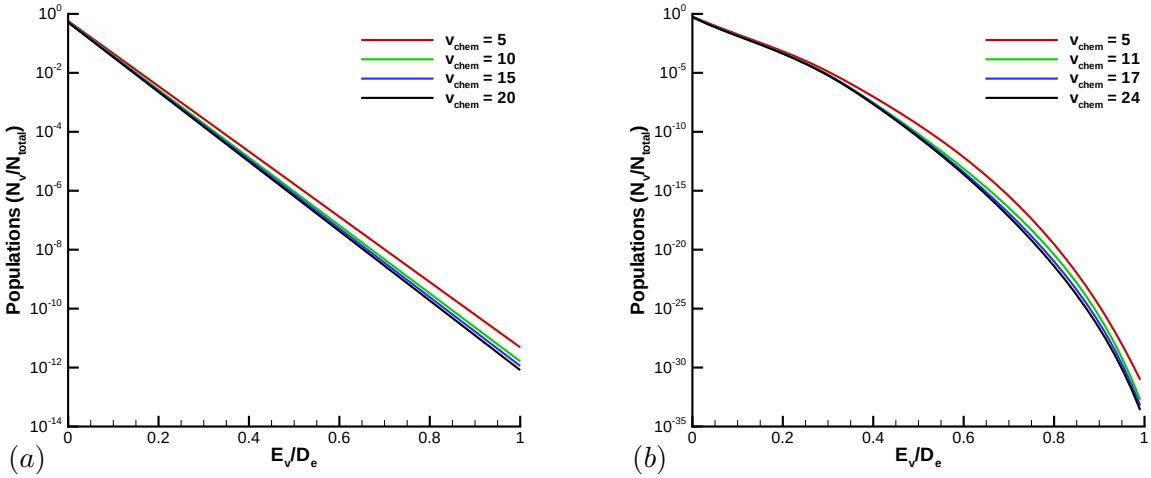

Figure 5.3: Population Distribution as a function of reduced vibrational energy, E_v/D_e, at the test section for (a) Harmonic and (b) Anharmonic cases.

Table 5.6: Comparison of Flow variables at the test section for No-Pref Basic model and the Standard model.

Model	Density (kg/m^3)	Temperature (K)	Mass fraction of O_2
Standard Model	0.001819	815.70	0.9099
No-Pref Basic Model	0.001863	754.53	0.8971

momentum (J), with no other assumptions about the dynamics. For a recombining 3-body system, the total energy is given by

$$E_{total} = D_e + E_{tr} \tag{5.11}$$

where E_{tr} is the initial relative translational energy of the three atoms. This E_{tr} is evaluated as c_{v_O}T, where c_{v_O} is the translational specific heat of the O atoms. The translational energy of the third-body collision partner is also added to E_{tr}. The final recombined diatomic distribution is given in terms of E_{int}, the total internal energy; and depends implicitly on J. The effect of J is to bias the distribution toward large E_{int} values because of the (2J+1) degeneracy factor for the high J values accessible at large E_{int}. Note that the variables employed to create the distribution are total

diatomic internal energy and angular momentum, not the more common vibrational and rotational energies. Vibration and rotation are no longer separable motions as the internal energy approaches D_e, but total internal energy and angular momentum retain their meaning.

5.3.1 Preliminary Recombination Model

We have constructed prior distributions for O_2 as shown in Fig. 5.4. These distributions represent occupation probabilities in energy bands about 2600 cm^{-1} wide.

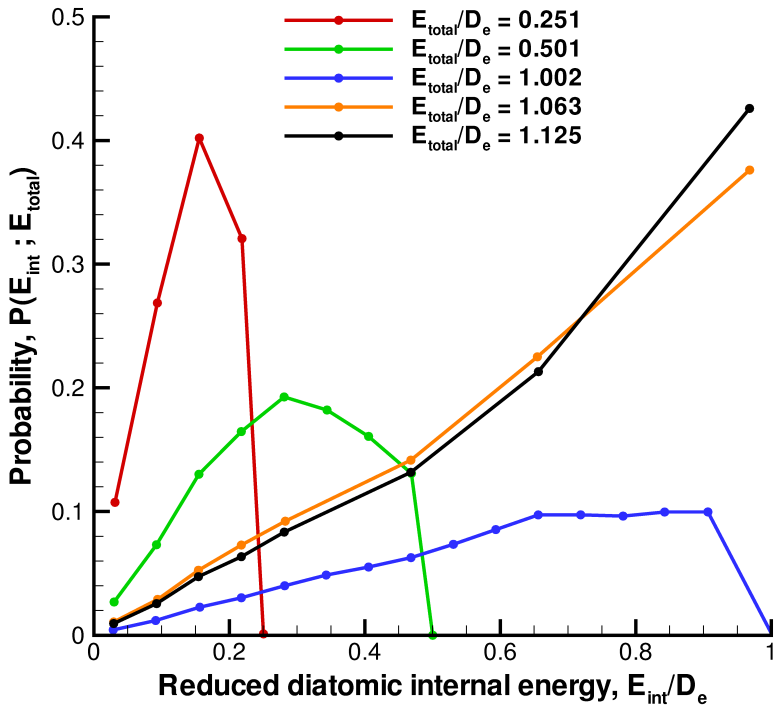

Figure 5.4: Prior distribution of product diatomic energy states for various total energies

In constructing these distributions we have made the additional assumption that the relaxation process between the isoenergetic states $E_{int}(v(J),J)$ and $E_{int}(v(0),J{=}0)$ is faster than the relaxation of vibrational states to equilibrium. This effectively removes the dependence of the internal energy on the rotational quantum number J, and focuses

on the vibrational states for the $J = 0$ potential surface. It is for this reason we have ignored data points for E_{int}/D_e greater than 1 (Fig. 5.4). A preliminary recombination model could then be constructed using the plots in Fig. 5.4 using the following procedure. For each E_{total}, polynomial curve fits of the population distributions are constructed. Since we know energies of the $J = 0$ potential surface using the Dunham expression (Eq. 5.7), we sample the probabilities using curve fits for the individual vibrational states for various total energies. This set of new sampled probabilities must be renormalized to ensure that the sum is 1. E_{total} for a given recombination reaction can be calculated using Eq. 5.11. The probabilities for each vibrational state for that E_{total} can be obtained through interpolation using the probabilities obtained from the plots in Fig. 5.4. In the implementation, we consider only the anharmonic case. This is because the test section conditions between the harmonic and anharmonic cases are not very different (Tables 5.4, 5.5). As stated earlier, there are a total of 36 vibrational states for the anharmonic case. Figure 5.5 shows the probabilities as a function of E_{total}/D_e for various vibrational states for the O_2 system.

In this figure we notice that upper states are not populated for low total energy and lower states are not populated for high total energy. Note that for recombination process, E_{total}/D_e is always greater than 1.

Once the probability distribution is obtained, the recombination rate constant for reaction (Eq. (5.8)) is given by

$$k_f(v) = k_f \times P(v, E_{total}) \tag{5.12}$$

where $\mathrm{P}(v, E_{total})$ is the probability for a vibrational state v for a given total energy E_{total}. The equilibrium constants for each state-specific recombination reaction are obtained as described in Section 5.2.

5.3.2 Results: Prior Distribution Model

The preliminary recombination model was incorporated into the axisymmetric nozzle code [19]. We compare the test sections for the set of experiments carried out at the LENS CUBRC facility for Oxygen - Argon mixtures. The experimental conditions cover a range of enthalpy conditions and at the same time vary the composition of the Oxygen - Argon mixtures. Table 5.7 provides the reservoir conditions for the different

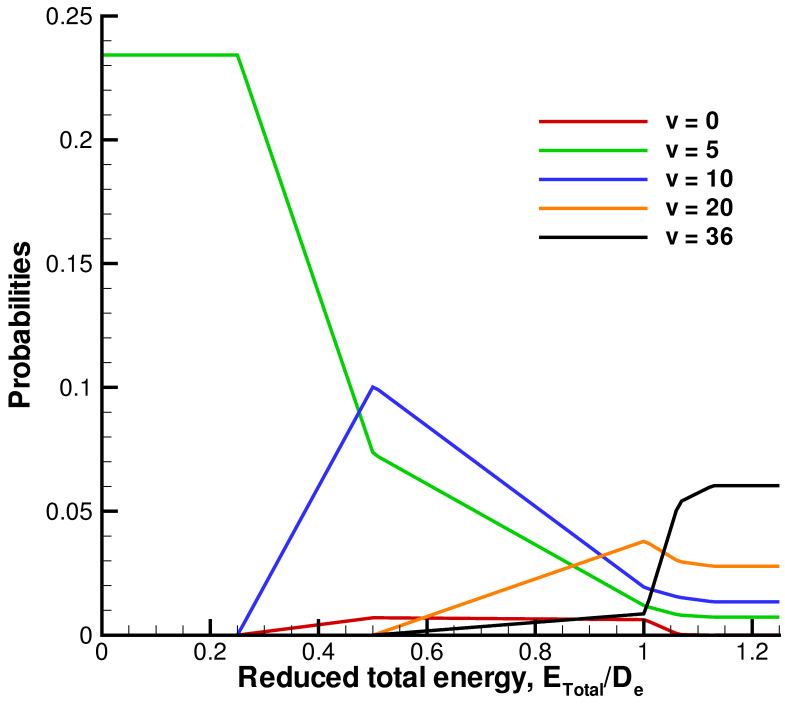

Figure 5.5: Probabilities as a function of reduced total energy E_{total}/D_e for various vibrational states

runs considered in the present work. The test section conditions are given in Table 5.8. The test section location is 6.26 m from the throat. The vibrational temperature for the anharmonic oscillator is obtained by calculating the equivalent temperature that provides the same population distribution.

For all cases, the vibrational temperature at the test section is larger than the predicted value by the standard model. The standard model assumes that the recombining molecules are formed at the local vibrational temperature. Therefore, if we assume a Boltzmann distribution, this implies that the population of the lower vibrational states is higher than that of the upper vibrational states. This will produce a larger translational temperature for the standard model because it promotes recombination to the lower states. The prior recombination distribution model on the other hand uniformly predicts larger vibrational temperature for all the cases. This is because when the

Table 5.7: Run Matrix for high enthalpy O_2 runs - Reservoir conditions

Run	Enthalpy [MJ/kg]	O_2/Ar	ρ_0 [kg/m^3]	T_0 [K]	Mass fraction (O_2)
81	6.4	50/50	5.2426	4645.05	33.96%
82	8.1	50/50	6.2898	5159.75	26.34%
84	9.3	50/50	5.8147	5448.55	20.74%
85	10.1	75/25	5.7715	5157.95	43.30%
88	8.7	100/0	6.8643	4673.61	77.95%
90	4.0	100/0	10.315	3379.65	98.12%
91	10.2	100/0	10.322	5080.23	71.69%

flow exits the reservoir, the total energy available to the system is very large, forcing recombination into the upper states. The total energy is large due to the elevated temperature and O atom mass fraction. As the flow expands, the translational temperature reduces, bringing down the value of total energy. The chemistry time scales competes with the flow time scale producing nonequilibrium flowfield (there is freezing of chemical and vibrational energy shortly after the flow exits the reservoir). At lower enthalpy, such as Run 90, the difference between the vibrational temperatures predicted by the standard model and the prior recombination distribution model is the smallest. The translational temperature and mass fraction of O_2 are very similar for both models. For higher enthalpy cases such as Run 84 or Run 85, the vibrational temperature predicted by the prior recombination distribution model is almost triple the value predicted by the standard model. Because most of the energy is locked up in the vibrational modes, the translational temperature is smaller for the prior recombination distribution model. The velocities are also uniformly lower than the standard model, but the difference is not as large as in the case of translational and vibrational temperatures.

5.4 Further Analysis in Chemistry-Vibrational Coupling

In this section, we look at the inner workings of any chemistry-vibrational model in a generalized system. From preceding sections, we know the general physics behind recombination of atoms. When two atoms recombine to form a molecule, the energy available to the molecule at the time of formation will place it at an appropriate internal energy state. From that state, it strives towards equilibrium through vibrational

Table 5.8: Comparison of test section conditions between Standard Model and Prior Recombination Model

Model	ρ [kg/m^3]	T [K]	T_v [K]	Mass frac. (O_2)	u [m/s]
Run 81					
Standard Model	9.234×10^{-4}	275.8	760.40	47.4%	3399.95
Recombination Model	1.030×10^{-3}	192.9	1929.1	45.45%	3297.92
Run 82					
Standard Model	1.045×10^{-3}	391.1	660.3	45.45%	3768.99
Recombination Model	1.167×10^{-3}	247.2	2031.5	42.72%	3650.83
Run 84					
Standard Model	9.620×10^{-4}	452.1	646.9	43.31%	3972.64
Recombination Model	1.096×10^{-3}	261.6	2150.2	39.64%	3830.68
Run 85					
Standard Model	9.243×10^{-4}	586.2	687.3	66.54%	4080.48
Recombination Model	9.495×10^{-4}	372.3	2007.7	64.06%	3997.57
Run 88					
Standard Model	1.061×10^{-3}	569.8	697.5	94.82%	3853.3
Recombination Model	1.024×10^{-3}	428.2	1781.44	94.36%	3826.76
Run 90					
Standard Model	1.834×10^{-3}	190.1	1009.6	99.85%	2731.1
Recombination Model	1.907×10^{-3}	175.6	1315.4	99.87%	2719.8
Run 91					
Standard Model	1.543×10^{-3}	728.9	773.1	93.88%	4147.5
Recombination Model	1.568×10^{-3}	568.9	1784.2	93.12%	4125.9

exchanges within the molecule. These could be vibrational - vibrational exchanges or vibrational - translational exchanges. If the internal energy of the newly formed molecule is large enough, it could also re-dissociate. The focus in this section is to produce a model that reflects the prior recombination distribution model, but with a reduced set of variables. We assume that the rotational relaxation is faster than vibrational relaxation. This way we can represent the internal energy of a molecule by its vibrational quantum number.

5.4.1 Basics

We carry out the following exercise as we are interested in the kinetics of O_2. The same procedure can be extended to any diatomic molecule. The key processes in a

dissociating O_2 system are,

$$O_2(v) + M \rightleftharpoons O + O + M \tag{5.13}$$

$$O_2(v) + O_2(w) \rightleftharpoons O_2(v-1) + O_2(w+1) \tag{5.14}$$

$$O_2(v) + M \rightleftharpoons O_2(v-1) + M \tag{5.15}$$

These are dissociation/recombination reaction for v state, V-V processes and V-T processes. The rates of formation of O_2 from each of these processes are listed below

$$\frac{d}{dt}[O_2^v]_{chem} = k_{1b}^v[O][O][M] - k_{1f}^v[O_2^v][M] \tag{5.16}$$

$$\frac{d}{dt}[O_2^v]_{VV} = \Sigma_w(k_{2b}^{v,w}[O_2^{w+1}][O_2^{v-1}] - k_{2f}^{v,w}[O_2^w][O_2^v]) \tag{5.17}$$

$$\frac{d}{dt}[O_2^v]_{VT} = k_{3b}^v[O_2^{v-1}][M] - k_{3f}^v[O_2^v][M] \tag{5.18}$$

Now the total rate of formation of O_2 is given by the sum of the rates of production due to each individual reaction.

$$\frac{d}{dt}[O_2] = \sum_v \frac{d}{dt}[O_2^v] = \sum_v \frac{d}{dt}[O_2^v]_{chem} + \sum_v \frac{d}{dt}[O_2^v]_{VV} + \sum_v \frac{d}{dt}[O_2^v]_{VT} \tag{5.19}$$

Now by construction, the rate of production of O_2 due to processes within the vibrational manifold should be zero, because O_2 can be produced only by the chemical reaction. So ignoring the relaxation processes within the vibrational manifold for now, we obtain

$$\frac{d}{dt}[O_2] = \left(\sum_v k_b^v\right)[O][O] - \left(\sum_v k_f^v \frac{[O_2^v]}{[O_2]}\right)[O_2] \tag{5.20}$$

Note that we have absorbed the effect of the third body in the value of the rate constant. Now for the global recombination reaction,

$$O_2 \rightleftharpoons O + O \tag{5.21}$$

the rate of formation of O_2 is given by,

$$\frac{d}{dt}[O_2] = k_b[O][O] - k_f[O_2] \tag{5.22}$$

Comparing the R.H.S of Eqs. (5.20) and (5.22),

$$\left(\sum k_b^v\right)[O][O] - \left(\sum k_f^v \frac{[O_2^v]}{[O_2]}\right)[O_2] = k_b[O][O] - k_f[O_2] \tag{5.23}$$

We now start with the first set of assumptions.

- The rate constants k_f, k_b, k_f^v and k_b^v are independent of the [O] and [O_2] concentrations. This is a reasonable assumption since in most cases we find that the rate constants are of the Arrhenius form. We also note here that the rate constants k_f^v and k_b^v may have a dependence on the vibrational state 'v' or 'E_v'.

- The next assumption is that the ratio $\frac{[O_2^v]}{[O_2]}$ is independent of the concentrations of [O] and [O_2]. This ratio can be described in most cases by the parameters of the vibrational distribution function. For example, the ratio is a function of T_v in the case of an harmonic oscillator.

The above assumptions are necessary to justify the following equality. Since Eq. (5.23) is true for all values of [O] and [O_2], and the coefficients are independent of the concentrations,

$$\sum_v k_b^v = k_b \qquad\qquad \sum_v k_f^v \frac{[O_2^v]}{[O_2]} = k_f \tag{5.24}$$

The equation (5.24) can also be viewed as a statement of probability.

$$\sum_v k_b^v = k_b \Rightarrow \sum_v \frac{k_b^v}{k_b} = \sum_v \mathcal{P}_b^v = 1 \tag{5.25}$$

$$\sum_v k_f^v \frac{[O_2^v]}{[O_2]} = k_f \Rightarrow \sum_v \frac{k_f^v}{k_f} \frac{[O_2^v]}{[O_2]} = \sum_v \mathcal{P}_f^v = 1 \tag{5.26}$$

where $\mathcal{P}_b^v$ is the probability that $O_2(v)$ was created from O atoms. Similarly, $\mathcal{P}_f^v$ is probability that O atoms dissociated from $O_2(v)$.

Now revisiting Eq. (5.24), we see that the expressions obtained for k_f and k_b are the nonequilibrium rate constants for the reaction. Its important to note that though the vibrational relaxation within the manifold does not affect the rates explicitly, they have an implicit effect through the factor $\frac{[O_2^v]}{[O_2]}$. This ratio is determined by the rate at which vibrational relaxation takes place within the manifold. Now let us consider the system in equilibrium so as to obtain the relationship between k_f and k_b at equilibrium. Note that at equilibrium, the rate of production of O atom is zero which necessitates that the rate of production of $[O_2^v]_{chem}$ be zero as well. This simplifies the derivation of the relationship between k_f^v and k_b^v.

The superscript * refers to equilibrium values. Total concentration of O_2 is given by the following expression,

$$[O_2]^* = \sum_v [O_2^v]^* \tag{5.27}$$

where,

$$[O_2^v]^* = [O_2^0]^* \exp(-E_v/kT) \tag{5.28}$$

Therefore the total sum can be expressed as,

$$[O_2]^* = [O_2^0]^* \sum_v \exp(-E_v/kT) = [O_2^0]^* \mathcal{Q}(T) \tag{5.29}$$

$\mathcal{Q}(T)$ is the vibrational partition function evaluated at T. The equilibrium constant for the global reaction is given by,

$$K_{eq} = \frac{[O]^*[O]^*}{[O_2]^*} \tag{5.30}$$

The equilibrium constant for the elementary reaction is given by

$$K_{eq}^v = \frac{[O]^*[O]^*}{[O_2^v]^*} = \frac{[O]^*[O]^*}{[O_2]^*}\frac{[O_2]^*}{[O_2^v]^*} = K_{eq}\frac{[O_2]^*}{[O_2^0]^*}\frac{[O_2^0]^*}{[O_2^v]^*} = K_{eq}\mathcal{Q}(T)\exp(E_v/kT) \tag{5.31}$$

The principle of detailed balance is valid for the elementary reaction and is given by,

$$\frac{k_f^v}{k_b^v} = K_{eq}^v = K_{eq}\mathcal{Q}(T)\exp(E_v/kT) \tag{5.32}$$

So we get the expression relating k_f^v and k_b^v as

$$k_b^v(v,T) = k_f^v(v,T)\frac{\exp(-E_v/kT)}{K_{eq}\mathcal{Q}(T)} \tag{5.33}$$

Going back to Eq. (5.24),

$$k_f = \sum_v k_f^v \frac{[O_2^v]}{[O_2]} \tag{5.34}$$

Under nonequilibrium conditions, the ratio $\frac{[O_2^v]}{[O_2]}$ is a function of the vibrational distribution chosen. For harmonic oscillator it is a function of the vibrational temperature T_v. For convenience, let us call the ratio $\mathcal{R}(T, \alpha_1^v, \alpha_2^v, ...)$, where $\alpha_1^v, \alpha_2^v, ...$ are the parameters of the vibrational distribution.

$$k_f = \sum_v k_f^v \mathcal{R}(T, \alpha_1^v, \alpha_2^v, ...) \tag{5.35}$$

Note that under equilibrium conditions, the value of this ratio is given by,

$$\mathcal{R}_{eq}(T, \alpha_1^v, \alpha_2^v, ...) = \frac{\exp(-E_v/kT)}{\mathcal{Q}(T)} \tag{5.36}$$

Now, for k_b

$$k_b = \sum_v k_b^v = \sum_v \frac{k_f^v \exp(-E_v/kT)}{K_{eq}\mathcal{Q}(T)} = \frac{\sum_v k_f^v \exp(-E_v/kT)}{K_{eq}\mathcal{Q}(T)} \tag{5.37}$$

Under nonequilibrium conditions, the ratio k_f/k_b is

$$\frac{k_f}{k_b} = \frac{\sum_v k_f^v \mathcal{R}(T, \alpha_1^v, \alpha_2^v, ...)}{\sum_v k_f^v \exp(-E_v/kT)} K_{eq}\mathcal{Q}(T) \tag{5.38}$$

Now for equilibrium conditions, we can easily verify that we this ratio k_f/k_b as K_{eq}.

$$\left[\frac{k_f}{k_b}\right]_{eq} = \frac{\sum_v k_f^v \mathcal{R}_{eq}(T, \alpha_1^v, \alpha_2^v, ...)}{\sum_v k_f^v \exp(-E_v/kT)} K_{eq}\mathcal{Q}(T) = \frac{\sum_v k_f^v \frac{\exp(-E_v/kT)}{\mathcal{Q}(T)}}{\sum_v k_f^v \exp(-E_v/kT)} K_{eq}\mathcal{Q}(T) = K_{eq} \tag{5.39}$$

Let us revisit the expression for k_b Eq. (5.37).

$$k_b = \frac{1}{K_{eq}} \sum_v k_f^v \frac{\exp(-E_v/kT)}{\mathcal{Q}(T)} = \frac{1}{K_{eq}} [k_f]_{eq} \tag{5.40}$$

This shows that under nonequilibrium conditions, the backward rate constant is unaffected by the vibrational distribution of the gas. The recombining atoms 'see' only the energy barrier and not beyond, i.e. the vibrational level they recombine to, does not affect the rate constant.

This exercise also gives a constraint on the forward rate constant distribution. The rate constant distribution at equilibrium must satisfy the following condition.

$$[k_f]_{eq} = k_f(T) = \sum_v k_f^v \frac{\exp(-E_v/kT)}{\mathcal{Q}(T)} \tag{5.41}$$

We need to obtain expressions for k_f^v that satisfy Eqn 5.41. There are potentially many solutions to the state-specific rate constant k_f^v given a global rate constant $[k_f]_{eq}$. Typically, k_f^v for upper vibrational states are larger due to increased tendency to dissociate. Once we obtain k_f^v, we can obtain a nonequilibrium rate constant from Eqn 5.34.

Following the generalized procedure described above, we can derive some of the popularly used chemistry - vibration coupling models by picking an appropriate k_f^v.

5.4.2 Special Cases

Trivial Solution

The trivial solution to the constraint equation is that k_f^v is dependent only on T.

$$k_f^v = C(T) \tag{5.42}$$

$$[k_f(T)]_{eq} = \sum_v k_f^v \frac{\exp(-E_v/kT)}{\mathcal{Q}(T)} = \sum_v C(T) \frac{\exp(-E_v/kT)}{\mathcal{Q}(T)} = C(T) = k_f(T) \tag{5.43}$$

There is no vibration-chemistry coupling in this case.

Cut-off Harmonic Oscillator - I

This case considers the molecules to behave as harmonic oscillators. The vibrational distribution is characterized by a vibrational temperature, T_v. This means that,

$$\frac{[\mathrm{O}_2^v]}{[\mathrm{O}_2]} = \mathcal{R}(T, \alpha_1^v, \alpha_2^v, ...) = \frac{\exp(-E_v/kT_v)}{\mathcal{Q}(T_v)} \tag{5.44}$$

So far we have not specified the number of vibrational levels. Let us suppose that the maximum vibrational level is N_{max}. Consider the following expression that scales the rate constant k_f^v, exponentially with vibrational level energy, E_v.

$$k_f^v = \frac{k_f(T) \exp(E_v/kT) \mathcal{Q}(T)}{N_{max}} \tag{5.45}$$

This expression satisfies the constraint.

$$\sum_v k_f^v \frac{\exp(-E_v/kT)}{\mathcal{Q}(T)} = \sum_v \frac{k_f(T) \exp(E_v/kT) \mathcal{Q}(T)}{N_{max}} \frac{\exp(-E_v/kT)}{\mathcal{Q}(T)} \tag{5.46}$$

Note that all the expressions inside the summation gets canceled with one another giving $k_f(\mathrm{T})/N_{max}$,

$$\sum_v \frac{k_f(T)}{N_{max}} = k_f(T) \tag{5.47}$$

Now let us evaluate the forward rate constant for this case. From Eq. (5.24).

$$k_f = \sum_v k_f^v \frac{[\mathrm{O}_2^v]}{[\mathrm{O}_2]} = \sum_v \frac{k_f(T) \exp(E_v/kT) \mathcal{Q}(T)}{N_{max}} \frac{[\mathrm{O}_2^v]}{[\mathrm{O}_2]} \tag{5.48}$$

$$k_f = \sum_v \frac{k_f(T)\exp(E_v/kT)\mathcal{Q}(T)}{N_{max}} \frac{\exp(-E_v/kT_v)}{\mathcal{Q}(T_v)} \tag{5.49}$$

Pulling out terms that are independent of 'v' from the summation,

$$k_f = \frac{k_f(T)\mathcal{Q}(T)}{N_{max}\mathcal{Q}(T_v)} \sum_v \exp\left(\frac{-E_v}{k}\left(\frac{1}{T_v} - \frac{1}{T}\right)\right) = k_f(T)\frac{\mathcal{Q}(T)\mathcal{Q}(T_m)}{N_{max}\mathcal{Q}(T_v)} \tag{5.50}$$

where $1/T_m = 1/T_v$ - $1/T$. This result is exactly the same as the one obtained by Marrone & Treanor in 1962 [53]. This model is known as the chemistry-vibration-dissociation or the CVD model.

Cut-off Harmonic Oscillator - II

Notice that in the above derivation, the parameter N_{max} appears because of summation in (5.47). It can be viewed as a normalizing factor. This implies that we could have any factor that is summable over the vibrational levels. Consider a similar expression for k_f^v as in (5.45),

$$k_f^v = k_f(T)\exp(E_v/kT)\mathcal{Q}(T)\frac{\exp(E_v/kU)}{\mathcal{Q}(-U)} \tag{5.51}$$

$$\sum_v \exp(E_v/kU) = \mathcal{Q}(-U) \qquad \text{just as} \qquad \sum_v 1 = N_{max} \tag{5.52}$$

Following the same procedure for this form of rate constant,

$$k_f = \frac{k_f(T)\mathcal{Q}(T)}{\mathcal{Q}(-U)\mathcal{Q}(T_v)} \sum_v \exp\left(\frac{-E_v}{k}\left(\frac{1}{T_v} - \frac{1}{T} - \frac{1}{U}\right)\right) = k_f(T)\frac{\mathcal{Q}(T)\mathcal{Q}(T_F)}{\mathcal{Q}(-U)\mathcal{Q}(T_v)} \tag{5.53}$$

where $1/T_F = 1/T_v$ - 1/T - 1/U. This result is the same as Marrone & Treanor in 1963 [54]. This model is popularly known as the chemistry-vibration-dissociation-vibration or the CVDV model. In the same paper, the authors show that the initial distribution of the recombination states as $\exp(E_v/kU)/\mathcal{Q}(-U)$.

From the above results and Ref. [54] we can assume that the general form of the state-specific rate expression is given by

$$k_f^v = k_f(T)\exp(E_v/kT)\mathcal{Q}(T)\mathcal{P}_b(v) \tag{5.54}$$

where $\mathcal{P}_b(v)$ is the probability that the molecule formed is at the vibrational state v. A closer examination at the above equation shows that this equation is the same as (5.33).

5.4.3 Reduced Model using Prior Distribution

In this section we derive a reduced model that uses the prior recombination distribution without the need for a state-specific approach. The focus of this reduced model is to reproduce the results obtained via the state-specific approach. We retain some of the key assumptions to simplify the formulation. The first of which is that we will continue to assume that a molecule at $E_{int}(v(J),J)$ will transition to the isoenergetic state, $E_{int}(v(0),0)$, and relax within that vibrational manifold towards equilibrium. As stated in earlier sections, this precludes the inclusion of rotational quantum number J in our calculations. The next assumption is that we will model the molecule as harmonic oscillators. The difference between modeling molecules as harmonic and anharmonic oscillators is very small when comparing the macroscopic variables such as density or temperature. Also, assuming molecules are harmonic oscillators simplifies the vibration-vibration coupling. It allows the use of a single vibrational temperature to describe the vibrational state of the gas. We do not have to consider the intramolecular vibrational relaxation processes due to equal energy spacing. The source term to the vibrational energy equation will include the terms from chemistry and the vibrational-translational processes. The source term due to vibrational - translational processes is obtained using the Landau-Teller model described in Chapter 2. We will derive the source term due to chemistry in the later part of this section.

Let us first obtain the expression for the rate constant under nonequilibrium conditions. We start with Eq. (5.54),

$$k_f^v = k_f(T)\exp(E_v/kT)\mathcal{Q}(T)\mathcal{P}_b(v) \tag{5.55}$$

From the prior recombination distribution model, for recombination processes we already know the probability $\mathcal{P}_b(v)$. Now the effective rate constant is given by,

$$k_f = \sum_v k_f^v \frac{[\mathrm{O}_2^v]}{[\mathrm{O}_2]} = \sum_v k_f(T)\exp(E_v/kT)\mathcal{Q}(T)\mathcal{P}_b(v)\frac{[\mathrm{O}_2^v]}{[\mathrm{O}_2]} \tag{5.56}$$

For a harmonic oscillator, we can describe the molecule by means of a single vibrational temperature.

$$k_f = \sum_v k_f(T)\frac{\exp(E_v/kT)\mathcal{Q}(T)}{\exp(E_v/kT_v)\mathcal{Q}(T_v)}\mathcal{P}_b(v) \tag{5.57}$$

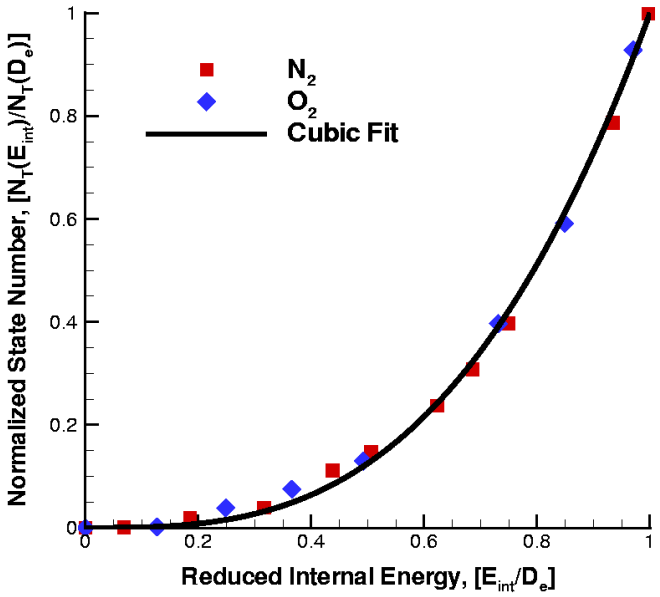

Figure 5.6: Number of states as a function of reduced internal energy

The next step is to obtain an analytic expression for the probability, $\mathcal{P}_b(v)$. We use the result for the number state population obtained by Kelley [48]. This is shown in Fig. 5.6.

The number of available states for a diatomic molecule scales cubically with the reduced internal energy. In analytic terms,

$$\frac{N_T(E_{int})}{N_T(D_e)} = \left(\frac{E_{int}}{D_e}\right)^3 \tag{5.58}$$

Taking discrete derivative,

$$\Delta N_T(E_{int}) = \frac{3[N_T(D_e)][E_{int}]^2}{{D_e}^3}\Delta E_{int} \tag{5.59}$$

This $\Delta N_T(E_{int})$ is the number of states present in the interval $E_{int} \pm \Delta E_{int}/2$, and ΔE_{int} may be considered to be the bin size. The density distribution of molecular states is given by [52],

$$\rho(E_{int}; E_{total}) \propto [\Delta N_T(E_{int})] \times [E_{total} - E_{int}]^{\frac{1}{2}} \tag{5.60}$$

Using the results above, the probability distribution is given by

$$\mathcal{P}_b(E_{int};E_{total}) = \frac{\rho(E_{int};E_{total})}{\sum \rho(E_{int};E_{total})} = \frac{E_{int}^2[E_{total}-E_{int}]^{\frac{1}{2}}}{\sum_v E_{int}^2[E_{total}-E_{int}]^{\frac{1}{2}}} \tag{5.61}$$

Under the assumptions made earlier in this section, $E_{int} \equiv E_v$,

$$\mathcal{P}_b(v;E_{total}) = \frac{E_v^2[E_{total}-E_v]^{\frac{1}{2}}}{\sum_v E_v^2[E_{total}-E_v]^{\frac{1}{2}}} \tag{5.62}$$

Substituting the above result in the rate constant expression,

$$k_f = \sum_v k_f(T)\frac{\exp(E_v/kT)\mathcal{Q}(T)}{\exp(E_v/kT_v)\mathcal{Q}(T_v)}\frac{E_v^2[E_{total}-E_v]^{\frac{1}{2}}}{\sum_v E_v^2[E_{total}-E_v]^{\frac{1}{2}}} \tag{5.63}$$

On further simplification,

$$k_f(T,T_v) = \frac{k_f(T)}{\sum_v E_v^2[E_{total}-E_v]^{\frac{1}{2}}}\frac{\mathcal{Q}(T)}{\mathcal{Q}(T_v)}\sum_v \exp\left(\frac{E_v}{k}\left(\frac{1}{T}-\frac{1}{T_v}\right)\right)E_v^2[E_{total}-E_v]^{\frac{1}{2}} \tag{5.64}$$

Note that when $T = T_v$, we get back the expression for $k_f(T)$. Now let us evaluate the $P_f(v)$ from the above expression. It is useful to denote the summation in the above equation by $\mathcal{N}_\mathcal{D}$

$$\mathcal{N}_\mathcal{D} = \frac{\sum_v \exp\left(\frac{E_v}{k}\left(\frac{1}{T}-\frac{1}{T_v}\right)\right)E_v^2[E_{total}-E_v]^{\frac{1}{2}}}{\sum_v E_v^2[E_{total}-E_v]^{\frac{1}{2}}} \tag{5.65}$$

Now, the expression for $k_f(T,T_v)$ is

$$k_f(T,T_v) = k_f(T)\frac{\mathcal{Q}(T)}{\mathcal{Q}(T_v)}\mathcal{N}_\mathcal{D} \tag{5.66}$$

We can now obtain an expression for the probability that dissociation has occurred from level v from Eq. (5.26),

$$\mathcal{P}_f(v) = \frac{k_f(T)\exp(E_v/kT)\mathcal{Q}(T)\mathcal{P}_b(v)}{k_f(T)\frac{\mathcal{Q}(T)}{\mathcal{Q}(T_v)}\mathcal{N}_\mathcal{D}}\frac{\exp(-E_v/kT_v)}{\mathcal{Q}(T_v)} \tag{5.67}$$

This can be further simplified to give,

$$\mathcal{P}_f(v) = \frac{\exp\left(\frac{E_v}{k}(\frac{1}{T}-\frac{1}{T_v})\right)}{\mathcal{N}_\mathcal{D}}\mathcal{P}_b(v) \tag{5.68}$$

Also, its important to note that the recombination rate constant, k_b is not altered by the vibrational distribution of the molecule (Eq. (5.40)).

Vibrational Source Term due to Chemical Reactions

As with any chemistry-vibrational model, we need to address the amount of energy released into the vibrational modes when chemical reactions take place. Following Marrone and Treanor [54], the average energy gained by recombination is given by

$$\overline{E}_R = \sum_v E_v \mathcal{P}_b(v) \tag{5.69}$$

where $\mathcal{P}_b(v)$ is given by Eq. (5.62). Similarly, the energy lost during dissociation,

$$\overline{E}_D = \sum_v E_v \mathcal{P}_f(v) \tag{5.70}$$

where $\mathcal{P}_f(v)$ is given by Eq. (5.67). The vibrational source due to chemistry is then given by,

$$Q_{chem_s} = \overline{E}_R w_{r_s} + \overline{E}_D w_{d_s} \tag{5.71}$$

Also, if $\overline{E}_D$ is expressed as $\overline{E}(T, T_v)$, its easy to verify that $\overline{E}_R$ is $\overline{E}(T, T)$ [10].

To summarize, we have developed a chemistry-vibrational model by using the concepts of the prior distribution model. The rates take into account the nonequilibrium state of the gas. The chemistry source term due to vibration has been re-derived for the prior distribution case. We retain the Landau-Teller formulation for the vibrational energy produced due to vibrational-translational relaxation processes.

5.4.4 Results: Reduced Model

We first look at the probability distribution $\mathcal{P}_f(v)$ and $\mathcal{P}_b(v)$, and compare them with the Boltzmann distribution for different vibrational temperatures. The standard model assumes that when a new molecule is formed, it is formed at the local vibrational temperature. This implies that the energy in the vibrational modes of that molecule correspond to a Boltzmann distribution at the local vibrational temperature. Similarly, when a molecule dissociates, the vibrational energy removed is calculated based on the vibrational temperature of the mixture. Thus the standard model's probability distribution, $\mathcal{P}_f^{std}(v)$ and $\mathcal{P}_b^{std}(v)$ are both equal, and is given by the Boltzmann distribution at the vibrational temperature, T_v.

The probability distribution of the reduced model, $\mathcal{P}_f(v)$ and $\mathcal{P}_b(v)$ are compared with the Boltzmann distribution. The comparison for the case, T=T_v is shown in

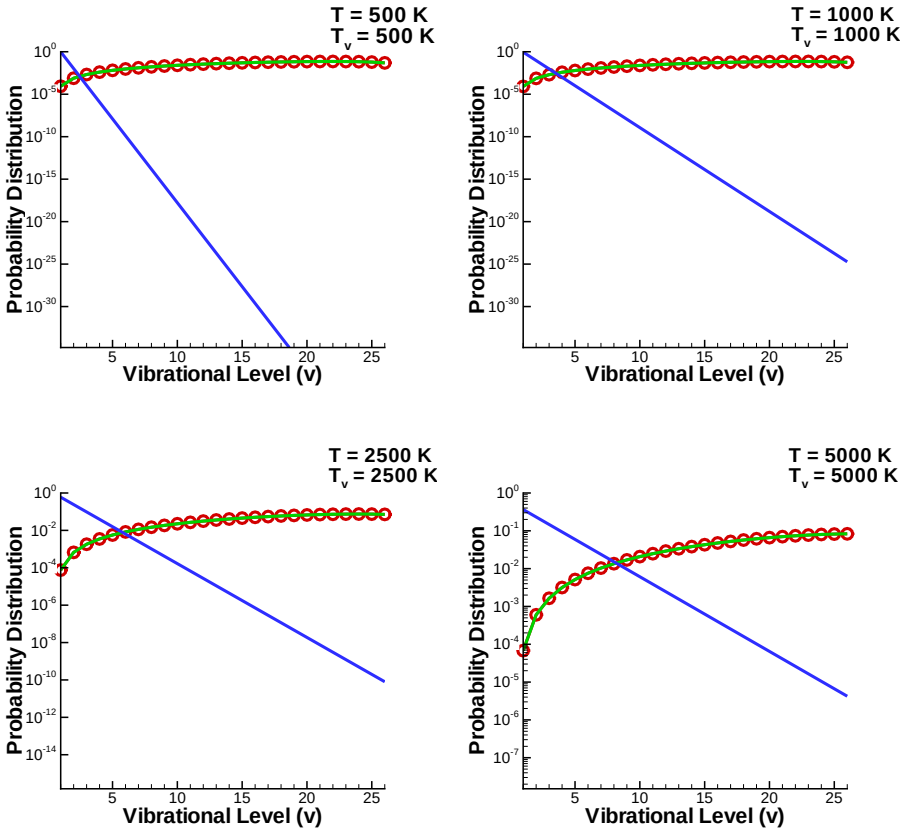

Figure 5.7: Probability Distribution of Recombination States for $T = T_v$. Blue line: Boltzmann distribution at T_v. Green line: $\mathcal{P}_f(v)$. Red circle: $\mathcal{P}_b(v)$

Fig. 5.7. As expected, the probability distribution for the forward and backward reaction are the same. Note that this probability distribution is not the same as the Boltzmann distribution. The rotational degeneracy in the reduced model formulation allows upper internal/vibrational states to be selectively populated even at equilibrium. These probability distributions are initial distributions right after recombination. Any initial distribution always relaxes towards a Boltzmann distribution (harmonic oscillator assumption). This implies that if a flow is accelerating from an equilibrium state, like the nozzle expansion, upper vibrational states will be preferentially populated, and close to the throat, there will be an onset of vibrational nonequilibrium in the flow as it expands due to time scale disparity between vibrational relaxation and flow time scales.

The next figure (Fig. 5.8) shows the probability distribution for cases where $T > T_v$. This type of case is typically encountered behind a shock, where the vibrational temperature lags the translational temperature. The chemistry behind a shock is dominated by dissociation reactions. The standard models like Park's model or Marrone & Treanor model were developed and validated for dissociating flow behind shocks. We see that the probability distribution of the reduced model, $\mathcal{P}_f(v)$ is very similar to a Boltzmann distribution that most standard models use. It is important to note that $\mathcal{P}_f(v)$ looks like a Boltzmann distribution corresponding to a larger temperature than the temperature that standard models assume i.e. T_v for Park's model. The mismatch of the $\mathcal{P}_b(v)$ is not very important for these type of flows since the backward rates of recombination are usually very low behind a shock, thus the vibrational energy source term is unaffected by recombination.

Figure 5.9 shows the probability distribution for cases where $T < T_v$. These conditions occur during a nozzle expansion. In these set of plots, $\mathcal{P}_b(v)$ is the probability distribution in focus since the expanding flow is dominated by recombination reactions due to rapid decrease in translational temperature. Note that unlike the previous case, there is considerable difference between the Boltzmann distribution at T_v and $\mathcal{P}_b(v)$ especially at low translational temperatures.

It is also instructive to investigate the rate constants between the standard Park's model and the reduced model. The backward rate constant or the recombination rate constant is unaltered between the models. The comparison between the forward rate constants of dissociation is presented in Fig. 5.10. The factor $\mathrm{k}_f(T,T_v)/\mathrm{k}_f(T)$ is compared between the two models for different temperatures. This factor is dependent on the parameters of the rate constant for Park's model. For the reduced model, this factor is independent of the rate constant. The factor predicted by the reduced model formulation is uniformly greater or equal to the factor predicted by Park's model. The difference between T and T_v significantly influences the difference between the factors. Note that although the factor may be very large, the actual value of the dissociation rates in expansion flows are very small.

Figure 5.11 shows the variation of E_R, E_D and e_{vib} (estimated at T_v) for different temperatures. As expected, E_R remains constant in each of the plots as it is solely dependent on the translational temperature. For the case $T = 500$ K, E_D rapidly

changes from $T_v = 500$ K to 1000 K, and very slowly increases for temperatures greater than 1000 K. Notice the order of magnitude difference between the energy predicted by standard model and the reduced model. Assuming the recombination rates are about the same, the vibrational source term due to chemistry is much larger than the standard model estimate. This is because of the preferential population of the upper vibrational states modeled by the reduced model.

In summary, these results show that the reduced model reflects the most important aspects of the state-specific prior distribution model. However, there is certain loss in detail by assuming a single vibrational temperature for the vibrational distribution of the molecule. In the state-specific model, if a molecule in upper vibrational state is formed then it has two choices, either to re-dissociate or to relax to lower vibrational states. In the reduced model, a molecule formed at an upper vibrational state (v_{high}) would imply a larger value of the vibrational energy source term. This increase in vibrational energy source term manifests itself as increased vibrational temperature of the molecule. This in turn implies that the molecular states conform to a Boltzmann distribution for that vibrational temperature. So the effect of a single recombination to an upper vibrational state (v_{high}) is spread over all molecular states in the reduced model. As a result of such a distribution, the number density of the vibrational state v_{high} is lower than what it is supposed to be. This reduces the rate of that vibrational state re-dissociating due to lower concentration. This effect is not present in the state-specific model.

The reduced model was implemented in the standard nozzle code [19]. We retain the Landau-Teller model for vibration-translation relaxation. The relaxation times for O_2-O_2 and O_2-O are obtained from best curve fits (Table 3.3). Using these relaxation times will predict the same V-T behavior as the state-specific prior distribution model.

Two cases were picked from the matrix to compare the new model with both the state-specific model and the standard model. The test section results are tabulated in Table 5.9. The test section is located at 6.26 m from the throat. Runs 82 and 91 were selected as test cases. The state-specific model predicted both chemical and vibrational nonequilibrium at the test section for Run 82. For Run 91, the state-specific model predicted vibrational nonequilibrium even though the standard model predicted equilibrium conditions.

The reduced model reproduces the vibrational nonequilibrium predicted by the state-specific model. However the vibrational temperature predicted by the reduced model is slightly larger than the state-specific estimate. Also, the extent of chemical nonequilibrium predicted by state-specific model (eg. Run 82) is not reproduced by the reduced model. The reason for the mismatches has been covered briefly earlier in this section. Figures 5.12 and 5.13 illustrate the reason for the difference. These figures show the mass fraction of various vibrational states from the state-specific recombination model. For both runs, we see that the mass fraction for the lower vibrational states (eg. v = 1, 2 and 5) shows an increase near the throat due to recombination and then decrease due to vibration-vibration relaxation processes. The mass fraction of upper vibrational states (v = 10, 15, 20 & 30) continues to decrease as the flow expands. This is because the upper vibrational states that are formed by oxygen atom recombination have larger rates of re-dissociation than the lower vibrational states. This causes lower concentration of O_2 in the test section for the state-specific model. This effect is stronger in Run 82.

It is also instructive to look at the vibrational temperature variation given by the reduced model. This is shown in Fig. 5.14. For Run 82, we see an initial decline in vibrational temperature primarily due to Landau-Teller vibrational-translation relaxation. The vibrational temperature starts to increase due to recombination of O_2 molecules. As upper vibrational states are preferred, the vibrational energy available to the mixture due to recombination is large. This manifests as larger vibrational temperature. For Run 91, similar variation in vibrational temperature is observed in the near-throat region, although it is less than 1% of the test section vibrational temperature. The use of single vibrational temperature reduces the actual concentration of molecules in the upper vibrational states and thereby prevents re-dissociation. Re-dissociation would reduce the concentration of O_2 and also reduce the vibrational temperature (due to the vibrational energy loss during dissociation).

Additionally, the expansion process is dominated by recombination reactions, and since the recombination rate constant is the same for the standard and the reduced model, the test section chemical composition is very similar between the two models.

Table 5.9: Comparison of Flow variables at the Test Section.

Model	Density (kg/m^3)	Temp.(K)	Vib. Temp.(K)	Mass frac. O_2
Run 82				
Standard Model	1.045×10^{-3}	391.1	660.3	45.45%
Recombination Model	1.167×10^{-3}	247.2	2031.5	42.72%
Reduced Model	1.008×10^{-3}	312.7	2380.6	45.40%
Run 91				
Standard Model	1.543×10^{-3}	728.9	773.1	93.88%
Recombination Model	1.568×10^{-3}	568.9	1784.2	93.12%
Reduced Model	1.560×10^{-3}	578.0	1942.0	93.80%

5.5 Conclusions

A state-specific chemistry-vibrational model has been proposed and implemented to study the recombining flow in high enthalpy nozzles. Two types of models were considered. The first model assumed that atoms recombined to a specific vibrational level. This was carried out for harmonic and anharmonic oscillators. Both cases gave similar results for macroscopic flow variables such as density, temperature and mass fraction. When all vibrational states were considered for recombination with equal probability, the results were very close to that of a standard chemistry-vibrational coupling model. The second approach assumes that atoms recombine based on a probability distribution function. This implementation considers a model that provides a prior recombination distribution for the recombining states based on the total energy available to the system. The prior recombination distribution is obtained by counting the number of possible states in which a molecule can be formed. Both rotational and vibrational states are accounted for in counting the number of possible states. Due to degeneracy of the rotational states, we observe a biased distribution towards the higher internal energies at higher total energies. This model was implemented in an axisymmetric flow solver to study the expansion flow in a nozzle. The results at the test section show that the translational temperature is lower than the value predicted by the standard model. The present model also predicts larger values of the vibrational temperature and the mass fraction of O atoms.

To adequately reproduce the state-specific model using as few parameters as possible,

a reduced model was developed from basic principles. The prior distribution concepts were utilized in the development of the model. This model was implemented in the standard code to run the nozzle simulations. While the extent of vibrational nonequilibrium predicted by the state-specific model was very well captured by this reduced model, the extent of chemical nonequilibrium was not as large as the state-specific model.

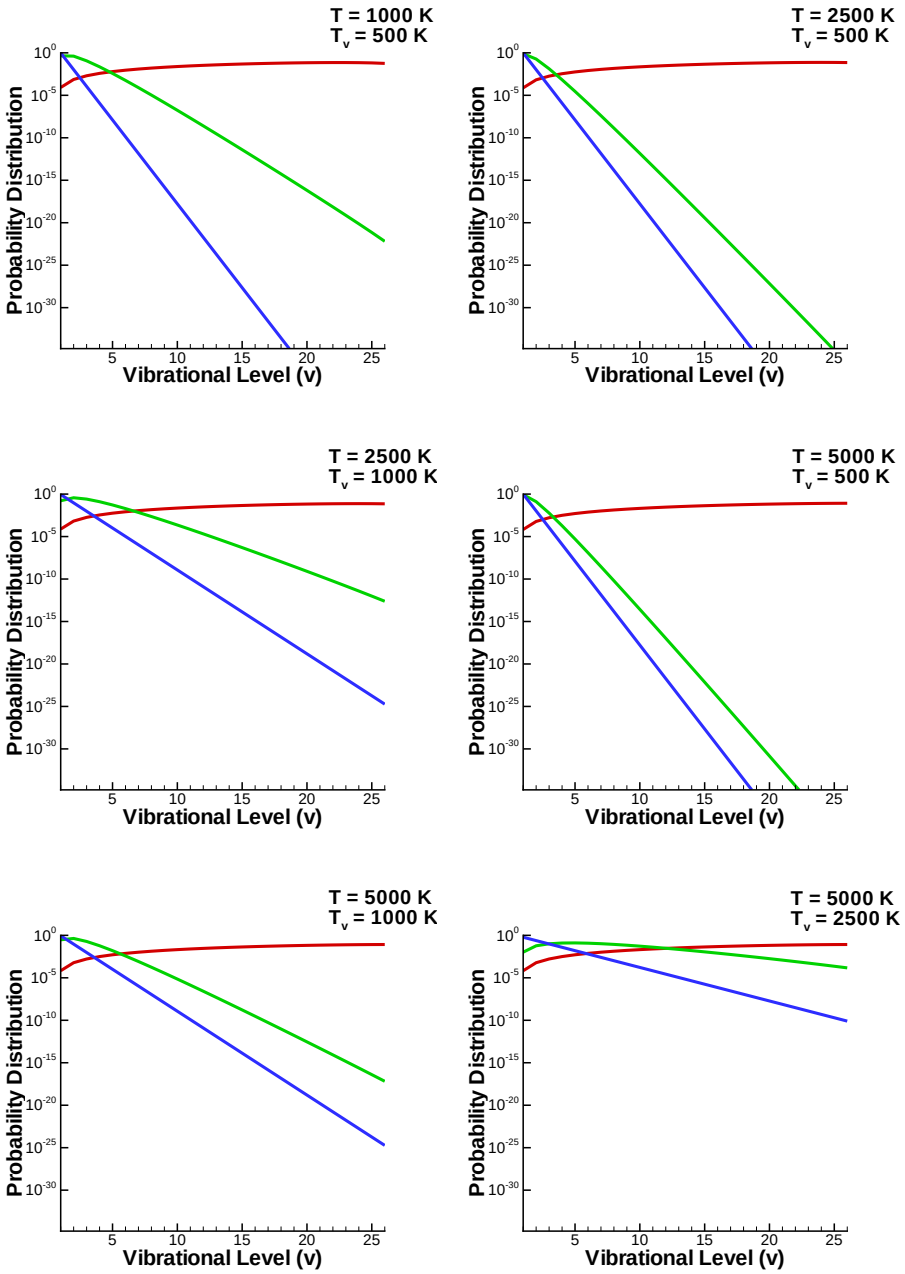

Figure 5.8: Probability Distribution of Recombination States for $T > T_v$. Blue line: Boltzmann distribution at T_v. Green line: $\mathcal{P}_f(v)$. Red line: $\mathcal{P}_b(v)$

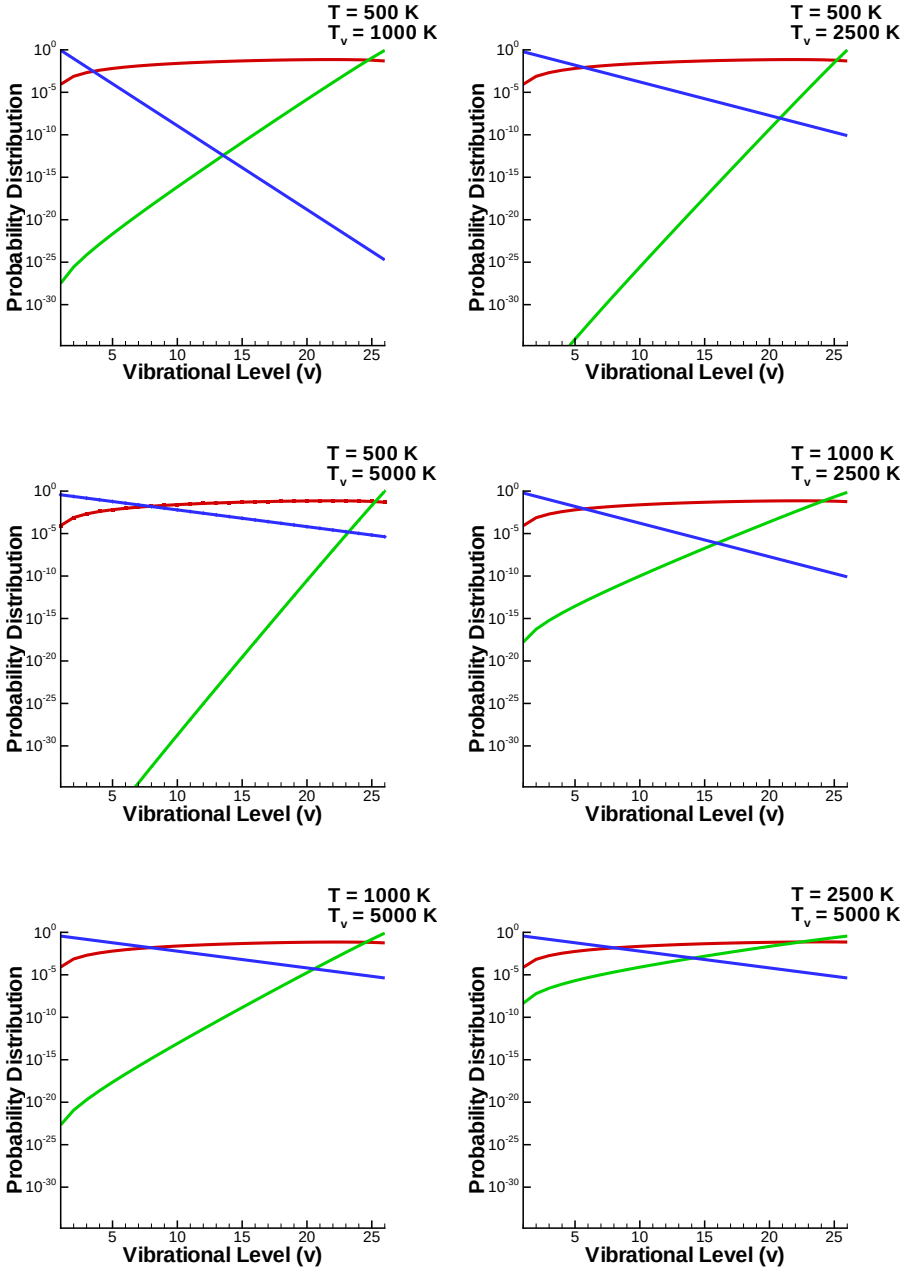

Figure 5.9: Probability Distribution of Recombination States for $T < T_v$. Blue line: Boltzmann distribution at T_v. Green line: $\mathcal{P}_f(v)$. Red line: $\mathcal{P}_b(v)$

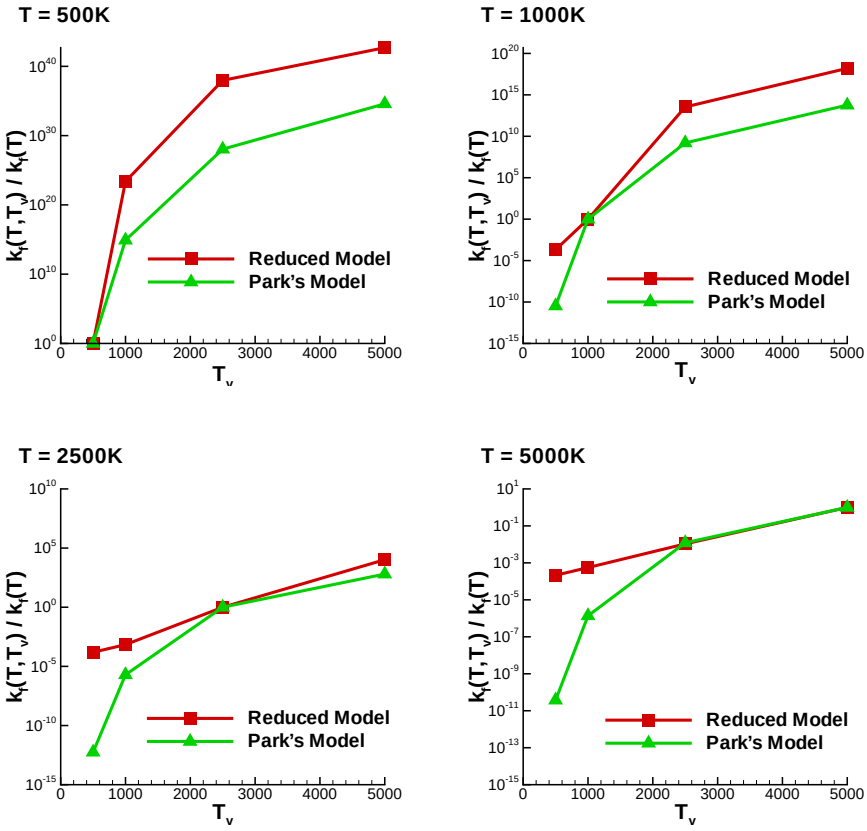

Figure 5.10: Variation of the factor $k_f(T,T_v)/k_f(T)$ with T_v for different T.

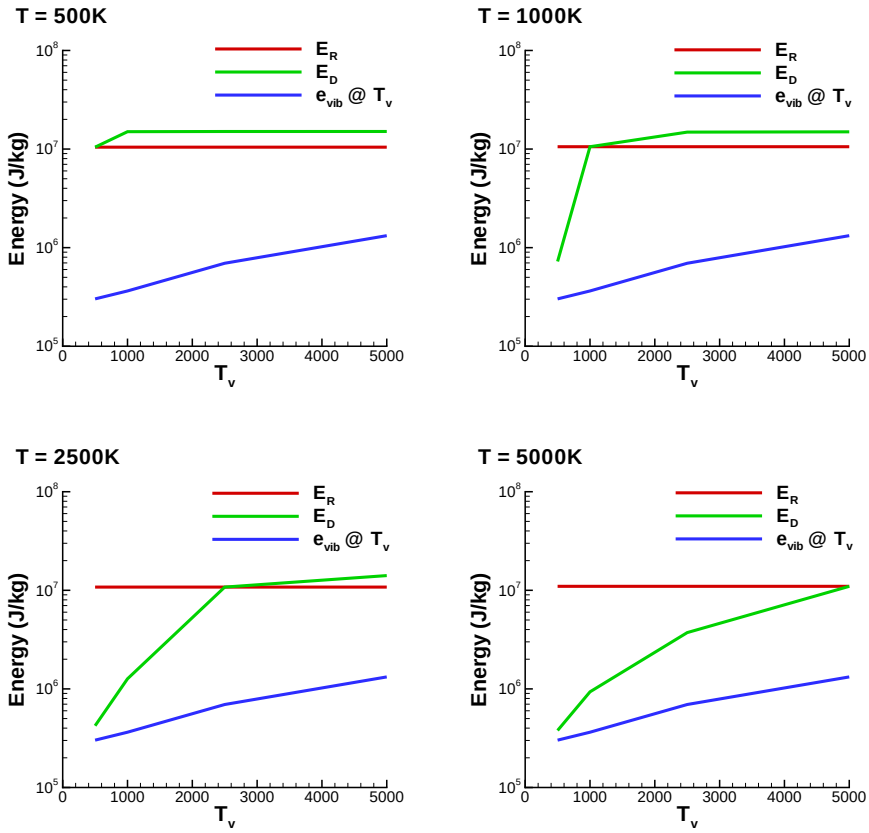

Figure 5.11: Variation of energy E_R, E_D and $\mathrm{e}_{vib}(T_v)$ with T_v for different T.

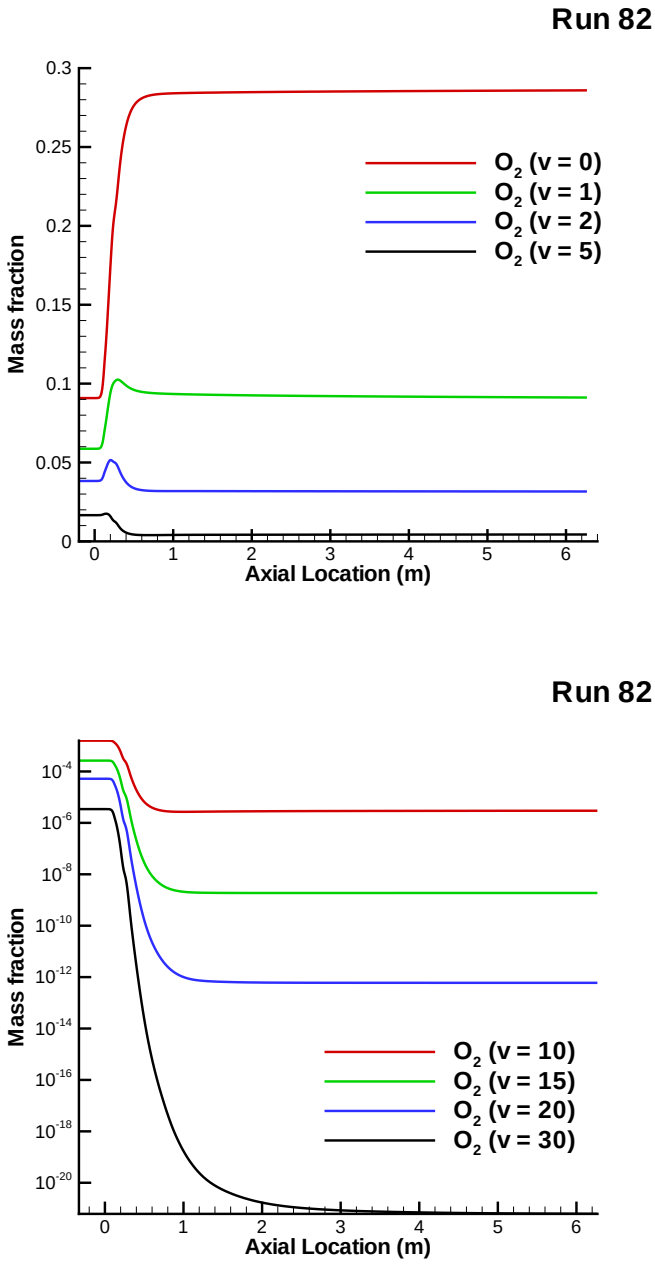

Figure 5.12: Variation of mass fraction of various vibrational states of O_2 with axial location (Run 82)

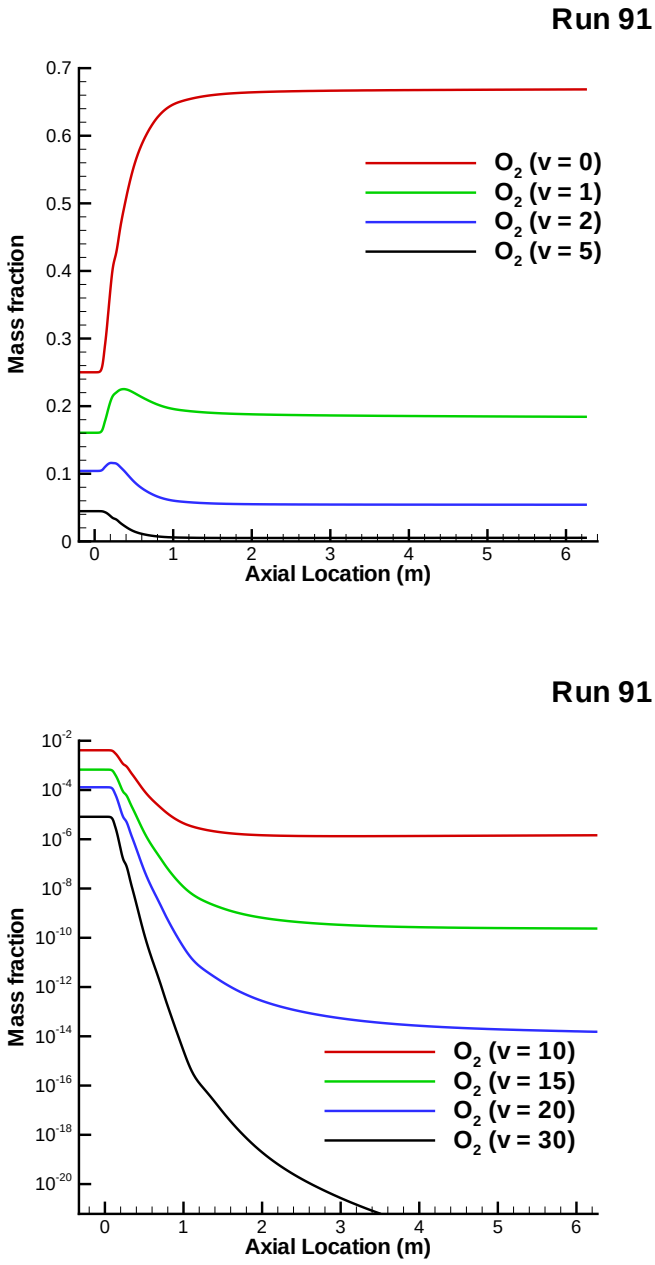

Figure 5.13: Variation of mass fraction of various vibrational states of O_2 with axial location (Run 91)

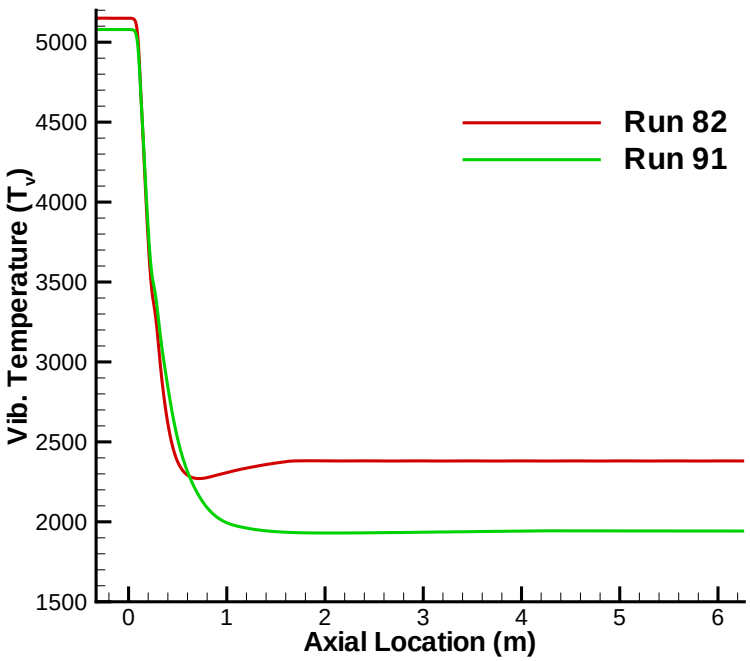

Figure 5.14: Variation of vibrational temperature with axial location.

Chapter 6

Conclusion and Discussion

6.1 Summary

This thesis investigates possible reasons for the discrepancies observed between simulations and experiments in high enthalpy wind tunnel facilities. The differences observed are peculiar to high enthalpy reflected shock tunnels where high temperature effects are most prominent. The primary motivation for the present work is the observed increased shock standoff distance observed in high enthalpy carbon dioxide flow over the Mars Science Laboratory capsule. Also, in recent oxygen runs in the same facility, the surface pressure and heat transfer data predicted by computations did not match with the experiments.

First, the governing equations for a chemically reacting, vibrationally relaxing flowfield were presented. Physical models and relevant rate constants were also presented. The assumptions and the limitations of the chemistry-vibration coupling model employed in standard codes were explained. Also, the numerical method, and the codes that were used to simulate the flowfield were discussed in brief.

In the first part of the work, an elaborate procedure to model the vibrational relaxation of the CO_2 system was carried out. A state-specific approach was used, where every vibrational state of different molecules in the CO_2 system was taken to be a separate chemical species. All important reactions were identified. The anharmonic behavior of the molecules was implicitly accounted for in the energy of the species. Harmonic oscillator scaling and SSH scaling were used to obtain the rate constants for

transitions/reactions wherever experimental data were unavailable. Validation studies were carried out for this vibrational model. Very good agreement was observed between experimental and computational relaxation times. Next, this vibrational model was coupled with the chemical reactions in two ways: a reduced model with 4 species (CV-pτ) and an elaborate model that includes all the 16 state-specific species (CV-16). These models were implemented in the standard codes to carry out nozzle simulations to obtain the test section conditions. The test section conditions were used as inflow for the shock standoff studies. The shock standoff distance did not appreciably change between the standard model and the CV-pτ model. With the CV-16 model, the shock standoff distance decreased, showing that the chemistry-vibration coupling plays an important role. This study showed that elaborate vibrational modeling did not explain the increased shock standoff distance.

In the second part of the study, the effect of excited electronic states was briefly investigated. A recent computational study that uses quasi-classical trajectory calculations showed that the first excited electronic state of CO_2 plays a very important role in the recombination process. Previous CFD studies had suggested, within the constraints imposed by their modeling, that excited electronic states of O_2 did not have an impact on the chemistry. Since similar constraints were present in the models used in this work, excited electronic states of O_2 were not included. A simple model was devised to incorporate all of the essential components of the recombination mechanism. The net effect on the shock standoff was to increase it by almost 100%. This showed that the excited electronic states play an important role at high enthalpy high temperature flows.

In the last part of the study, we investigated the coupling between chemistry and vibration of diatomics. Firstly, a numerical experiment was devised to investigate the effect of forced recombination to a pre-defined vibrational state. The molecules were treated as either harmonic or anharmonic oscillators. Although the macroscopic variables such as density, temperature and mass fraction did not appreciably change between harmonic and anharmonic oscillator assumptions, they were significantly different from the standard model calculations. Next, all vibrational levels of the molecules were taken to be equally probable for the recombination process. The predicted nozzle test section conditions for this equal probability recombination were very close to the standard

model predictions. This motivated further research to establish the initial distribution of molecules over vibrational states upon recombination. Information theory was used to estimate the prior distribution of recombination states. Both rotational and vibrational states, and their inherent coupling were taken into account while estimating this prior distribution. The resulting distribution showed that upper internal states were selectively populated during the recombination process. This model was implemented in the standard code using the state-specific approach to carry out the nozzle simulations. The test section results showed a large degree of vibrational nonequilibrium compared to the standard model. In some cases, mass fraction of O atoms were slightly increased. In order to make this approach feasible for realistic cases, a reduced model was developed to incorporate the essentials of the state-specific model. Although, the extent of chemical nonequilibrium predicted by the reduced model was not as large as the state-specific model, the vibrational nonequilibrium in the test section was very well captured by the reduced model.

6.2 Concluding Remarks

This study shows that the puzzle of increased shock standoff distance observed in carbon dioxide flows at high enthalpy conditions is extremely complex, and has multiple factors that contribute. Carbon dioxide, a triatomic molecule has three modes of vibration. These modes interact both with each other and with other molecules in the mixture. Additionally, these modes can also interact with other chemical species such as oxygen or carbon monoxide. This work provides best fit approximations for the relaxation times associated with the vibrational interactions for multiple pairs.

The inclusion of excited electronic states in high enthalpy flows is very crucial to predicting the right test section conditions. The number density of the first excited state of CO_2 in the nozzle, though very low, influences the shock standoff distance significantly. Better estimates for the rate constant for the transition reaction from the excited electronic state to the ground state would prove useful to better quantify the role of the first excited electronic state on the shock standoff.

This work also presents in depth analysis of the basic chemistry-vibrational coupling present in a vibrationally relaxing, chemically reacting system. The experiments with

oxygen as the test gas provide a very good data set to compare the macroscopic variables such as density, temperature etc. between different models. A reduced model with minimum empiricism is presented to reflect the actual mechanism of chemistry-vibrational coupling in dissociating/recombining systems.

6.3 Future Work

The problem of the increased shock standoff distance in high temperature CO_2 flow is not completely solved. The new chemistry-vibrational coupling model developed is applicable to dissociation/recombination reactions only. The effect of vibration-vibration coupling within a molecule is ignored by invoking the harmonic oscillator assumption. The molecules behave as anharmonic oscillators, especially at the enthalpies of interest, and this effect must be taken into account. The vibration-vibration coupling in anharmonic oscillators contribute to the vibrational energy source term and must be modeled accurately. The excited electronic states of O_2 should then be included in the model, and their role in recombining flows must be assessed. Comparison with the recent experiments at the LENS-I facility should provide valuable insight into the validity of such a model. New techniques to measure trace species such as excited states of O_2 or O atoms will be extremely useful to better understand the recombination process.

Further, this chemistry-vibrational coupling model must be extended to exchange reactions as well. The initial distribution of the newly formed molecules due to exchange reactions must be estimated by information theory or otherwise. This initial distribution could then be used to estimate the modified rate constants of the reaction. The modeling of vibration-vibration coupling is essential to accurately estimate these modified rate constants. The chemistry-vibration coupling model would then be adequate to analyze realistic flows with multiple species.

For CO_2, quantum calculations should be carried out to estimate the rate constant associated with the transition from the first excited electronic state to the ground state. This process is assumed to be very fast compared to the subsequent vibrational relaxation. The validity of this assumption must be ascertained. Also, at the upper internal energy levels, the various vibrational modes of CO_2 lose their individuality and relax as one. Such a behavior should also be adequately modeled.

Finally, computational chemistry work must be carried out to estimate rate constants in a vibrationally relaxing, chemically reacting system for various processes.

References

[1] MacLean, M. and Holden, M., "Numerical Assesment of Data in Catalytic and Transitional Flows for Martian Entry," AIAA Paper 2006–2946, June 2006.

[2] Holden, M., Wadhams, T., MacLean, M., Mundy, E., and Parker, R., "Experimental Studies in LENS I and X to Evaluate Real Gas Effects on Hypervelocity Vehicle Performance," AIAA Paper 2007–204, Jan. 2007.

[3] Sharma, M., Swantek, A., Flaherty, W., Austin, J., Doraiswamy, S., and Candler, G., "Experimental and Computational Investigation of Hypervelocity Carbon dioxide Flow over Blunt Bodies," *Journal of Thermophysics and Heat Transfer*, Vol. 24, No. 4, 2010.

[4] Parker, R., Wakeman, T., Holden, M., and MacLean, M., "Measuring Nitric Oxide Freestream Concentration Using Quantum Cascade Lasers at CUBRC," AIAA Paper 2006-0926, Jan. 2006.

[5] Parker, R. and Wakeman, T., "Measuring Nitric Oxide Freestream Velocity Using Quantum Cascade Lasers at CUBRC," AIAA Paper 2007-1329, Jan. 2007.

[6] Nompelis, I., Candler, G. V., MacLean, M., and Holden, M., "Investigation of Hypersonic Double-Cone Flow Experiments at High Enthalpy in the LENS facility," AIAA Paper 2007-0203, Jan. 2007.

[7] Nompelis, I., Candler, G., MacLean, M., Wadhams, T., and Holden, M., "Numerical Investigation of Double-Cone Flow Experiments with High-Enthalpy Effects," AIAA Paper 2010–1283, Jan. 2010.

[8] Hwang, D.-Y. and Mebel, A. M., "Ab initio study of spin-forbidden unimolecular decomposition of carbon dioxide," *Chemical Physics*, Vol. 256, 2000, pp. 169–176.

[9] Park, C., *Nonequilibrium Hypersonic Aerothermodynamics*, John Wiley & Sons, 1990.

[10] Olejniczak, J., *Computational and Experimental Study of Nonequilibrium Chemistry in Hypersonic Flows*, Ph.D. thesis, University of Minnesota, Minneapolis, April 1997.

[11] Vincenti, W. G. and Kruger, C. H., *Introduction to Physical Gas Dynamics*, Krieger Publishing Company, Florida, 1965, p. 203.

[12] Boyd, I. D., Chen, G., and Candler, G. V., "Predicting the Failure of Continuum in Transitional Hypersonic Flows," *Physics of Fluids*, Vol. 7, 2006, pp. 210–219.

[13] Wilke, C. R., "A Viscosity Equation for Gas Mixtures," *Journal of Chemical Physics*, Vol. 18, 1971, pp. 517–519.

[14] Blottner, F. R., Johnson, M., and Ellis, M., "Chemically Reacting Viscous Flow Program for Multi-Component Gas Mixtures," Sandia National Laboratories Report - SC-RR-70754,, 1971.

[15] Park, C., "Assessment of Two-Temperature Kinetic Model for Dissociating and Weakly-Ionizing Nitrogen." *Journal of Thermophysics and Heat Transfer*, Vol. 2, No. 1, 1988, pp. 8–16.

[16] McBride, B. J., Zehe, M. J., and Gordon, S., "NASA Glenn Coefficients for Calculating Thermodynamic Properties of Individual Species," NASA/TP-2002-211556, 2002.

[17] Lee, J. H., "Basic Governing Equation for Flight Regimes of Aeroassisted Orbital Transfer of Vehicles," *Thermal Design of Aeroassisted Orbital Transfer Vehicles*, edited by H. F. Nelson, Vol. 96, AIAA, New York, 1985, pp. 3–53.

[18] Millikan, R. C. and White, D. R., "Systematics of Vibrational Relaxation," *Journal of Chemical Physics*, Vol. 39, No. 12, 1963, pp. 3209–3213.

[19] Candler, G. V., "Hypersonic Nozzle Analysis Using an Excluded Volume Equation of State," AIAA Paper 2005–5202, June 2005.

[20] I. Nompelis, T. W. D. and Candler, G. V., "Development of Hybrid Unstructured Implicit solver for the Simulation of Reacting Flows Over Complex Geometries," AIAA Paper 2004–227, July 2004.

[21] Nompelis, I., Drayna, T. W., and Candler, G. V., "A Parallel Unstructured Implicit Solver for Hypersonic Reacting Flow Simulations," AIAA Paper 2005–4867, June 2005.

[22] Wright, M. J., Candler, G. V., and Bose, D., "Data-Parallel Line Relaxation Method for the Navier Stokes Equations Using Gauss-Seidel Line Relaxation," *AIAA Journal*, Vol. 36, No. 9, 1998, pp. 1603–1609.

[23] Taylor, R. L. and Bitterman, S., "Survey of Vibrational Relaxation Data for Process Important in the CO_2-N_2 Laser System," *Reviews of Modern Physics*, Vol. 41, No. 1, 1969, pp. 26–47.

[24] Lewis, P. F. and Trainor, D. W., "Survey of Vibrational Relaxation Data for O_2, N_2, NO, H_2, CO, HF, HCl, CO_2, and H_2O," AMP–422, AVCO Everett Research Laboratory, Nov. 1974.

[25] Weitz, E. and Flynn, G. W., "Laser Studies of Vibrational and Rotational Relaxation in Small Molecules," *Annual Review of Physical Chemistry*, Vol. 25, 1974, pp. 275–315.

[26] Ono, S. and Teii, S., "Vibrational Temperature in a Weakly Ionised CO_2-N_2-He discharge," *J. Phys. D:Appl. Phys*, Vol. 18, No. 3, 1985, pp. 441–450.

[27] Ralph R. Jacobs, K. J. P. and Thomas, S. J., "Rate constants for the CO_2 02^02-10^00 relaxation," *Physical Review A*, Vol. 11, No. 1, 1975, pp. 54–61.

[28] Orr, B. J. and Smith, I. W. M., "Collision-Induced Vibrational Energy Transfer in Small Polyatomic Molecules," *Journal of Chemical Physics*, Vol. 91, 1987, pp. 6106–6119.

[29] S. L. Lunt, C. T. W. J. and Simpson, C. J. S. M., "Rate Constants for the Deactivation of the 15 μm band of Carbon Dioxide by the collision partners CH_3F, CO_2, N_2, Ar and Kr over the Temperature Ranges 300 to 150K," *Chemical Physics Letters*, Vol. 115, No. 1, 1985, pp. 60–65.

[30] Lopez-Valverde, M. A. and Lopez-Puertas, M., "A Non-local Thermodynamic Equilibrium Radiative Transfer Model for Infrared Emission in the Atmosphere of Mars," *Journal of Geophysical Research*, Vol. 99, No. 6, 1994, pp. 13,117–13,132.

[31] Limbaugh, C. and Drakes, J., "CO_2 Vibrational Relaxation Effects in a Laser-Heated Hypersonic Flow," AIAA Paper 1997–2492, June 1997.

[32] Rapp, D. and Kassal, T., "The Theory of Vibrational Energy Transfer between Simple Molecules in Nonreactive Collisions," *Chemical Review*, Vol. 69, No. 1, 1969, pp. 61–102.

[33] Jeffers, W. Q. and Kelley, J. D., "Calculations of V-V Transfer Probabilities in CO-CO Collisions," *Journal of Chemical Physics*, Vol. 55, No. 9, 1971, pp. 4433–4437.

[34] Herzberg, G., *Infrared and Raman Spectra*, Vol. 1, Van Nostrand, New York, 1st ed., 1947.

[35] Herzberg, G., *Spectra of Diatomic Molecules*, Vol. 1, Princeton: Van Nostrand, New York, 1st ed., 1959.

[36] T. Ahn, I. A. and Lempert, W. R., "Stimulated Raman Scattering Measurements of V-V Transfer in Oxygen," *Chemical Physics*, Vol. 323, No. 2, 2006, pp. 532–544.

[37] C. Park, J. T. Howe, R. L. J. and Candler, G. V., "Review of Chemical-Kinetic Problems of Future NASA Missions, II: Mars Entries," *Journal of Thermophysics and Heat Transfer*, Vol. 8, No. 1, 1994, pp. 9–23.

[38] Mitcheltree, R. A. and Gnoffo, P. A., "Wake flow about a MESUR Mars entry vehicle," AIAA Paper 1994–1958, June 1994.

[39] Landau, L. and Teller, E., "Zür Theorie der Schalldispersion," *Physik Z. Sowjetunion*, Vol. 10, No. 1, 1936, pp. 34.

[40] Camac, M., "CO_2 Relaxation Processes in Shock Waves," *Fundamental Phenomena in Hypersonic Flows*, Cornell Univ. Press, New York, 1966, pp. 195–215.

[41] Kelley, J. D. and Thommarson, R. L., "Vibrational Deactivation and Atom Exchange in $O(^3P)$+$CO(X^1\Sigma)$ collisions," *Journal of Chemical Physics*, Vol. 66, 1977, pp. 1953.

[42] Braunstein, M. and Duff, J. W., "Theoretical study of the $N(^2D)$+$O2(X^3\Sigma_g^-) \rightarrow$ O+NO reaction," *Journal of Chemical Physics*, Vol. 112, 2000, pp. 2736.

[43] Krupenie, P. H., "The Spectrum of Molecular Oxygen," *Journal of Physical and Chemical Reference Data*, Vol. 1, 1972, pp. 423–524.

[44] G. Colonna, D. D. and Capitelli, M., "Numerical Prediction of Non-equilibrium Flows in Hypersonic Nozzles: State-to-State Kinetics Versus Macroscopic Models." AIAA Paper 2003–3549, June 2003.

[45] Doraiswamy, S., Kelley, J. D., and Candler, G. V., "Vibrational Modeling of CO_2 for High Enthalpy Nozzle Flows," *Journal of Thermophysics and Heat Transfer*, Vol. 24, No. 1, 2010.

[46] Park, C., "Thermochemical Relaxation in Shock Tunnels," *Journal of Thermophysics and Heat Transfer*, Vol. 20, No. 4, 2006, pp. 689–698.

[47] Josyula, E. and Bailey, W. F., "Vibration-Dissociation Coupling Using Master Equations in Nonequilibrium Hypersonic Blunt-Body Flow," *Journal of Thermophysics and Heat Transfer*, Vol. 15, No. 2, 2001, pp. 157–167.

[48] Kelley, J. D., *High Enthalpy Air Modeling (purchase order 5419, subcontract 004)*, Feb. 2009.

[49] Kiefer, J. H. and Lutz, R. W., *11^{th} Combustion Symposium*, Combustion Institute, California, 1966, p. 67.

[50] Breen, J. E., Quy, R. B., and Glass, G. P., "Vibrational Relaxation of O_2 in the Presence of Atomic Oxygen," *Journal of Chemical Physics*, Vol. 59, No. 1, 1973, pp. 556–557.

[51] Warnatz, J., *Combustion Chemistry: Rate Coefficients in the C/H/O system*, Springer-Verlang, 1984.

[52] Levine, R. D. and Bernstein, R. B., *Modern Theoretical Chemistry, VIII, Dynamics of Molecular Collisions*, New York, 1st ed., 1975.

[53] Marrone, P. V. and Treanor, C. E., "Effect of Dissociation on the Rate of Vibrational Relaxation," *Physics of Fluids*, Vol. 6, 1962, pp. 1022.

[54] Marrone, P. V. and Treanor, C. E., "Chemical Relaxation with Preferrential Dissociation from Excited Vibrational Levels," *Journal of Chemical Physics*, Vol. 6, 1963, pp. 1215–1221.

[55] Oehlschlaeger, M. A., *Shock Tube Studies of Thermal Decomposition Reactions using Ultraviolet Absorption Spectroscopy*, Ph.D. thesis, Stanford University, California, June 2005.

[56] Center, R. E., "Vibrational Relaxation of CO by O atoms," *Journal of Chemical Physics*, Vol. 58, No. 12, 1973, pp. 5230–5236.

[57] M. E. Lewittes, C. E. D. and McFarlane, R. A., "Vibrational Deactivation of CO(v=1) by Oxygen atoms," *Journal of Chemical Physics*, Vol. 69, No. 5, 1978, pp. 1952–1957.

[58] Starr, D. F. and Hancock, J. K., "Vibrational energy transfer in CO_2-CO mixtures from 163 to 406K," *Journal of Chemical Physics*, Vol. 63, No. 12, 1975, pp. 4730–4734.

[59] Taylor, R. L., "Tables of Rate and Photochemical Data for Modeling of the Stratosphere," *Chemical Kinetics Data Survey, VII*, NBSIR 74-430, revised ed., 1974.

Appendix A

Model Constants in CO_2 and O_2 systems

Table A.1: Vibrational Temperatures of Species

Species	θ_v (K)
$CO_2(\nu_1)$	1918.7
$CO_2(\nu_2)$(doubly degenerate)	959.6
$CO_2(\nu_3)$	3382.1
CO	3122.0
O_2	2239.0

Table A.2: Formation Enthalpy of Species (J/kg)

Species	θ_v (K)
CO_2(X)	-8.932×10^6
CO_2(A)	1.440×10^6
CO	-4.063×10^6
O_2	0.0
O	1.542×10^7
Ar	0.0

Table A.3: Viscosity Coefficients for the Blottner Model

Species	A_s	B_s	C_s
CO_2(X)	-4.1372×10^{-2}	1.3293×10^{0}	-1.5016×10^{1}
CO_2(A)	-4.1372×10^{-2}	1.3293×10^{0}	-1.5016×10^{1}
CO	0.0183×10^{0}	0.4360×10^{0}	-1.1691×10^{1}
O_2	4.4929×10^{-2}	-8.2615×10^{-2}	-9.2019×10^{0}
O	2.0314×10^{-2}	4.2944×10^{-1}	-1.1603×10^{1}
Ar	-0.2201×10^{-1}	0.1010×10^{1}	-0.1342×10^{2}

Table A.4: Rate constants for CO_2-CO-O_2-O system.

Reaction	M	C_M (cm^3/mol-s)	θ (K)	Source
Dissociation Reactions				
$CO_2 + M \rightleftharpoons CO + O + M$	CO_2	2.2×10^{15}	51300	[55]
	CO	9.4×10^{14}		
	O_2	9.4×10^{14}		
	O	9.4×10^{14}		
$O + O + M \rightleftharpoons O_2 + M$	CO_2	8.1×10^{13}	-890.6	[51]
	CO	4.1×10^{13}		
	O_2	2.2×10^{13}		
	O	2.2×10^{13}		
Exchange Reactions				
$CO_2 + O \rightleftharpoons CO + O_2$		2.5×10^{12}	24056	[51]

Appendix B

Rate Constants for vibrational processes in CO_2 system

Table B.1: Rate constants for intramolecular V-V processes.

Reaction	C (cm^3/s)[1]	ΔE (cm^{-1})	Source
$CO(v{=}1) + CO(v{=}1) \rightleftharpoons CO(v{=}0) + CO(v{=}2)$	4.0^{-13}	27	[33]
$CO(v{=}1) + CO(v{=}2) \rightleftharpoons CO(v{=}0) + CO(v{=}3)$	6.0^{-13}	54	
$CO(v{=}1) + CO(v{=}3) \rightleftharpoons CO(v{=}0) + CO(v{=}4)$	8.0^{-13}	80	
$CO(v{=}2) + CO(v{=}2) \rightleftharpoons CO(v{=}1) + CO(v{=}3)$	1.2^{-12}	27	
$CO(v{=}2) + CO(v{=}3) \rightleftharpoons CO(v{=}1) + CO(v{=}4)$	1.6^{-12}	54	
$CO(v{=}3) + CO(v{=}3) \rightleftharpoons CO(v{=}2) + CO(v{=}4)$	2.4^{-12}	27	
$CO_2(\nu_3 = 1) + CO_2(\nu_3 = 1) \rightleftharpoons CO_2(\nu_3 = 0) + CO_2(\nu_3 = 2)$	4.0^{-13}	25	[33]
$CO_2(\nu_3 = 1) + CO_2(\nu_3 = 2) \rightleftharpoons CO_2(\nu_3 = 0) + CO_2(\nu_3 = 3)$	6.0^{-13}	50	
$CO_2(\nu_3 = 2) + CO_2(\nu_3 = 2) \rightleftharpoons CO_2(\nu_3 = 1) + CO_2(\nu_3 = 3)$	1.2^{-12}	25	
$O_2(v{=}1) + O_2(v{=}1) \rightleftharpoons O_2(v{=}0) + O_2(v{=}2)$	4.0^{-13}	24	[36]
$O_2(v{=}1) + O_2(v{=}2) \rightleftharpoons O_2(v{=}0) + O_2(v{=}3)$	6.0^{-13}	48	
$O_2(v{=}1) + O_2(v{=}3) \rightleftharpoons O_2(v{=}0) + O_2(v{=}4)$	8.0^{-13}	72	
$O_2(v{=}1) + O_2(v{=}4) \rightleftharpoons O_2(v{=}0) + O_2(v{=}5)$	8.0^{-13}	97	
$O_2(v{=}2) + O_2(v{=}2) \rightleftharpoons O_2(v{=}1) + O_2(v{=}3)$	1.2^{-12}	24	
$O_2(v{=}2) + O_2(v{=}3) \rightleftharpoons O_2(v{=}1) + O_2(v{=}4)$	1.6^{-12}	48	
$O_2(v{=}2) + O_2(v{=}4) \rightleftharpoons O_2(v{=}1) + O_2(v{=}5)$	2.0^{-12}	72	
$O_2(v{=}3) + O_2(v{=}3) \rightleftharpoons O_2(v{=}2) + O_2(v{=}4)$	2.4^{-12}	24	
$O_2(v{=}3) + O_2(v{=}4) \rightleftharpoons O_2(v{=}2) + O_2(v{=}5)$	3.0^{-12}	48	
$O_2(v{=}4) + O_2(v{=}4) \rightleftharpoons O_2(v{=}3) + O_2(v{=}5)$	4.0^{-12}	24	

[1] $4.0^{-13} \equiv 4.0{\times}10^{-13}$

Table B.2: Rate constants for V-T,R processes.

Reaction	C (cm^3/s)	B	ΔE (cm^{-1})	Source
CO(v=1) + O $\rightleftharpoons$ CO(v=0) + O	2.50^{-6}	-168	2143	[56, 57]
CO(v=2) + O $\rightleftharpoons$ CO(v=1) + O	5.00^{-6}	-168	2116	
CO(v=3) + O $\rightleftharpoons$ CO(v=2) + O	7.50^{-6}	-168	2089	
CO(v=4) + O $\rightleftharpoons$ CO(v=3) + O	1.00^{-5}	-168	2063	
CO(v=1) + $\Sigma\mathbf{CO_2}$ $\rightleftharpoons$ CO(v=0) + $\Sigma\mathbf{CO_2}$	1.20^{-6}	-240	2143	[18]
CO(v=2) + $\Sigma\mathbf{CO_2}$ $\rightleftharpoons$ CO(v=1) + $\Sigma\mathbf{CO_2}$	2.40^{-6}	-240	2116	
CO(v=3) + $\Sigma\mathbf{CO_2}$ $\rightleftharpoons$ CO(v=2) + $\Sigma\mathbf{CO_2}$	3.60^{-6}	-240	2089	
CO(v=4) + $\Sigma\mathbf{CO_2}$ $\rightleftharpoons$ CO(v=3) + $\Sigma\mathbf{CO_2}$	4.80^{-6}	-240	2063	
CO(v=1) + $\Sigma\mathbf{CO}$ $\rightleftharpoons$ CO(v=0) + $\Sigma\mathbf{CO}$	1.20^{-6}	-240	2143	
CO(v=2) + $\Sigma\mathbf{CO}$ $\rightleftharpoons$ CO(v=1) + $\Sigma\mathbf{CO}$	2.40^{-6}	-240	2116	
CO(v=3) + $\Sigma\mathbf{CO}$ $\rightleftharpoons$ CO(v=2) + $\Sigma\mathbf{CO}$	3.60^{-6}	-240	2089	
CO(v=4) + $\Sigma\mathbf{CO}$ $\rightleftharpoons$ CO(v=3) + $\Sigma\mathbf{CO}$	4.80^{-6}	-240	2063	
CO(v=1) + $\Sigma\mathbf{O_2}$ $\rightleftharpoons$ CO(v=0) + $\Sigma\mathbf{O_2}$	1.20^{-6}	-240	2143	
CO(v=2) + $\Sigma\mathbf{O_2}$ $\rightleftharpoons$ CO(v=1) + $\Sigma\mathbf{O_2}$	2.40^{-6}	-240	2116	
CO(v=3) + $\Sigma\mathbf{O_2}$ $\rightleftharpoons$ CO(v=2) + $\Sigma\mathbf{O_2}$	3.60^{-6}	-240	2089	
CO(v=4) + $\Sigma\mathbf{O_2}$ $\rightleftharpoons$ CO(v=3) + $\Sigma\mathbf{O_2}$	4.80^{-6}	-240	2063	
O_2(v=1)+ O $\rightleftharpoons$ O_2(v=0) + O	3.40^{-9}	-67.5	1556	[49, 50]
O_2(v=2)+ O $\rightleftharpoons$ O_2(v=1) + O	6.80^{-9}	-67.5	1532	
O_2(v=3)+ O $\rightleftharpoons$ O_2(v=2) + O	1.02^{-8}	-67.5	1508	
O_2(v=4)+ O $\rightleftharpoons$ O_2(v=3) + O	1.36^{-8}	-67.5	1484	
O_2(v=1) + $\Sigma\mathbf{CO_2}$ $\rightleftharpoons$ O_2(v=0) + $\Sigma\mathbf{CO_2}$	3.60^{-7}	-190	1556	[18]
O_2(v=2) + $\Sigma\mathbf{CO_2}$ $\rightleftharpoons$ O_2(v=1) + $\Sigma\mathbf{CO_2}$	7.20^{-7}	-190	1532	
O_2(v=3) + $\Sigma\mathbf{CO_2}$ $\rightleftharpoons$ O_2(v=2) + $\Sigma\mathbf{CO_2}$	1.08^{-6}	-190	1508	
O_2(v=4) + $\Sigma\mathbf{CO_2}$ $\rightleftharpoons$ O_2(v=3) + $\Sigma\mathbf{CO_2}$	1.44^{-6}	-190	1484	
O_2(v=1) + $\Sigma\mathbf{CO}$ $\rightleftharpoons$ O_2(v=0) + $\Sigma\mathbf{CO}$	3.60^{-7}	-190	1556	
O_2(v=2) + $\Sigma\mathbf{CO}$ $\rightleftharpoons$ O_2(v=1) + $\Sigma\mathbf{CO}$	7.20^{-7}	-190	1532	
O_2(v=3) + $\Sigma\mathbf{CO}$ $\rightleftharpoons$ O_2(v=2) + $\Sigma\mathbf{CO}$	1.08^{-6}	-190	1508	
O_2(v=4) + $\Sigma\mathbf{CO}$ $\rightleftharpoons$ O_2(v=3) + $\Sigma\mathbf{CO}$	1.44^{-6}	-190	1484	
O_2(v=1) + $\Sigma\mathbf{O_2}$ $\rightleftharpoons$ O_2(v=0) + $\Sigma\mathbf{O_2}$	3.60^{-7}	-190	1556	
O_2(v=2) + $\Sigma\mathbf{O_2}$ $\rightleftharpoons$ O_2(v=1) + $\Sigma\mathbf{O_2}$	7.20^{-7}	-190	1532	
O_2(v=3) + $\Sigma\mathbf{O_2}$ $\rightleftharpoons$ O_2(v=2) + $\Sigma\mathbf{O_2}$	1.08^{-6}	-190	1508	
O_2(v=4) + $\Sigma\mathbf{O_2}$ $\rightleftharpoons$ O_2(v=3) + $\Sigma\mathbf{O_2}$	1.44^{-6}	-190	1484	
$CO_2(\nu_3 = 1)$ + $\Sigma\mathbf{CO_2}$ $\rightleftharpoons$ $CO_2(\nu_3 = 0)$ + $\Sigma\mathbf{CO_2}$	3.10^{-10}	-80.6	2349	[30]
$CO_2(\nu_3 = 2)$ + $\Sigma\mathbf{CO_2}$ $\rightleftharpoons$ $CO_2(\nu_3 = 1)$ + $\Sigma\mathbf{CO_2}$	6.20^{-10}	-80.6	2324	
$CO_2(\nu_3 = 3)$ + $\Sigma\mathbf{CO_2}$ $\rightleftharpoons$ $CO_2(\nu_3 = 2)$ + $\Sigma\mathbf{CO_2}$	9.30^{-10}	-80.6	2299	
$CO_2(\nu_3 = 1)$ + $\Sigma\mathbf{CO}$ $\rightleftharpoons$ $CO_2(\nu_3 = 0)$ + $\Sigma\mathbf{CO}$	2.10^{-12}	-46.1	2349	
$CO_2(\nu_3 = 2)$ + $\Sigma\mathbf{CO}$ $\rightleftharpoons$ $CO_2(\nu_3 = 1)$ + $\Sigma\mathbf{CO}$	4.20^{-12}	-46.1	2324	
$CO_2(\nu_3 = 3)$ + $\Sigma\mathbf{CO}$ $\rightleftharpoons$ $CO_2(\nu_3 = 2)$ + $\Sigma\mathbf{CO}$	6.30^{-12}	-46.1	2299	
$CO_2(\nu_3 = 1)$ + $\Sigma\mathbf{O_2}$ $\rightleftharpoons$ $CO_2(\nu_3 = 0)$ + $\Sigma\mathbf{O_2}$	1.25^{-12}	-4.6	2349	
$CO_2(\nu_3 = 2)$ + $\Sigma\mathbf{O_2}$ $\rightleftharpoons$ $CO_2(\nu_3 = 1)$ + $\Sigma\mathbf{O_2}$	2.50^{-12}	-4.6	2324	
$CO_2(\nu_3 = 3)$ + $\Sigma\mathbf{O_2}$ $\rightleftharpoons$ $CO_2(\nu_3 = 2)$ + $\Sigma\mathbf{O_2}$	3.75^{-12}	-4.6	2299	
$CO_2(\nu_3 = 1)$ + O $\rightleftharpoons$ $CO_2(\nu_3 = 0)$ + O	6.25^{-13}	0	2349	
$CO_2(\nu_3 = 2)$ + O $\rightleftharpoons$ $CO_2(\nu_3 = 1)$ + O	1.25^{-12}	0	2324	
$CO_2(\nu_3 = 3)$ + O $\rightleftharpoons$ $CO_2(\nu_3 = 2)$ + O	1.87^{-12}	0	2299	

Table B.3: Rate constants for intermolecular V-V processes.

Reaction	C (cm^3/s)	B	ΔE (cm^{-1})	Source
$CO_2(\nu_3 = 1) + CO(v{=}0) \rightleftharpoons CO_2(\nu_3 = 0) + CO(v{=}1)$	9.40^{-12}	-30.12	206	[58, 59]
$CO_2(\nu_3 = 2) + CO(v{=}0) \rightleftharpoons CO_2(\nu_3 = 1) + CO(v{=}1)$	1.90^{-11}	-27.60	181	
$CO_2(\nu_3 = 3) + CO(v{=}0) \rightleftharpoons CO_2(\nu_3 = 2) + CO(v{=}1)$	2.80^{-11}	-25.00	156	
$CO_2(\nu_3 = 1) + CO(v{=}1) \rightleftharpoons CO_2(\nu_3 = 0) + CO(v{=}2)$	1.90^{-11}	-32.70	233	
$CO_2(\nu_3 = 2) + CO(v{=}1) \rightleftharpoons CO_2(\nu_3 = 1) + CO(v{=}2)$	3.80^{-11}	-30.31	208	
$CO_2(\nu_3 = 3) + CO(v{=}1) \rightleftharpoons CO_2(\nu_3 = 2) + CO(v{=}2)$	5.60^{-11}	-27.90	183	
$CO_2(\nu_3 = 1) + CO(v{=}2) \rightleftharpoons CO_2(\nu_3 = 0) + CO(v{=}3)$	2.80^{-11}	-35.2	260	
$CO_2(\nu_3 = 2) + CO(v{=}2) \rightleftharpoons CO_2(\nu_3 = 1) + CO(v{=}3)$	5.60^{-11}	-32.9	235	
$CO_2(\nu_3 = 3) + CO(v{=}2) \rightleftharpoons CO_2(\nu_3 = 2) + CO(v{=}3)$	8.50^{-11}	-30.5	210	
$CO_2(\nu_3 = 1) + CO(v{=}3) \rightleftharpoons CO_2(\nu_3 = 0) + CO(v{=}4)$	3.80^{-11}	-37.6	287	
$CO_2(\nu_3 = 2) + CO(v{=}3) \rightleftharpoons CO_2(\nu_3 = 1) + CO(v{=}4)$	7.50^{-11}	-35.4	262	
$CO_2(\nu_3 = 3) + CO(v{=}3) \rightleftharpoons CO_2(\nu_3 = 2) + CO(v{=}4)$	1.10^{-10}	-33.1	237	
$CO(v{=}1) + O_2(v{=}0) \rightleftharpoons CO(v{=}0) + O_2(v{=}1)$	3.50^{-10}	-124.0	587	[58, 59]
$CO(v{=}2) + O_2(v{=}0) \rightleftharpoons CO(v{=}1) + O_2(v{=}1)$	7.00^{-10}	-120.0	560	
$CO(v{=}3) + O_2(v{=}0) \rightleftharpoons CO(v{=}2) + O_2(v{=}1)$	1.10^{-9}	-116.0	533	
$CO(v{=}4) + O_2(v{=}0) \rightleftharpoons CO(v{=}3) + O_2(v{=}1)$	1.40^{-9}	-112.0	506	
$CO(v{=}1) + O_2(v{=}1) \rightleftharpoons CO(v{=}0) + O_2(v{=}2)$	7.00^{-10}	-127.0	611	
$CO(v{=}2) + O_2(v{=}1) \rightleftharpoons CO(v{=}1) + O_2(v{=}2)$	1.40^{-9}	-124.0	584	
$CO(v{=}3) + O_2(v{=}1) \rightleftharpoons CO(v{=}2) + O_2(v{=}2)$	2.10^{-9}	-120.0	557	
$CO(v{=}4) + O_2(v{=}1) \rightleftharpoons CO(v{=}3) + O_2(v{=}2)$	2.10^{-9}	-116.0	530	
$CO(v{=}1) + O_2(v{=}2) \rightleftharpoons CO(v{=}0) + O_2(v{=}3)$	1.05^{-9}	-131.0	635	
$CO(v{=}2) + O_2(v{=}2) \rightleftharpoons CO(v{=}1) + O_2(v{=}3)$	2.10^{-9}	-127.0	608	
$CO(v{=}3) + O_2(v{=}2) \rightleftharpoons CO(v{=}2) + O_2(v{=}3)$	3.20^{-9}	-123.0	581	
$CO(v{=}4) + O_2(v{=}2) \rightleftharpoons CO(v{=}3) + O_2(v{=}3)$	4.20^{-9}	-119.0	554	
$CO(v{=}1) + O_2(v{=}3) \rightleftharpoons CO(v{=}0) + O_2(v{=}4)$	1.40^{-9}	-134.0	659	
$CO(v{=}2) + O_2(v{=}3) \rightleftharpoons CO(v{=}1) + O_2(v{=}4)$	2.80^{-9}	-130.0	633	
$CO(v{=}3) + O_2(v{=}3) \rightleftharpoons CO(v{=}2) + O_2(v{=}4)$	4.20^{-9}	-127.0	605	
$CO(v{=}4) + O_2(v{=}3) \rightleftharpoons CO(v{=}3) + O_2(v{=}4)$	5.60^{-9}	-123.0	579	
$CO(v{=}1) + O_2(v{=}4) \rightleftharpoons CO(v{=}0) + O_2(v{=}5)$	1.75^{-9}	-137.0	683	
$CO(v{=}2) + O_2(v{=}4) \rightleftharpoons CO(v{=}1) + O_2(v{=}5)$	3.50^{-9}	-134.0	657	
$CO(v{=}3) + O_2(v{=}4) \rightleftharpoons CO(v{=}2) + O_2(v{=}5)$	5.30^{-9}	-130.0	630	
$CO(v{=}4) + O_2(v{=}4) \rightleftharpoons CO(v{=}3) + O_2(v{=}5)$	7.00^{-9}	-126.0	603	